rijksuniversiteit
groningen

The impact of dark satellites on dwarf galaxies in a ΛCDM universe

Proefschrift

ter verkrijging van de graad van doctor aan de
Rijksuniversiteit Groningen
op gezag van de
rector magnificus prof. dr. E. Sterken
en volgens besluit van het College voor Promoties.

De openbare verdediging zal plaatsvinden op

vrijdag 24 juni 2016 om 14:30 uur

door

Tjitske Karen Starkenburg

geboren op 18 januari 1987
te Hengelo

Promotor
Prof. dr. A. Helmi

Beoordelingscommissie
Prof. dr. E. Tolstoy
Prof. dr. J. Schaye
Prof. dr. J. F. Navarro

ISBN: 978-90-367-8958-5 (printed version)
ISBN: 978-90-367-8957-8 (electronic version)

Cover: The images depict different components of a dwarf galaxy that is undergoing a minor merger with a dark satellite. The simulation of this sytem is presented in Chapter 3 and discussed in more detail in Chapter 4 of this Thesis. All images are close to face-on, and made using VaeX (Visualization and eXploration; www.astro.rug.nl/∼breddels/vaex). The components shown clockwise from the title are: the stellar disk, the dark matter halos, the gas disk, the position-velocity diagram of the gas disk, and the location of current starformation within the gas disk.
Printed by: Gildeprint - The Netherlands

Contents

1

Introduction

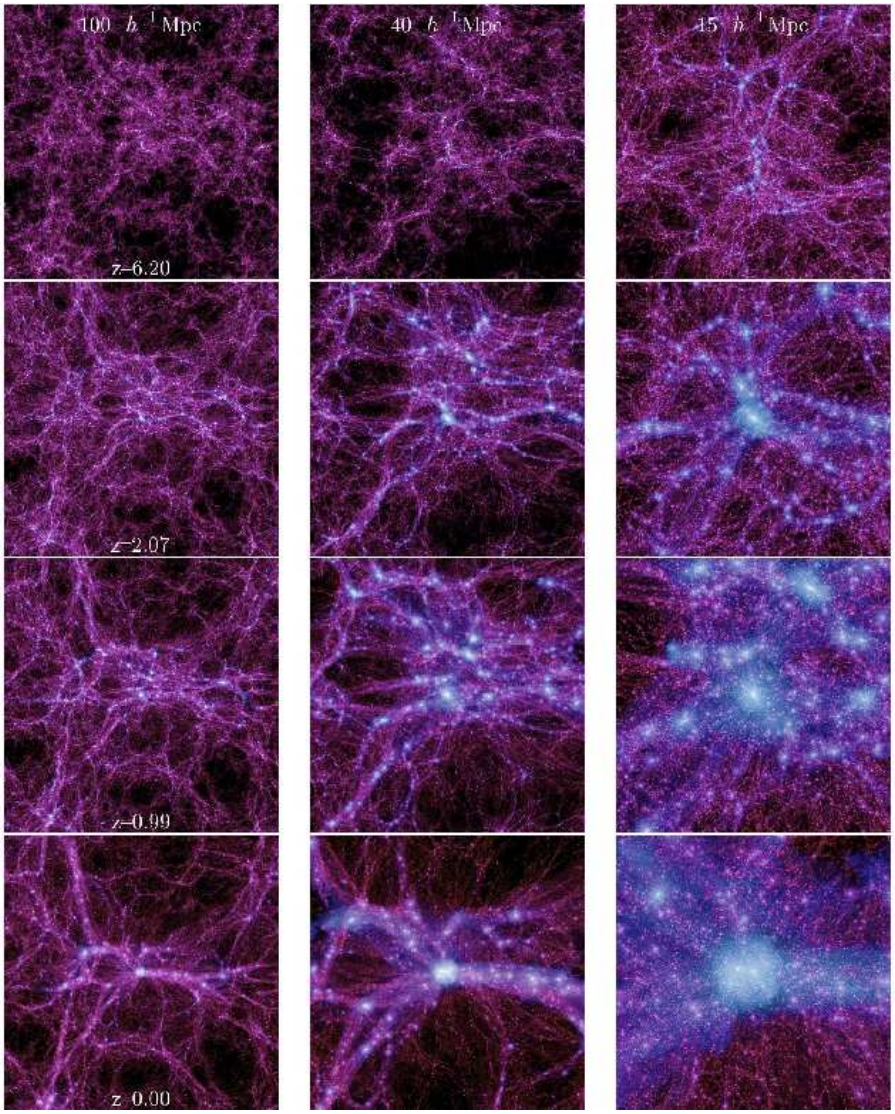

Figure 1.1 – Time evolution of the (from left to right) full simulation box of 100 Mpc/h, and two regions further zoomed-in around the most massive halo ($M_{\rm FOFhalo} = 8.2 \times 10^{14}\ M_{\odot}$) at the present time ($z = 0$), of 40 and 15 Mpc/h (all in comoving units). From top to bottom: $z = 6$, 2, 1, and 0. Figure from Boylan-Kolchin et al. (2009).

1.1 Hierarchical structure formation

The large scale structure present in the Universe is thought to have formed in a hierarchical fashion (e.g. Press & Schechter 1974; Rees & Ostriker 1977; White & Rees 1978). Starting from a hot and dense state, the early Universe contained small overdensities, whose traces are seen in the Cosmic Microwave Background. When overdensities contain sufficient mass to counter the expanding Hubble flow of the Universe, they collapse and form self-bound structures, the (dark matter) halos. These halos are often found in sheets, filaments, nodes, and voids, as can be seen from Fig. 1.1. So although modern cosmology is built upon the hypothesis of an isotropic and uniform universe on exceedingly large scales (the cosmological principle), on smaller scales the distribution of matter is highly non-linear.

Of the matter content in our Universe a dominant fraction is thought to be in the form of weakly-interacting particles. Indications of the existence of this "dark matter" are found on a variety of scales, from e.g. rotation curves of individual galaxies (Rubin & Ford 1970; Rubin et al. 1980; Bosma 1978), to clusters of galaxies (the first discovery by Zwicky 1933, 1937), the Universe as a whole (Allen et al. 2003; Komatsu et al. 2011; Planck Collaboration et al. 2014). The search for direct evidence of this dark matter, and the determination of its nature, is strongly being pursued at the moment by astrophysicists as well as particle physicists (e.g. Ackermann et al. 2014; Ajello et al. 2015; Daylan et al. 2016), and the hope is that this mystery will be solved in the coming decade. The ΛCDM-cosmology is the currently favored cosmological model, where dark energy dominates the energy density of the Universe with $\sim 69\%$ (Planck Collaboration et al. 2014), "cold" dark matter accounts for $\sim 26\%$, and where the last $\sim 5\%$ is in baryons, of which we have observed only a fraction thus far.

Galaxies in the Universe

Galaxies are believed to form and be embedded in dark matter halos (e.g. Freeman & Bland-Hawthorn 2002). While in the early Universe, during the first phases of that formation process, galaxies have very irregular shape and structure, toward the present time different morphologies can be identified (e.g. Conselice 2014). The best known classification scheme identifies two main groups or classes: ellipticals and spirals (the Hubble tuning fork, Hubble 1936; Sandage 1961). Galaxies that do not fit into these defined classes fall into a separate group of "irregular galaxies".

Elliptical galaxies, as their name suggests, have an elliptical shape and a generally rather smooth brightness profile, following a Sérsic (e.g. Sérsic 1963; Blanton & Moustakas 2009) light profile falling off with $R^{1/n}$ where often for giant elliptical galaxies $n = 4$ (the de Vaucouleurs profile, de Vaucouleurs 1948), while for dwarf elliptical galaxies $n = 1$. Upon closer examination

however, deviations from the smooth profile are apparent in the form of shells and streams in the outer regions and disk-like structures in the inner parts (van Dokkum 2005; Duc et al. 2011; Krajnović et al. 2013). At galaxy masses similar to the Milky Way ellipticals form a relatively small fraction of the galaxy population but toward larger galaxy masses they are increasingly dominant (Conselice 2006; Guo et al. 2011). Central galaxies in clusters are almost always large ellipticals, and the fraction of ellipticals decreases with decreasing galaxy density in the cluster (or group) (the morphology-density relation, Dressler 1980; Postman & Geller 1984; Whitmore et al. 1993; Blanton & Moustakas 2009; Conselice 2014).

Spiral galaxies, of which the Milky Way is one, are the most common galaxy within the intermediate mass range (Conselice 2006; Blanton & Moustakas 2009; Conselice 2014). The disk with its spiral structure is the most striking morphological feature but other components, like bulges and bars are also present, with varying degrees of prominence. The stellar and gas disks are generally described by exponential profiles, morphologically as well as kinematically, with scale radii of a few kpc for Milky Way-like galaxies, although the gas disk can be more extended than the stellar disk. The disk height is generally described by an isothermal profile with disk scale height about $\lesssim 10\%$ of the disk scale length for thin disks, and disk scale heights of up to $\lesssim 50\%$ (especially for lower mass galaxies, Roychowdhury et al. 2010) of the disk scale length for thick disks. Besides the major components smaller substructure, asymmetries, or deviations from exponential disks, can also be present, like streams, rings, shells, arms, plumes, warps, and lopsidedness. These substructures can be due to internal effects such as disk instabilities or bar formation, or external influences like satellite infall or other tidal disturbances. Irregular galaxies generally lack the regular disk appearance, or are dominated by substructures such as those described above.

Toward lower masses or luminosities disky systems can be seen to become more and more irregular (e.g. Gallagher & Hunter 1984). Such systems are smaller, with disk scale lengths $R_d \lesssim 1$ kpc, and thicker, with velocity dispersions more comparable to the rotational velocities. There are a number of different definitions of what exactly denotes a dwarf galaxy, but one often used is: systems with $M_V \geq -17$ and that are more extended than a globular cluster (Tamman 1994; Tolstoy et al. 2009). There is a large number of morphological types within the dwarf galaxy regime. These types have appeared historically and are based on a variety of properties, and depict significant overlap. Some of the most well-known classes are: dwarf spheroidals (dSph), dwarf irregulars (dIrr), dwarf ellipticals (dEll), ultra-faint dwarf galaxies (UFD), blue compact dwarfs (BCD), extremely metal-poor galaxies (XMP), HII galaxies, ultra-compact dwarfs (UCD).

The existence of a lower bound on the mass of galaxies have been questioned already for a few decades, (e.g. Arp 1965). For the last two decades this

question has mostly come up in the context of the so-called "missing satellites" problem as described by Klypin et al. (1999) and Moore et al. (1999), but also in computational efforts that better and better resolve low-mass systems. It appears plausible that observations miss a large set of satellites (and low-mass galaxies in the field) because these systems have formed (almost) no stars for various physical reasons, and so are hard or impossible to observe directly (Klypin et al. 1999). However other alternatives exist, such as a cut-off in the smallest mass halo that can form (driven by the intrinsic nature of dark matter itself). Dwarf galaxies and star-less dark galaxies will be further discussed in Sect. 1.3.

1.1.1 Modeling structure formation

For a system where the collisional relaxation timescale is long compared to its characteristic timescale (i.e. the orbital period of stars in a galaxy disk, or of dark matter particles in a dark matter halo), we can consider the constituent particles that almost only interact through gravity as essentially fully collissionless. Thanks to this and to the dominance of (cold) dark matter, the formation of structure in the Universe can be extensively and successfully studied using large cosmological N-body simulations. This allows for extremely large simulation volumes that model structure on large scales (of 10–1000 Mpc). On the other hand simulations of smaller volumes ($<$ 10 Mpc) with higher resolution can be used to study in detail the formation and evolution, structure and substructure, of individual dark matter halos, and groups of halos. Specific zoom-in (e.g. Aquarius, Springel et al. 2008; NIHAO, Wang et al. 2015; APOSTLE, Sawala et al. 2016a) or constrained (e.g. CLUES, Gottlöber et al. 2010), simulations are often oriented toward simulating the distribution of dark matter in Milky Way-like or Local Group-like environments.

Such N-body simulations determine the gravitational acceleration of one particle from all other particles by solving Poisson's equation. For a low number of particles, for example in star clusters, this is literally what is done, but for larger numbers of particles direct summation of the forces (which has $\mathcal{O}(\mathrm{N}^2)$ time complexity) quickly becomes too computationally expensive. In that case instead of the exact forces of individual particles at large distances, these are approximated by the cumulative force from the center of mass (the hierarchical tree code, Barnes & Hut 1986; Hernquist & Katz 1989). Another approach is to calculate the potential due to the forces of all particles on a grid and moving the particles along gradients of this potential, as in particle-mesh codes (Hockney & Eastwood 1988). In most codes nowadays both these ($\mathcal{O}(\mathrm{NlogN})$) approximations are combined in tree-PM codes (Xu 1995) where the short-range forces are calculated using a tree, and long-range forces are approximated using a grid.

The power of dark matter-only simulations lies in tracing the evolution of structure in the Universe, from the very early times until the present day. They allow for the study of the abundance, clustering, internal structure, shape, and angular momentum of the individual dark matter halos that form, as well as of the large scale cosmic web in which they are embedded. The density distributions obtained in ΛCDM cosmological simulations compare very well to those found in large surveys on large scales (e.g. Primack 2005). Another advantage of such N-body simulations is that one can experiment with different dark matter models and monitor the differences in the structure distribution. Modeled alternatives include various "warm" dark matter particles, with larger energies (e.g. CLUES, Zavala et al. 2009; COCO, Bose et al. 2016), and a number of flavors of "self-interacting dark matter" (e.g. Vogelsberger et al. 2012; Rocha et al. 2013), among others.

In most cases to trace the history of a specific halo a series of so-called post processing techniques are used. In the first step, all the halos at each output snapshot of the simulation have to be "found", or identified. This can be done in different ways, e.g. by defining groups of particles that occupy similar regions in physical and phase space, for example with a Friends-Of-Friends algorithm (FOF, Davis et al. 1985), which is usually combined with a second algorithm to identify objects bound by their self-gravity (e.g. SUBFIND, Springel et al. 2001a). Alternatively, halos can be found as overdensities within the density distribution in physical and/or phase space (e.g. ROCKSTAR, Behroozi et al. 2013b). In the next step halos from different snapshots are connected via a progenitors-descendant-scheme, where each halo has one unique descendant (the halo in the next snapshot with the most particles of the progenitor halo weighted by e.g. a rank based on binding energy), but can have more than one progenitor. In this way merger trees are build up. These trees contain information about the properties of halos at each snapshot as well as its descendant and its progenitors, and so can be used to trace the evolution, including mergers, of halos. Therefore, the halo- and subhalo-catalogs and the merger trees can be used efficiently to study many halo properties from a simulation, without having to inspect the large datasets usually associated with the snapshots with all the particle information. For example, such merger trees are often used as a backbone for semi-analytic modeling of galaxy formation.

As an example Fig. 1.1 shows the formation and evolution of the most massive halo formed in a large cosmological simulation. This most massive halo is comparable to the Coma cluster with a mass of $M_{\rm FOFhalo} = 8.2 \times 10^{14}\ M_{\odot}$, and consists of 119.5 million particles and ≈ 36000 resolved subhalos over nearly 7 orders of magnitude in mass (Boylan-Kolchin et al. 2009).

1.1.2 Modeling galaxy formation and evolution

Including hydrodynamics in the cosmological N-body simulations enables the study of the formation and evolution of galaxies. The dynamics of the gas is mainly modeled with two different methods: mesh-based hydrodynamics (Eulerian; see for a review Teyssier 2015), or smoothed particle hydrodynamics (Lagrangian; see for a review Monaghan 1992; Springel 2010b), but a combined method, moving-mesh hydrodynamics (see for example AREPO, Springel 2010a), is now also used.

In the simulations described in this Thesis we use a smoothed particle hydrodynamics (SPH) approach (e.g. Gingold & Monaghan 1977; Lucy 1977; Monaghan 1992; Springel 2010b). SPH uses particles to trace a fluid and applies kernel smoothing and interpolation to determine the (continuous) fluid quantities. The GADGET simulation code (Springel et al. 2001b; Springel 2005), used in this Thesis, applies a specific implementation in which the thermodynamic state of each fluid particle is defined based on the entropy $A \equiv P/\rho^{\gamma} = A(s)$. GADGET uses an adaptive smoothing length based on a given number of neighbors.

Next to gravity and hydrodynamics the physics in simulations is largely governed by the so-called subgrid physics. This essentially means that there is a "resolution" limit present in the simulations based on how detailed the physics in the code is. Processes below this resolution limit, which should be consistent with the mass and length-scale resolution limits in the simulations, are described through prescriptions that mimic the outcome of smaller-scale processes on the resolution scale or empirical relations at the resolution scale.

Main subgrid processes in hydrodynamical codes are related to gas-physics, and are associated to processes such as gas heating and cooling, star formation and feedback, black hole formation and feedback from active galactic nuclei (AGN), stellar populations, and chemical evolution. For example the process of gas cooling is modeled using pre-calculated cooling-functions for a range in gas temperatures, densities, and metallicities. Most of the cooling at $T_{\rm gas} \gtrsim 10^4$ K is done through free-free emission ($T_{\rm gas} > 10^7$ K) and recombination (10^4 K $< T_{\rm gas} < 10^7$ K) in ionized gas (primordial –H and He– gas as well as heavier elements –metal-line cooling). Below this temperature collisional excitation/de-excitation of more heavier elements (metal-line cooling) and molecular cooling can cool the gas further (e.g. Somerville & Davé 2015). Heating on the other hand is mostly due to reionization or feedback effects like photoionization, stellar winds, shocks, and radiative or thermal feedback from stars and AGN.

For the onset of star formation, many codes apply a density threshold, with in addition sometimes other, less stringent criteria, like a convergent gas flow, and an upper limit for the gas temperature. The density threshold for star formation often depends on the level of sophistication of the input physics and the mass and spatial resolution (see e.g. House et al. 2011). In general all

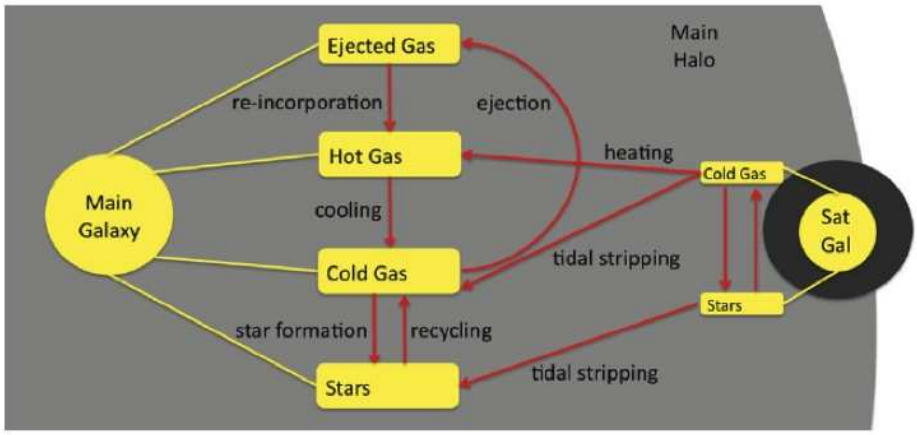

Figure 1.2 – A schematic overview of the semi-analytical modeling scheme from Starkenburg et al. (2013). It shows all different, analytically modeled, "phases" or components for baryons (yellow boxes) and all modeled physical prescriptions that affects these (red arrows), for a central galaxy within a dark matter halo and a satellite that has just been accreted.

star formation recipes are tuned or shown to reproduce the Kennicutt-Schmidt empirical relation in simulations of isolated disks (e.g. Scannapieco et al. 2012; Somerville & Davé 2015). The amount of star formation then depends on the local (surface or volume) density, and includes a certain stochasticity in the likelihood for star formation to take place. The amount of stars formed is usually assumed to follow a given initial mass function (IMF) and a fixed fraction is assumed to evolve into supernovae (SNe). These SNe (usually TypeII and TypeIa are taken into account), as well as, possibly, stellar winds and radiative feedback, affect the surrounding gas. The SNe feedback is generally dispersed over the neighboring gas particles/cells though thermal feedback, kinetic feedback, or entropy feedback (e.g. Scannapieco et al. 2012; Somerville & Davé 2015).

Another popular way to follow the formation and evolution of galaxies is through semi-analytic modeling (SAM) (e.g. Somerville & Davé 2015). Since galaxies are assumed to be embedded in dark matter halos, many of their properties are computed using information about dark matter halos

(for example halo merger trees). Dark matter-only simulations or analytic descriptions (see e.g. Press & Schechter 1974) form the skeleton by providing e.g. the number of objects of a given mass at a given time and their evolution in time (through e.g. merger trees). In the semi-analytic model a galaxy consists of a number of different constituents (like stars, hot gas, and cold gas), which hold a certain amount of mass. The mass flow and transformations from one constituent to another is followed with physically or empirically motivated prescriptions. An example of this is given in Fig. 1.2. The prescriptions used in semi-analytic modeling are in essence very similar to the subgrid physics of hydrodynamic simulations, with the exception that for SAMs also the characteristic sizes, densities, concentrations, masses, and radii are determined through prescriptions.

For example in many semi-analytic models the feedback, or ejected gas mass, due to star formation is in total described by $\dot{m}_{\rm ejected} = \epsilon_w \, (V_0/V_c)^{\alpha_w} \, \dot{m}_\star$, where $\dot{m}_\star$ is the rate of star formation in the galaxy, V_c is its circular velocity, V_0 is an arbitrary normalization parameter, and ϵ_w and α_w are tunable parameters, where for $\alpha_w = 1, 2$ the ejected mass approximates scalings for feedback through galactic winds from hydrodynamic simulations (Somerville & Davé 2015).

Calibration of the (combination of) unavoidable free parameters in the subgrid and semi-analytical prescriptions is often done using a selection of correlations of galaxy properties and scaling relations, found empirically, that have a small amount of scatter and are well-constrained. Examples of these are, the luminosity function, stellar mass function, the (Baryonic) Tully-Fisher relation, the main sequence of star-forming galaxies, the cold gas–stellar mass relation, the mass–size relation for spiral galaxies, the metallicity–stellar mass relation, and relations between the mass of the central supermassive black hole and galaxy properties (Somerville & Davé 2015, and references therein). Although no existing simulation fits all relations we observe simultaneously, simulations fit a larger subset of these relations increasingly well. Note however that fitting statistical relations does not necessarily imply that individual objects have realistic properties.

1.1.3 Controlled simulations

On non-cosmological scales the so-called "controlled" simulations are useful to explore in more detail the evolution of individual halos and galaxies. These simulations have a longer history than the fully cosmological simulations, starting from models of star clusters, with 16 (von Hoerner 1960) and 200 (Aarseth 1963) stellar particles, and galaxies, (Pfleiderer & Siedentopf 1961; Pfleiderer 1963; Tashpulatov 1969, 1970; Yabushita 1971; but see also the work by Holmberg 1941 who modeled a merger between two spiral galaxies by using light bulbs as tracer particles ($N = 37$ per galaxy) and the light intensity as gravitational force). With the growth in computational power, and faster

and more sophisticated algorithms, simulations where galaxies are modeled using millions of particles in the stellar, dark matter, and hot and cold gas components, are the norm now (see e.g. Athanassoula et al. 2016; Vera-Ciro et al. 2014). As similar codes are used as for the cosmological simulation the input physics is also similar.

An important aspect of controlled simulations is the modeling of the initial conditions. This is in contrast partly, to cosmological simulations where the initial conditions are known (to some extent) ab-initio. The character of the research might require for example an initially stable galaxy (for simulating galaxy interactions), or a deliberately, in a particular way, perturbed galaxy (for simulating the development of spiral and bar features (e.g. Athanassoula et al. 2013; D'Onghia 2015; Vera-Ciro et al. 2014, see also Chapter 2).

1.2 Galaxy interactions and mergers

Galaxies are often found to be significantly clustered on group, cluster, and larger scales, and sometimes also to be interacting. Many observed irregular features of galaxies, as for example apparent in Arp's catalog of (large) peculiar galaxies (Arp 1966), can be explained by being due to interactions. According to Toomre (1974) the idea of tidal features being due to interactions between galaxies can be dated back to Chamberlin (1901) (although he discusses the possible formation of spiral nebulae due to interacting gaseous spheres). However, the work by Toomre & Toomre (1972); Toomre (1977) is generally seen as the first numerical simulations that clearly have shown the impact of galaxy mergers, and thereby triggered the interest in this field.

For a long time it was believed that if two similar mass gas-rich disk galaxies merged this would always lead to an elliptical galaxy (e.g. Toomre 1977; Barnes & Hernquist 1992; Cox et al. 2008). In the last few years, however, some groups have shown that two gas-rich disk galaxies merging can also result in a disk galaxy, and that soon after the merger a new thin disk can form (e.g. Springel & Hernquist 2005; Athanassoula et al. 2016), depending on initial conditions. Mass ratio is thus not the only aspect that plays a role in interacting galaxies. For example, Di Matteo et al. (2007, 2008) have shown that while an increase in star formation rates, or even a starburst, often takes place during and/or after a merger (Mihos & Hernquist 1994a,b; Teyssier et al. 2010; Bournaud et al. 2011), and such an increase in star formation is in fact seen in observations (Ellison et al. 2011; Willett et al. 2015; Kaviraj 2014b,a; Willett et al. 2015), there is not a direct dependence on the merger mass ratio (but see Teyssier et al. 2010). They find that nuclear starbursts are triggered by gas inflow due to non-axisymmetries. As such, direct (prograde) encounters develop more asymmetries and therefore star formation enhancement. However, if more gas is dragged outside the galaxy

by tidal tails, i.e. if the tidal torques are stronger per time interval, the increase in central star formation rate is smaller (Di Matteo et al. 2007, 2008).

Studies into the dynamical effects of minor mergers have mostly focussed on Milky Way-like galaxies. In controlled simulations of systems similar in mass and structure to the Milky Way, minor mergers have been shown to be the source of substructure, like shells, plumes, ripples, X-features (e.g. Quinn & Goodman 1986; Barnes & Hernquist 1992), and more global disturbances as warps, boxy isophotes, disk thickening, and bulge creation or growth (e.g. Schweizer 1990; Toth & Ostriker 1992; Quinn et al. 1993; Walker et al. 1996; Huang & Carlberg 1997; Velazquez & White 1999; Font et al. 2001; Villalobos & Helmi 2008; Hopkins et al. 2008; Purcell et al. 2009; Moster et al. 2010; Qu et al. 2011). Minor mergers are generally harder to observationally identify due to their weaker impact compared to major mergers. On the other hand, this also means that the fractions of bulge-less galaxies and galaxies with really thin disks we observe can be used to constrain the fraction of minor mergers, the longevity of the effects due to minor mergers, or the dependence of the results of minor mergers on properties of the merging halos, galaxies, and the interaction (Toth & Ostriker 1992; Hopkins et al. 2008; Purcell et al. 2009; Moster et al. 2010).

1.3 On the scale of dwarf galaxies

There is a wide variety of dwarf galaxies seen in the Local Universe (e.g. Tolstoy et al. 2009; James et al. 2015). Dwarf galaxies outside of the Local Group came into view in large observing campaigns, that resulted in the Catalogue of galaxies and of clusters of galaxies (Zwicky et al. 1961, 1968), the Catalogue of selected compact galaxies and of post-eruptive galaxies (Zwicky & Zwicky 1971), and the Uppsala General Catalog (Nilson 1973, initiated by E. Holmberg). As small, and fragile, systems dwarf galaxies can be more severely affected by internal and external influences. On the other hand, this also complicates determining the specific processes that are responsible for the variety of observed morphological, structural, and kinematical properties in these systems.

Within a CDM universe the dark matter halo mass function is scale free, and the same subhalo mass function and hence similar merger ratios are expected on all scales (a dependence of the merger fraction on the present day halo mass is almost completely due to a dependence on halo formation redshift $z_{\rm form}$ (van den Bosch et al. 2005; van den Bosch & Jiang 2014). Fig. 1.3 shows a cluster-size halo (Gao et al. 2012) and a Milky Way-size halo (Springel et al. 2008) where the distribution of the dark matter substructure in both cases is essentially identical. The dark matter halo properties are found to be the same for dwarf galaxies as for larger mass halos in cosmological N-body simulations.

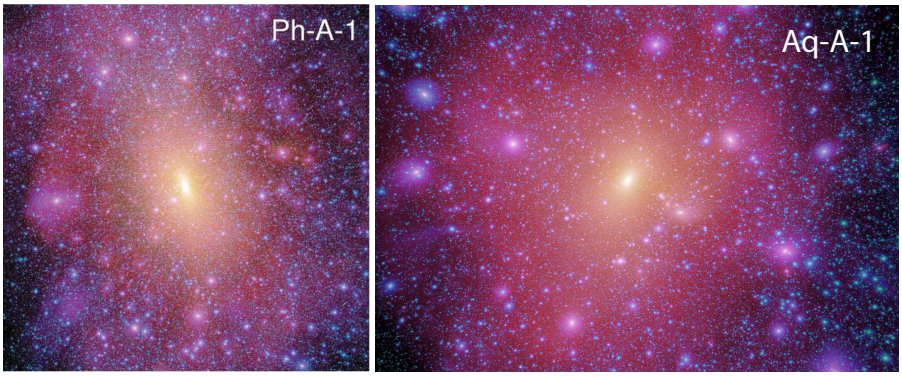

Figure 1.3 – Two dark matter distributions from two simulations: a cluster-size halo from the Phoenix project (Gao et al. 2012) and a Milky Way-size halo from the Aquarius project (Springel et al. 2008). The dark matter substructure is very similar (see also the discussion in Gao et al. 2012).

Lower mass galaxies are however expected to be strongly influenced by reionization, photoheating, and feedback (e.g. Gnedin 2000; Hoeft et al. 2006; Kaufmann et al. 2007; Okamoto et al. 2008; Gnedin et al. 2009; Li et al. 2010; Sawala et al. 2013). This is thought to have had significant effects on the star formation histories, and present day properties of dwarf galaxies (e.g. Weisz et al. 2014). Moreover, dwarf galaxies can be severely affected when in the neighborhood of larger mass galaxies, due to gas stripping and subsequent star formation quenching (e.g. Sofue 1994; Wetzel et al. 2013), and tidal effects (Mayer et al. 2001b,a, 2006; Sawala et al. 2016b) leading possibly to morphological transformations. Also dwarf–dwarf interactions are expected to be important (e.g. Ashley et al. 2013; Amorisco et al. 2014; Łokas et al. 2014). All these processes are thought to be responsible for the large variety of dwarf galaxies we see. For example Grebel et al. (2003) discuss three very different, but not necessarily independent, formation processes of dwarf spheroidal galaxies (but see also Ricotti & Gnedin 2005; Slater & Bell 2013; Benítez-Llambay et al. 2013), where one depends on more intrinsic properties, and others are due to environmental effects (as described for example in Mayer et al. 2006). Intriguingly however, a small number of dwarf spheroidal galaxies have been found in the field (Makarov et al. 2012; Karachentsev et al. 2015).

New observations seem to indicate that we may not have a fully complete view of the class of dwarf galaxies yet. For example, by using photometric properties of the XMP galaxy Leo P as a proxy, James et al. (2015) found a set of what they call blue diffuse dwarf (BDD) galaxies. Having a low surface brightness main body, and mostly only HII-regions that stand out, these objects would not readily be identified when not specifically searched for. Blue compact dwarf galaxies show similar characteristics, although with a bright center with young stars and a more diffuse older population (e.g.

Gil de Paz et al. 2003; Paudel et al. 2015). However, BCDs often show irregular morphologies and kinematics (Taylor et al. 1995; Ekta & Chengalur 2010; López-Sánchez 2010; Holwerda et al. 2013; Lelli et al. 2014a; Knapen & Cisternas 2015), in cases without a visible companion (Brosch et al. 2004; Ekta & Chengalur 2010; López-Sánchez 2010; Lelli et al. 2014b). But similar off-center bursts of star formation and kinematic differences between the stellar an gas component have also been observed in XMP galaxies (Filho et al. 2013, 2015). Figure 1.4 shows the Local Group dwarf galaxy IC10, which shows very irregular stellar and gas morphology and kinematics. The cause of these irregular features is still under debate (Nidever et al. 2013; Ashley et al. 2014).

In contrast to the halo mass function, the galaxy mass function is not scale free and sufficiently low-mass halos are expected to be completely devoid of baryons. This might partially be due to reionization and star-formation feedback, but when going to lower mass scales at some point the dark matter halos are too small/light to form any stars (e.g. Verde et al. 2002; Davies et al. 2006; Pustilnik 2008; but see also Taylor & Webster 2005; Warren et al. 2007). This is called a star-less or dark galaxy. Note that gas may be present, although stricter definitions, cold gas-less as well as star-less, are also used (and that is what we assume in the Chapters in this Thesis). Dwarf galaxies that have formed stars in the past but stopped doing so, for example due to reionization, generally called fossils, are not completely devoid of stars as dark galaxies are supposed to be. Nevertheless, as their stellar mass can be too low to be observable, in effect they can be similar to completely dark galaxies.

In general, isolated low-mass halos seem to be gas-rich, with $M_{\rm HI} > M_{\star}$, although they might only be able to form a small amount of stars (e.g. Schombert et al. 2001; Zhang et al. 2012; Yaryura et al. 2016). There have been observational efforts to find halos without stars in blind HI-surveys, combined with high resolution optical follow-up (e.g. Adams et al. 2015; Cannon et al. 2015; Janowiecki et al. 2015), but no unambiguous dark galaxies have been found to date. These observations are complicated due to the difficulty in distinguishing between individual systems and HI clouds belonging to other systems, like for example the High Velocity Clouds around the Milky Way (see also the discussion over the extended gas cloud VIRGOHI21, Minchin et al. 2005; Bekki et al. 2005; Davies et al. 2006; Kent et al. 2007). In addition other promising techniques are being developed to find extremely low-mass halos that will likely be dark by purely gravitational effects (e.g. Trentham et al. 2001; Ibata et al. 2002; Johnston et al. 2002; Karachentsev et al. 2006; Vegetti et al. 2010, 2012; Erkal & Belokurov 2015; Nierenberg et al. 2016), and this Thesis may contribute to that group.

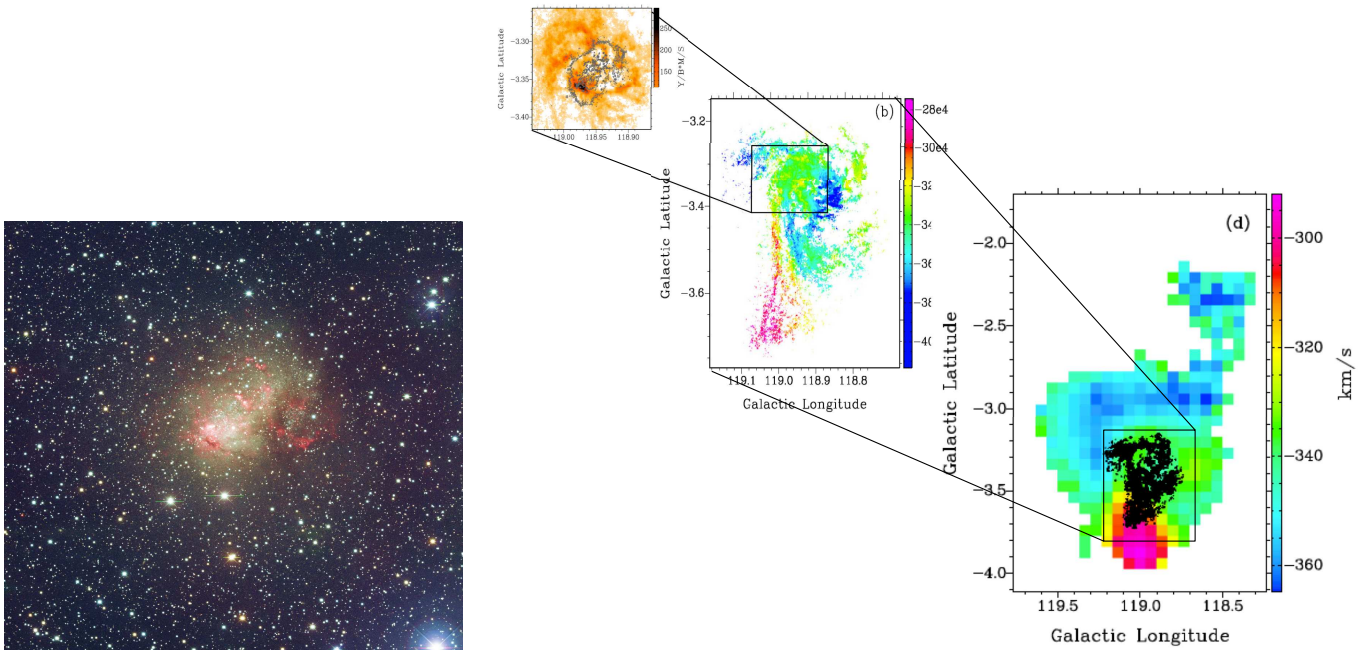

Figure 1.4 – The Local Group dwarf galaxy IC10, on the left a composite B, V, Hα image from the Lowell Observatory Local Group Survey (see e.g. Massey et al. 2007), on the right the V-band optical data (grey) embedded in the HI distribution, as observed by the VLA (left and middle panels) and GBT (right panel, with the most extended VLA data overplotted in black), with the colors in the middle and left panel indicating velocities, from Ashley et al. (2014).

1.4 This Thesis

In this Thesis we explore the effect that dark subhalos can have on dwarf galaxies. From the expectation of a decreasing stellar mass–halo mass relation toward lower masses and an increasing number of star-less halos below a certain mass scale, and the prediction from ΛCDM that the halo mass function is scale free, we infer two consequences: dwarf galaxies are more sensitive to tidal effects and external perturbers, and a predominant fraction of those perturbers will be dark.

In Chapter 2 and Chapter 3 we test these predictions with a suite of controlled simulations of disky dwarf galaxies in the mass range $M_{\rm vir} \sim 10^9$–10^{10} $M_\odot$, interacting with dark satellites with as merger mass ratio of $M_{\rm vir,sat}/M_{\rm vir,host} = 0.2$. This set-up for the dwarf galaxy is motivated by the idea that star formation mainly takes place in disks, and that this immediately allows us to test the morphological changes induced by the encounter. Chapter 2 describes a set of collissionless simulations where we explore the effects of infalling dark satellites on the morphology, structure, and kinematics of the stellar disk of a dwarf galaxy for a range of disk mass fractions. After carefully setting up the initial conditions, our experiments show that an interaction with a dark satellite can significantly perturb the dwarf galaxy, creating tidal tails and shells, thickening of the disk, and even leading to a spheroidal-like morphology. The effects of the merger are increasingly pronounced for lower disk mass fractions or equivalently, lower baryonic mass fractions. Kinematically the velocity dispersion increases and the rotational velocity decreases. For the lowest disk mass fraction considered, the final dispersion is comparable to the rotational velocity. Therefore, Chapter 2 shows that minor mergers of dwarf galaxies with a dark satellites constitute a novel channel for the formation of dwarf spheroidal galaxies, especially in the field.

Chapter 3 extends the simulations of Chapter 2 to dwarf galaxies with a gas disk. In these hydrodynamic simulations we explore the effect of the minor merger on the dwarf galaxy, and especially on the gas disk and star formation in the dwarf galaxy. We vary structural properties for the dwarf galaxy (the concentration of the dark matter halo, the virial mass and correspondingly the stellar and gas masses, the gas fraction, stellar disk thickness, and extent of the gas disk compared to the stellar disk), the dark satellite (the mass ratio with respect tot the host and the concentration of the dark matter halo), and the orbit of the satellite (inclination with respect to the dwarf galaxy stellar disk, and the initial tangential velocity which also controls the eccentricity of the orbit). Our simulations show that the minor mergers can be the cause of short, strong starbursts as well as lead to a significant long-term increase in star formation rate, major tidal tails in the gas as well as in the stellar disk, and that the thickening of the stellar disk discussed in Chapter 2 is also pronounced in the presence of a gas disk. We compare our simulated dwarf galaxies to a large

set of observed irregular dwarf galaxies and blue compact dwarfs, and show that there is important overlap in their general properties. This indicates that interactions between dwarf galaxies and their own (dark) satellites may well contribute to the diversity of the dwarf galaxy population that we see in the Universe around us.

The results of Chapter 2 and Chapter 3 indicate that dwarf galaxies are very susceptible to tidal disturbances due to their own satellites. As we expect these infalling satellites to predominantly be dark, in Chapter 4 we investigate possible methods to characterize the effects on the dwarf galaxy and compare these to observations quantitatively. To this end we gather a number of indicators from the literature that describe structural and kinematical properties of galaxies. We find that although the dwarf galaxies experiencing a merger fill a wide range of the indicators' parameter space, dwarf galaxies in isolation occupy smaller regions of the space, in particular for parameters describing the asymmetry, concentration, and central surface brightness. Noteworthy differences also occur in the indicators' parameter spaces describing inconsistent kinematics and orientation between the gas and the stars. This leads us to conclude that specific indicators characterizing the structure and kinematics of dwarfs, can help identifying which systems are experiencing a minor merger with a dark satellite. In particular highly asymmetric, or very concentrated dwarf galaxies, or dwarf galaxies with off-centered star formation, especially in the outskirts, are good candidates to be merging or post-merger systems where the secondary is dark.

A question that remains in the context of dwarf galaxies interacting with their own (dark) satellites is the fraction, for example at the present time, and the frequency of such events. In Chapter 5 we attempt to find an answer to these questions by combining a large, dark matter-only, cosmological simulation (Millennium-II Boylan-Kolchin et al. 2009, see also Fig. 1.1) with a semi-analytic galaxy formation model (see e.g. Starkenburg et al. 2013). We trace back in time the dwarf galaxies with $10^8\ M_\odot < M_{\rm vir} < 10^{10}\ M_\odot$ at the present day and $M_\star > 0$, and follow the satellites and their properties. We then compute the fraction of dwarf galaxies that have an infalling, completely dark, satellite above a given mass ratio. Our analysis shows that approximately 10% of the dwarf galaxies have experienced a merger with a dark satellite with a mass ratio large than $1:5$ for $z < 0.5$, and 27% for $z < 2$. We conclude that the possible influence of dark satellites on the evolution of dwarf galaxies is substantial and should not be neglected in considering the dwarf galaxy population.

1.5 Future outlook

Dwarf galaxies are the most dark matter-dominated systems known (Tolstoy et al. 2009; Simon et al. 2011). Hence, they provide crucial clues on the nature

of the dark matter itself. Moreover, as fragile systems, they are sensitive and possibly the most direct probes of all the important physical processes driving galaxy evolution, including galaxy interactions, the physics of gas cooling and heating, and star formation and feedback (Simpson et al. 2013; Hu et al. 2016). The relative importance of these processes and how they impact the evolution of low-mass galaxies however, still needs to be determined. This may or may not be related to the huge variety of dwarf galaxies we observe. Possible evolutionary connections between the different dwarf galaxies we see, and the exact role of environment on the formation and evolution of the morphology, structure, and kinematics of dwarf galaxies remain to be established.

Even though resolution in simulations is increasingly higher, there are still many physical processes that we do not precisely understand, as well as their impact on the lower mass scales. For example, both changes in the type of dark matter (e.g. Zavala et al. 2009; Bose et al. 2016; Vogelsberger et al. 2012; Rocha et al. 2013), as well as baryonic processes, like star formation feedback (e.g. Governato et al. 2012; Pontzen & Governato 2012), can impact the structure and internal kinematics of a dwarf galaxy. To pin these down it is necessary to perform, as realistic as possible, hydrodynamical simulations (as dark matter-only simulations seem to predict dark matter halos different in their internal structure and abundance, Sawala et al. 2013; Brooks & Zolotov 2014).

Recent and upcoming multi-wavelength surveys are providing a wealth of unprecedented data on (previously undetected) low-mass systems (e.g., DES, Dark Energy Survey Collaboration, The Dark Energy Survey Collaboration 2005; CALIFA, Sánchez et al. 2012; ALFALFA, Giovanelli et al. 2005; LITTLE THINGS, Hunter et al. 2012; SHIELD, Cannon et al. 2011; WEAVE, Dalton et al. 2014; FOCUS, Lisker et al. 2015). Another interesting development on the dwarf scale is the TiNy Titans project on grouped, paired, and isolated dwarf galaxies (Stierwalt et al. 2015; Pearson et al. 2016), which will provide extremely valuable insights in dwarf galaxy evolution. Furthermore, existing (e.g., ALFALFA, Giovanelli et al. 2005; LITTLE THINGS, Hunter et al. 2012), ongoing (e.g., SHIELD, Cannon et al. 2011) and upcoming HI surveys will provide key insights on the role of the gas in low-mass systems, and increased sensitivity in optical observations will help identify low surface brightness (dwarf) galaxies in the field (see also low surface brightness galaxies in clusters, e.g. Dalcanton et al. 1997; van Dokkum et al. 2015; Roman & Trujillo 2016), as well as features associated to mergers (e.g. Martínez-Delgado et al. 2012; Nidever et al. 2013; Cannon et al. 2014). All these observational efforts will help constrain the model discussed in this Thesis. Additionally, new, and in general more detailed, theoretical efforts are needed to combine this data with predictions from models to test and further develop our understanding of the formation and evolution of the low-mass end of the galaxy spectrum.

2

Imprints of dark satellites on dwarf galaxies

— Based on *Dark influences: imprints of dark satellites on dwarf galaxies*, T. K. Starkenburg & A. Helmi, 2015, Astronomy & Astrophysics, 575, 59 —

Abstract

In the context of the current Λ Cold Dark Matter cosmological model small dark matter halos are abundant and satellites of dwarf galaxies are expected to be predominantly dark. Since low mass galaxies have smaller baryon fractions, interactions with these satellites may leave particularly dramatic imprints. We uncover the influence of the most massive of these dark satellites on disky dwarf galaxies and the possible dynamical and morphological transformations that result from these interactions. We use a suite of carefully set up, controlled simulations of isolated dwarf galaxies. The primary dwarf galaxies have solely a stellar disk in the dark matter halo and the secondaries are completely devoid of baryons. We vary the disk mass, halo concentration, initial disk thickness, and inclination of the satellite orbit. The disky dwarf galaxies are heated and disrupted by the minor merger event, more extremely for higher satellite-to-disk-mass ratios, and the morphology and kinematics are significantly altered. Moreover, for less concentrated halos the minor merger can completely destroy the disk leaving a low-luminosity spheroidal-like galaxy instead. We conclude that dwarf galaxies are very susceptible to being disturbed by dark galaxies and that even a minor merger event can significantly disrupt and alter the structure and kinematics of a dwarf galaxy. This process may be seen as a new channel for the formation of dwarf spheroidal galaxies.

2.1 Introduction

The current Lambda Cold Dark Matter (ΛCDM) cosmological standard model predicts an abundance of small dark matter halos. A predominant fraction of these halos (with masses $< 10^9\ M_\odot$) is thought to be too small to have been able to host a galaxy because of processes such as reionization, photo-evaporation of gas, and/or supernova outflows (Gnedin 2000; Hoeft et al. 2006; Kaufmann et al. 2007; Okamoto et al. 2008; Gnedin et al. 2009; Li et al. 2010; Sawala et al. 2013) (but see also Taylor & Webster 2005; Warren et al. 2007). These halos will remain almost devoid of stars and are therefore often called dark galaxies. The existence of such dark galaxies is a possible solution to the missing satellites problem (Klypin et al. 1999; Moore et al. 1999).

The dark matter subhalo mass function at accretion is nearly self-similar. Small differences arise because smaller halos form earlier and therefore have a slightly lower normalization of the subhalo mass function at a fixed redshift (van den Bosch et al. 2005; van den Bosch & Jiang 2014). A dwarf galaxy, or small dark matter halo, will thus have a spectrum of perturbers very similar to that of an $L_\star$ or larger galaxy.

In contrast to larger systems, smaller galaxies are very inefficient at forming stars (Blanton et al. 2001; Robertson & Kravtsov 2008); therefore, the stellar-to-halo-mass ratio decreases towards lower halo masses (Moster et al. 2013; Kormendy & Freeman 2016) and dwarf galaxy baryon fractions are well below the universal baryon fraction (Gnedin 2000; Hoeft et al. 2006; Crain et al. 2007). These small galaxies thus have a subhalo mass function similar to that of larger galaxies, but have smaller baryonic components and most of their satellites can be expected to be dark (Helmi et al. 2012).

The effect of infalling satellites and mergers on the disk of a Milky Way-sized galaxy has often been studied in the past. These events lead to the heating of the disk where the amount of damage depends on the satellite-to-host-mass ratio, the initial thickness of the disk, the orbit of the satellite, and the presence of gas in the disk (Toth & Ostriker 1992; Quinn et al. 1993; Velazquez & White 1999; Font et al. 2001; Benson et al. 2004; Villalobos & Helmi 2008; Hopkins et al. 2008; Moster et al. 2010; Kim et al. 2014). Similar heating events should also take place on the dwarf galaxy scale but the results may be expected to be much more disruptive as the mass of any disk component present is much smaller than that of the heavier satellites. However, this expectation has never been modeled and tested before.

Mergers between dwarf galaxies have been discussed before (e.g., Yozin & Bekki 2012; Kazantzidis et al. 2011; Łokas et al. 2014), but never in the context of dark companions, although some recent studies have looked at the effect of significantly smaller subhalos (e.g., Bekki & Chiba 2006; Chakrabarti & Blitz 2009; Kannan et al. 2012; Lora et al. 2012; Wagner-Kaiser et al. 2014). The frequency of mergers for dwarf galaxies has primarily been studied in the

context of the Local Group. There, mergers of dwarf galaxies are prevalent before their infall into bigger, Milky Way-sized halos, but mergers between subhalos do occassionally occur after infall (Angulo et al. 2009; Klimentowski et al. 2010; Deason et al. 2014).

Intriguingly, disks of smaller galaxies have on average a thicker morphology than their larger counterparts (Yoachim & Dalcanton 2006; Sánchez-Janssen et al. 2010). This is partly expected owing to the less efficient gas cooling in smaller halos (Kaufmann et al. 2007; Robertson & Kravtsov 2008), but may have an additional origin in dynamical effects. Moreover, many local field dwarf galaxies are highly irregular and seem disturbed, or are experiencing a starburst but have no clearly detectable companion closeby (Bergvall 2012; Lelli et al. 2014b). This also seems to hold for seemingly isolated nearby galaxies (Karachentsev et al. 2006, 2008, 2011). Using very deep observations and detailed analysis a few small galaxies have recently been found to have companions (Cannon et al. 2014; Nidever et al. 2013; Martínez-Delgado et al. 2012), or to be merging, or to be the remnants of significant mergers (Ashley et al. 2013; Amorisco et al. 2014; Łokas et al. 2014).

This argumentation leads us to propose that a merger of a dwarf galaxy with a dark satellite may be an additional path to form low-luminosity dwarf spheroidal galaxies in the field or near the outskirts of more massive halos (systems perhaps akin to the Cetus and Tucana dwarf galaxies, although these are thought to be satellites of the Milky Way, or the KKR25 (Makarov et al. 2012) and KKs3 (Karachentsev et al. 2015) dwarf galaxies).

In this chapter we perform a suite of simulations of isolated minor merger events of dwarf galaxies with a dark satellite. We vary the stellar-to-halo-mass ratio of the dwarf galaxy, the initial thickness of the disk and the inclination of the satellite orbit, but keep the mass ratio between the subhalo and the host at 20%. In addition we simulate one dwarf galaxy with properties similar to that of the Fornax dwarf spheroidal as derived from the Schwarzschild models by Breddels & Helmi (2013). The model and simulation parameters are explained in Sect. 2.2 and the results are described in Sect. 2.3. In Sect. 2.4 we present a discussion, and we conclude in Sect. 2.5.

2.2 Models

We perform a set of controlled simulations of mergers between a dwarf galaxy and a dark satellite using the N-body/SPH code GADGET3 (Springel et al. 2001b; Springel 2005). The setup of these experiments is inspired in the Aquarius simulations, a suite of six cosmological dark matter simulations with very high resolution (Springel et al. 2008). This high resolution allows the identification of merger events on the dwarf galaxy scale. In these simulations we identified minor mergers with mass ratio $M_{\rm sat} : M_{\rm host} \gtrsim 2 : 10$ for field host halos.

We take the orbit of the satellite to be almost completely radial with $r_{\rm apo}/r_{\rm peri} \sim 40$. At the start of the simulations the satellite is placed at a distance of ~ 23 kpc h^{-1} from the center of the main halo with a radial velocity that is small with respect to the local circular velocity (so the satellite is initially close to apocenter) and a small (prograde) tangential velocity. The inclination of the satellite orbit with the plane of the disk is 30 or 60 degrees, similar to other studies of disk thickening (Villalobos & Helmi 2008; Moster et al. 2010).

The simulations described in this chaper are fully collisionless; simulations including gas are discussed in Chapter 3. Throughout this chapter we assume a value for the Hubble constant of $H_0 = 100h$ with $h = 0.73$ km s^{-1} Mpc^{-1}.

2.2.1 Initial conditions for the dwarf galaxy

Structure

Our main isolated models of dwarf galaxies are similar to the simulated small galaxies in Dalla Vecchia & Schaye (2008) and Schaye & Dalla Vecchia (2008). The dwarf galaxies are disky systems (Mayer et al. 2001b, 2006) embedded in a dark matter halo and initially have no gas and no bulge component.

The dark matter halo has a Hernquist (1990) profile

$$\rho(r) = \frac{\rho_0}{(r/a)(1+r/a)^3} \tag{2.1}$$

whose characteristic parameters are set by an equivalent NFW (Navarro et al. 1996) profile (Springel et al. 2005). More specifically, given the virial mass and concentration of a NFW halo, we set the Hernquist halo's total mass to $M_{\rm vir}$, and the scale radius a is derived by requiring similar inner densities (i.e., $r_s\rho_{0,\rm NFW} = a\rho_{0,\rm H}$). For a halo of $M_{\rm vir} = 1.0 \times 10^{10}\ M_\odot\ h^{-1}$ and $c = 15$ this gives a scale radius $a = 6.5$ kpc h^{-1} and $r_{\rm vir} = 35.1$ kpc h^{-1}. The chosen concentration is within the error bars of the expected concentration at $z = 0$ for a halo with $M_{\rm vir} = 10^{10}\ M_\odot\ h^{-1}$ according to the mass-concentration relations found by Macciò et al. (2008) and Muñoz-Cuartas et al. (2011).

We also model a dwarf galaxy with properties similar to the Milky Way satellite Fornax. The mass and scale radius are consistent with the dynamical models of Breddels & Helmi (2013) and the system has $M_{\rm vir}^{FNX} = 4.0 \times 10^9\ M_\odot\ h^{-1}$ and $a = 5.75$ kpc h^{-1}. Note that the concentration of the dark matter halo of this *Fornax-analog* is lower ($c = 5$) than that of the other dwarf galaxy models ($c = 15$).

As stated earlier, we assume that the stars are distributed in an exponential disk with a density profile

$$\rho_d(R,z) = \frac{M_d}{4\pi R_d^2 z_0} \exp\left(-\frac{R}{R_d}\right) \operatorname{sech}^2\left(\frac{z}{z_0}\right). \tag{2.2}$$

Table 2.1 – Initial values for all parameters

Parameters	***Disk 1***	***Disk 2***	***Disk 3***	***Fornax-analog***
Primary: halo				
$M_{\rm vir}$ $[M_\odot\, h^{-1}]$	1×10^{10}	1×10^{10}	1×10^{10}	4×10^9
$r_{\rm vir}$ $[{\rm kpc}\, h^{-1}]$	35.1	35.1	35.1	20.2
Hernquist scale radius a $[{\rm kpc}\, h^{-1}]$	6.5	6.5	6.5	5.75
Concentration c	15	15	15	5
Number of particles	1×10^6	1×10^6	5×10^6	5×10^6
Softening length $[{\rm pc}\, h^{-1}]$	18	18	15	20
Primary: disk				
$M_{\rm disk}$ $[M_\odot\, h^{-1}]$	4×10^8	2×10^8	8×10^7	3.2×10^7
Disk scale length R_d $[{\rm kpc}\, h^{-1}]$	0.566	0.566	0.566	0.688
Disk scale height z_0 thin disk $[{\rm kpc}\, h^{-1}]$	$0.1R_d$	$0.1R_d$	$0.1R_d$	$0.1R_d$
Disk scale height z_0 thick disk $[{\rm kpc}\, h^{-1}]$	$0.2R_d$	$0.2R_d$	$0.2R_d$	$0.3R_d$
Radial dispersion factor f thin disk	7.37	3.84	1.29	1.29
Radial dispersion factor f thick disk	2.77	1.44	1.0	1.0
Number of particles	1×10^5	1×10^5	1×10^5	1×10^5
Softening length $[{\rm pc}\, h^{-1}]$	6	6	6	8
Secondary: halo				
$M_{\rm vir}$ $[M_\odot\, h^{-1}]$	2×10^9	2×10^9	2×10^9	8×10^8
$r_{\rm vir}$ $[{\rm kpc}\, h^{-1}]$	26.5	26.5	26.5	19.7
Concentration c	17.25	17.25	17.25	18.91
Number of particles	5×10^5	5×10^5	5×10^5	5×10^5
Softening length $[{\rm pc}\, h^{-1}]$	12	12	12	10

The disk scale length is set following Mo et al. (1998), assuming a spin parameter for the halo of 0.033, although our halos do not rotate. We explore a range of disk masses: $M_d = 0.04 M_{\rm vir}$, $M_d = 0.02 M_{\rm vir}$, and $M_d = 0.008 M_{\rm vir}$. This allows us to test the dependence of the effect of the merger on the disk itself. In all our setups the mass of the main halo and the mass of the satellite are kept constant.

All our disks are required to be equally stable with similar Toomre-stability parameter Q,

$$Q(R) = \frac{\sigma_R(R)\kappa(R)}{3.36 G \Sigma(R)} \tag{2.3}$$

(Toomre 1964), where G is the gravitational constant, $\Sigma(R)$ is the surface density of the disk, $\kappa(R)$ the epicyclic frequency, and $\sigma_R(R)$ the radial velocity dispersion, all at radius R. The influence of the mass of the disk on the epicyclic frequency $\kappa(R)$ is negligible because the halo dominates at all radii for these systems. This implies that the Toomre Q varies with disk mass only through the surface density $\Sigma(R)$ and the radial velocity dispersion $\sigma_R(R)$.

We also explore disks with different initial scale heights $z_0 = 0.1 R_d$ and $z_0 = 0.2 R_d$. The Fornax-like dwarf galaxy has initial scale heights of $z_0 = 0.1 R_d$ (as in the standard setup) and $z_0 = 0.3 R_d$, as smaller systems are expected to be thicker because of less efficient gas cooling (Kaufmann et al. 2007; Robertson & Kravtsov 2008).

All parameters governing the structure of the systems are summarized in Table 2.1. The numerical parameters of our simulations are described in more detail in Sect. 2.2.3.

Velocity structure

The initial conditions for the dwarf galaxies are generated following Springel et al. (2005) and Hernquist (1993). In this method the moments of the velocity distribution are calculated assuming that the distribution function only depends on the energy E and the L_z component of the angular momentum. Important differences arise in our setup because the potential is dominated by the halo at all radii, and the velocity dispersions are not negligible compared to the circular velocity in a significant part of the disk. Hence the epicyclic approximation typically used breaks down not only in the very center, but also over a much larger extent of the disk.

Moreover, setting up velocities for the halo particles following a Gaussian distribution with dispersions derived from the Jeans equations leads to a configuration that is not in equilibrium in the central parts of the halo (Kazantzidis et al. 2004; Springel et al. 2005). This is negligible when a disk dominates the region under consideration, but is significant in the case of dwarf galaxies with their considerable lower disk-to-total-mass ratios.

Therefore, we determine the velocities and dispersions for the halo particles using the distribution function for a Hernquist profile neglecting the effect of the disk.

For the setup of the velocity structure of the disk we start from the Jeans equations:

$$\frac{\partial(\rho\overline{v_R^2})}{\partial R}+\frac{\partial(\rho\overline{v_R v_z})}{\partial z}+\rho\left(\frac{\overline{v_R^2}-\overline{v_\phi^2}}{R}+\frac{\partial\Phi}{\partial R}\right)=0, \tag{2.4}$$

$$\frac{1}{R}\frac{\partial(R\rho\overline{v_R v_z})}{\partial R}+\frac{\partial(\rho\overline{v_z^2})}{\partial z}+\rho\frac{\partial\Phi}{\partial z}=0, \tag{2.5}$$

$$\frac{1}{R^2}\frac{\partial(R^2\rho\overline{v_R v_\phi})}{\partial R}+\frac{\partial(\rho\overline{v_z v_\phi})}{\partial z}=0. \tag{2.6}$$

Because the halo dominates the potential at all radii we now assume that the velocity ellipsoid is aligned with the coordinate directions of the spherical coordinate system (r,θ,ϕ) instead of the cylindrical system (R,θ,z), which is the usual assumption for massive disks. In our case we can approximate,

$$\overline{v_R v_z}\simeq\left(\overline{v_R^2}-\overline{v_z^2}\right)(z/R) \tag{2.7}$$

(Binney & Tremaine 1987). In the disk ($z\sim 0$) Eq. (2.5) gives the vertical velocity dispersion

$$\rho\overline{v_z^2}=\int_z^\infty \rho\left(R,z'\right)\frac{\partial\Phi}{\partial z'}\,\mathrm{d}z'. \tag{2.8}$$

The vertical velocity dispersion in the midplane is related to the disk surface density. For an isothermal sheet $\overline{v_z^2}=z_0\pi G\Sigma\left(R\right)$ (Hernquist 1993), which would result in an exponential variation with radius. It is often assumed that this dependence with radius holds for both σ_z and σ_R, i.e., that the ratio σ_z/σ_R is constant, and that the epicylic frequency holds for all disks (Binney & Merrifield 1998; van der Kruit & Freeman 2011; Hernquist 1993; Gerssen et al. 1997; Westfall et al. 2011). This frequency is also typically used to set up a stable stellar disk for N-body simulations (Hernquist 1993; Springel et al. 2005). However, in order to have a similar Toomre stability parameter $Q(R)$ for the different disks we relax these assumptions and require that $\overline{v_R^2}=f\overline{v_z^2}$ with $f\geq 1$ constant. Using the Jeans equations to calculate the vertical velocity dispersion (see Eq. (2.8)) we can find the radial velocity dispersion and the proportionality factor f by requiring that $Q(R)\geq 2$ throughout the disk. The value $Q(R)\geq 2$ is used to avoid spontaneous bar formation following Athanassoula & Sellwood (1986) and Athanassoula (2003).

The velocity dispersions obtained in this way can have a very steep, close to exponential rise in the inner parts of the disk. This subsequently leads to

extremely high radial velocity dispersions because we set $\sigma_R^2/\sigma_z^2 = f$ with $f \geq 1$. As a consequence, this can result in an imaginary azimuthal streaming velocity (Quinn et al. 1993; Hernquist 1993) if the epicyclic approximation is used. We follow Hernquist (1993) in solving this by smoothing the velocity dispersions using $R' = \sqrt{R^2 + a_s^2}$, where a_s is the smoothing length which we set equal to half the disk scale length, $a_s = 0.5R_d$. However, unlike Hernquist (1993), we smooth only the radial velocity dispersion because the vertical velocity dispersion is determined directly from the Jeans equations (see Eq. (2.8)).[1]

We find the azimuthal velocities using the assumptions stated above and using Eq. (2.4),

$$\overline{v_\phi^2} = \frac{R}{\rho}\frac{\partial(\rho\overline{v_R^2})}{\partial R} + \overline{v_R^2} + v_c^2 - z(f_R - 1)\frac{\partial\Phi}{\partial z} + (f_R - 1)\overline{v_z^2}. \tag{2.9}$$

Finally, we need to find $\overline{v_\phi}^2$ and σ_ϕ^2, which are related to $\overline{v_\phi^2}$ through

$$\overline{v_\phi}^2 = \overline{v_\phi^2} - \sigma_\phi^2. \tag{2.10}$$

To constrain these velocities the epicyclic approximation is normally used

$$\overline{(v_\phi - v_c)^2} = \frac{\overline{v_R^2}}{\eta^2}, \tag{2.11}$$

where

$$\eta^2 = \frac{4}{R}\frac{\partial\Phi}{\partial R}\left(\frac{3}{R}\frac{\partial\Phi}{\partial R} + \frac{\partial^2\Phi}{\partial R^2}\right)^{-1}. \tag{2.12}$$

This approximation, however, is only valid when the rotational motion dominates and the velocity dispersions are small. Therefore, we use the epicyclic approximation for the outer parts of the disk from the radius where $\overline{v_\phi^2} = v_c^2$. Since $\overline{v_\phi}^2 \leq v_c^2$ must hold, but $\overline{v_\phi^2}$ is large at the center, σ_ϕ^2 is likely to be significant there. Inwards of this point we fit quadratic functions to v_ϕ and require that $v_\phi(R = 0, z) = 0$ at each z. Although the function itself is continuous we do not force continuity on the slope of v_ϕ. In that region σ_ϕ is then found using Eq. (2.10).

2.2.2 Satellites

The dark satellite has a NFW profile (Navarro et al. 1996), set up following Villalobos & Helmi (2008), using the mass-concentration relation found by

[1] This means that the radial and vertical velocity dispersions no longer have the same ratio throughout the disk, but that the proportionality factor f changes with radius, $f = f_R = \sigma_R/\sigma_z$, for the inner part of the disk.

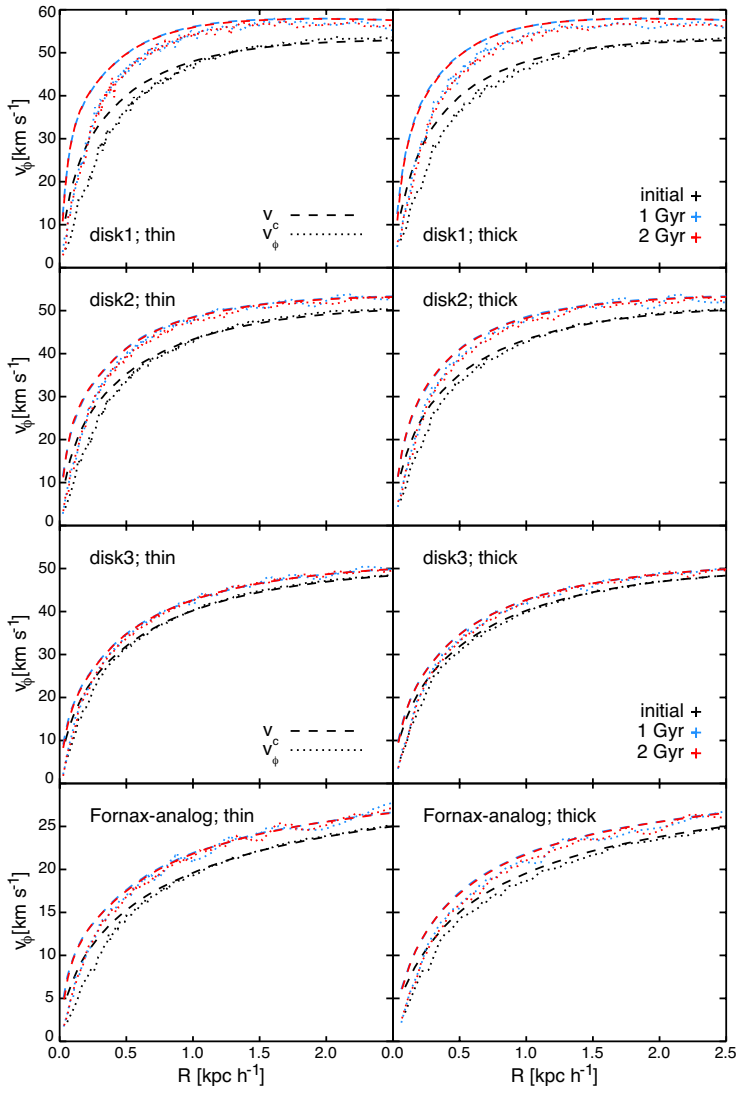

Figure 2.1 – Circular (dashed lines) and azimuthal (dotted lines) velocities of all the disks when relaxed in isolation: the initial conditions (black), after 1 Gyr (blue) and after 2 Gyr (red).

Muñoz-Cuartas et al. (2011). The satellite has a virial mass that is 20% of that of the host, $M_{\rm sat} = 2 \times 10^9\ M_\odot\ h^{-1}$, a concentration of $c = 17.25$, and has no baryonic matter at all. For the *Fornax-analog* experiment the satellite has a virial mass of $0.2 M_{\rm vir}^{FNX} = 8 \times 10^8\ M_\odot\ h^{-1}$ and a concentration of $c = 18.91$ (see Table 2.1). We compare the average density of the host, including both the halo and disk, inside the pericenter radius with the average density of the satellite within $r_{s,\rm sat}$. The ratio $\overline{\rho_{r_s,\rm sat}}/\overline{\rho_{r_p,\rm host}}$ ranges from 0.075 for *disk1*, 0.10 for *disk2*, and 0.13 for *disk3*, all with the more concentrated halo, to 0.63 for the *FNX-analog*, with the less concentrated halo.

2.2.3 Numerical parameters

The N-body systems are evolved using the code GADGET3. The number of particles used for the different components are chosen such that artificial bar formation due to graininess of the potential can be avoided and such that the ratio between the baryonic and dark matter particle masses is larger than $1:10$, to avoid numerical heating of the disk due to the dark matter halo particles. To ensure this, the systems with smaller disk masses, *disk3* and the *Fornax-analog*, have more particles in the host dark matter halo and a slightly different softening length.

To set the softening lengths we follow Villalobos & Helmi (2008) and use the prescription presented in Athanassoula et al. (2000). These authors found correlations between the optimal softening length and the mean distance from each particle to its sixth closest neighbor,

$$r_{6,\rm mean} = \left(N^{-1} \sum_{i=1}^{N} r_{6,i}^{-1} \right)^{-1}, \tag{2.13}$$

for a variety of mass distributions. We determined the optimal softening for our simulations calculating $r_{6,\rm mean}$ for our simulations after using a first guess for the softening and then comparing these values to those found by Villalobos & Helmi (2008). As our central densities and mass distributions of the individual components are very similar we find $\epsilon_{\rm opt}$ using their relation between $\epsilon_{\rm opt}$ and $r_{6,\rm mean}$. We have also checked that the derived softening lengths gave stable disk and halo profiles compared to taking slightly different values.

The criterion we use for the timestep is the standard GADGET criterion, $\Delta t = \sqrt{2\eta\epsilon/|a|}$, where we set $\eta = 0.025$ and fix the maximum timestep to 25 Myr. The total energy is conserved to within ~ 1 percent over 6 Gyr in all simulations.

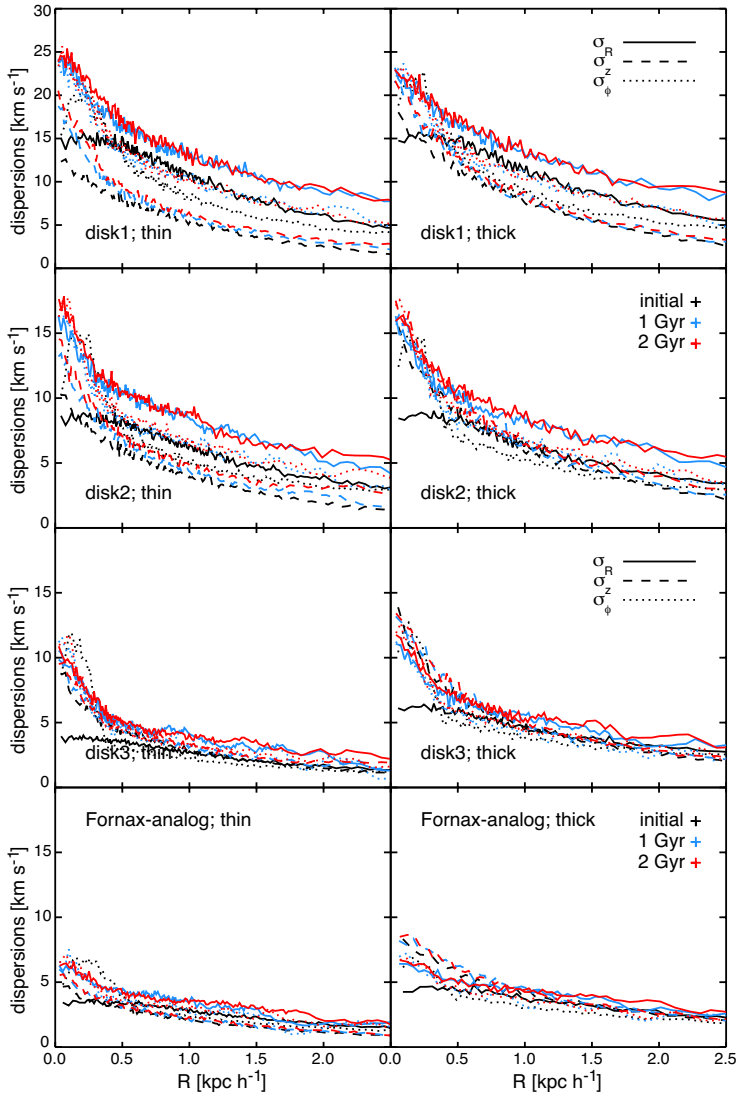

Figure 2.2 – Radial (solid lines), vertical (dashed lines), and azimuthal (dotted lines) velocity dispersions of all the disks when relaxed in isolation: the initial conditions (black), after 1 Gyr (blue) and after 2 Gyr (red).

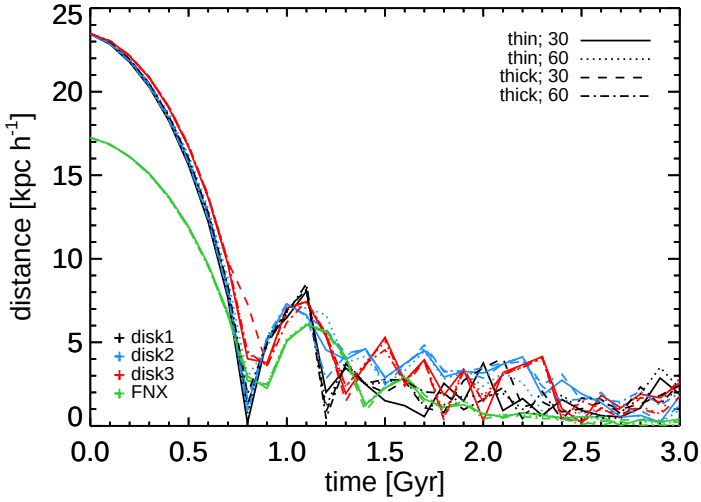

Figure 2.3 – Distance between the center of the dwarf galaxy and its satellite with time for all our simulations: the most massive disk (*disk1*; black), the intermediate disk (*disk2*; blue), the least massive disk (*disk3*; red), and the *Fornax-analog* (green) for two different inclinations of the satellite orbit with respect to the disk and two sets of initial scale heights as indicated by the top right inset. The orbits show the center of mass trajectory defined by the 100 most bound particles in the satellite. The satellite becomes completely unbound within 2 Gyr.

2.2.4 Evolution in isolation

Both the host and satellite are relaxed in isolation to ensure that they are in equilibrium before the merger. Figures 2.1 and 2.2 show the velocity structure of the host disks. The rotation and velocity dispersions are measured in cylindrical bins of variable radial bin size which contain a fixed number of 400 particles, and are close to the midplane of the disk, i.e., $|z| < 0.05$ kpc h^{-1}.

From Fig. 2.1 we note that the rotational motions of the disks do not evolve significantly. There is a slight increase in v_c and v_ϕ due to contraction of the halo, but this stabilizes very quickly. Figure 2.2 shows the velocity dispersions of the disks. It can be seen that our method to set the velocity distribution without relying on the epicyclic approximation near the center of the disks results in a small unrealistic bump in σ_ϕ at the initial time. This is caused by the approximation of the mean streaming velocity by a quadratic function where $\overline{v_\phi^2} \leq v_c^2$. The feature however dissappears quickly as the disk relaxes towards its equilibrium configuration.

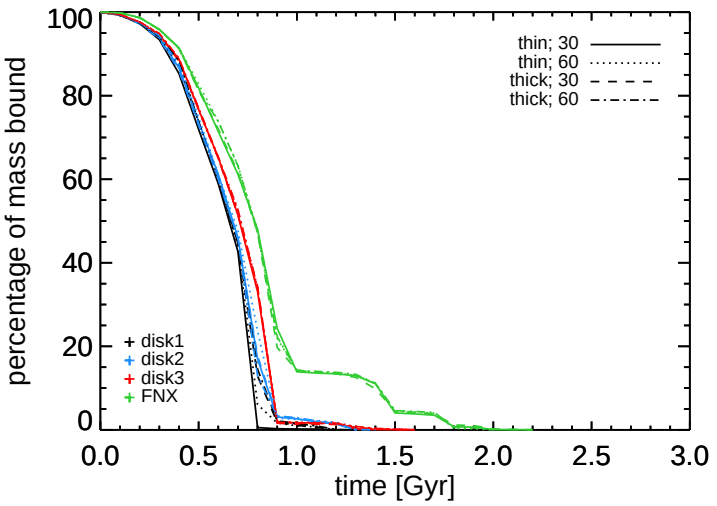

Figure 2.4 – Percentage of mass still bound to the satellite as a function of time for all simulations consisting of four different dwarfs each with two different initial scale heights and two different orbits for the satellite: the most massive disk (*disk1*; black), the intermediate disk (*disk2*; blue), the least massive disk (*disk3*; red), and the *Fornax-analog* (green). The color and line coding is the same as in Fig. 2.3.

2.3 Results

Figure 2.3 shows the orbits of the satellite for the different dwarf galaxies. At each snapshot we determine the center of the satellite by computing the center of mass using its 100 most bound particles. The satellite sinks in very quickly through dynamical friction to the central regions of the host where it is fully disrupted in a few passages.

This is shown in Fig. 2.4 where we have plotted the total mass that is still bound to the satellite as a function of time. For all three systems with the more massive halo ($M_{\rm vir} = 1 \times 10^{10}\ M_\odot\ h^{-1}$) the satellite becomes almost completely unbound before the second pericenter. The satellite is more severely stripped when falling into the primary with a more massive disk although the differences are marginal. This is reflected in Fig. 2.4 in the red lines lying above the blue lines which lie above the black lines. This is an indication that the disk mass slightly influences the minor merger process.

2.3.1 Morphological changes

Substructure

The morphology of all the dwarf galaxies changes because of the merger as can be seen in Fig. 2.5 (for the two most massive disks) and Fig. 2.6 (for the least massive disk and the *Fornax-analog*). In these figures we show the thinner disks – both face-on and edge-on – before, during, and after the merger in steps of 2 Gyr for the satellite on the orbit with an inclination of 60 degrees. In general, all the disks tilt during the merger. For all plots in this chapter, however, the galaxies are oriented in such a way that the direction of total angular momentum of all disk particles within the half-mass radius is parallel to the z-axis.

An envelope of stars coming from the disk itself can be found around the disks in these plots. The lower mass disks end up with larger and more densely populated envelopes than the higher mass disks. All the disks have experienced thickening (see also Sects. 2.3.1 and 2.3.1) while largely retaining the disky appearance except for the *FNX-analog*. *Disk1* develops irregular spiral arms and a strong bar during the merger. The least massive disk on the other hand, is more clearly disturbed by the merger and develops spiral arms and tilts very strongly. A comparison of the most and least massive disks shown in the top panels of Figs. 2.5 and 2.6 gives an indication of the very different effects of the satellite on a disk of $4 \times 10^8\ M_\odot\ h^{-1}$ and a disk of $8 \times 10^7\ M_\odot\ h^{-1}$ in dark matter halos of exactly the same mass.

As just mentioned, as a consequence of the merger the *Fornax-analog* system cannot be called a disky dwarf galaxy from after the second pericenter of the satellite. From an initially stable disk the galaxy first becomes lopsided with warps and irregular structure in the disk, subsequently becomes completely disturbed, and finally more closely resembles a spheroidal system as shown in the left-hand plots in the last two rows of Fig. 2.6.

The later snapshots of *disk3* and the *Fornax-analog* in Fig. 2.6 show an abundance of tidal debris that is distributed in shells and plumes. This debris comes from the disk itself as the satellite does not have any stars. Some of the shell structures that are formed during the merger are very similar to structures observed around external galaxies and are thought to be formed by secondary galaxies falling in. These simulations show that these structures can also be from the primary object itself if the merger event is significant enough.

Figures 2.7 and 2.8 show the surface brightness of the disks, face-on and edge-on. Since magnitudes are given on a logarithmic scale the density changes are much more clearly visible than in Figs. 2.5 and 2.6. Typically, particle plots emphasize the small-scale structures that emerge during the interaction, but fail to show the density contrasts closer to the center of each galaxy. On the other hand, the surface brightness maps are smoothed maps of the density distribution and so the small-scale structures in the outskirts

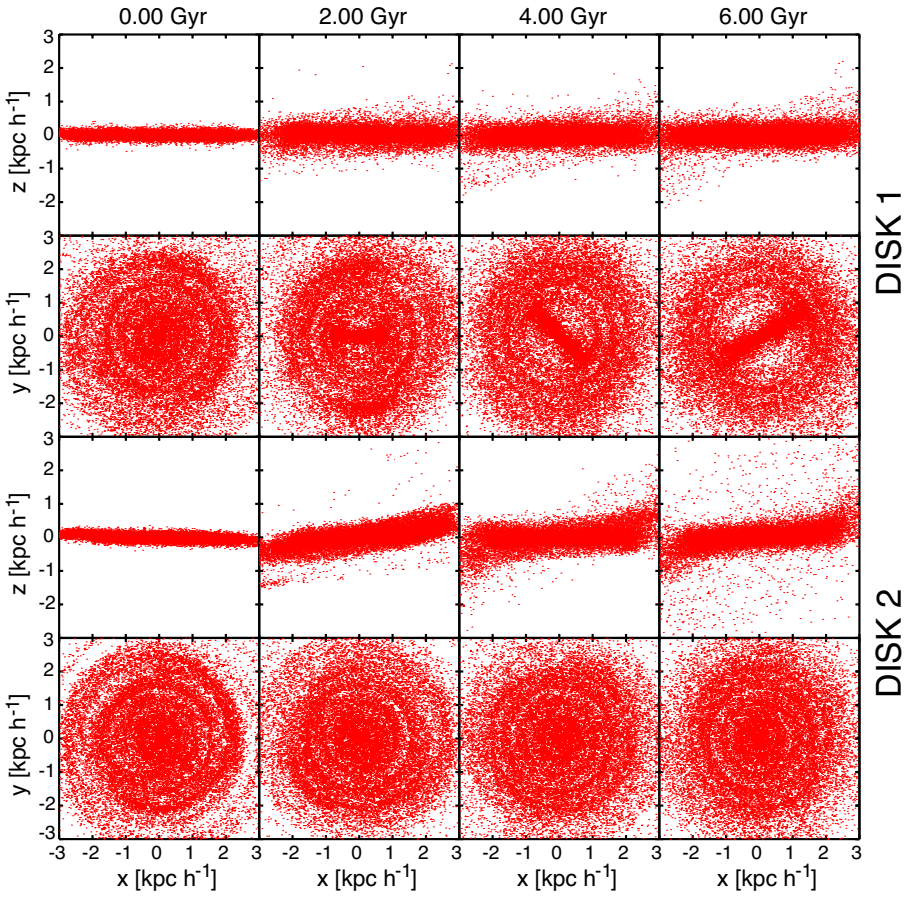

Figure 2.5 – Edge-on and face-on particle distributions of the two most massive disks before the merger (left) up to around 5 Gyr after the first pericenter of the satellite (6 Gyr; right) in steps of 2 Gyr. The orbit of the satellite has an inclination of 60 degrees. The top two panels are for the most massive disk (*disk1*), and the bottom two for the intermediate disk (*disk2*), both with $z_0 = 0.1R_d$ initially. The first and third row show the disks edge-on and the second and fourth row show the disks face-on. To show the features better we plot 5% of the particles within 0.5 kpc h^{-1}, 10% for radii between 0.5 and 1.0 kpc h^{-1}, 20% for radii between 1.0 and 1.5 kpc h^{-1}, and 50% with radii between 1.5 and 2.0 kpc h^{-1}; every particle is plotted for larger radii.

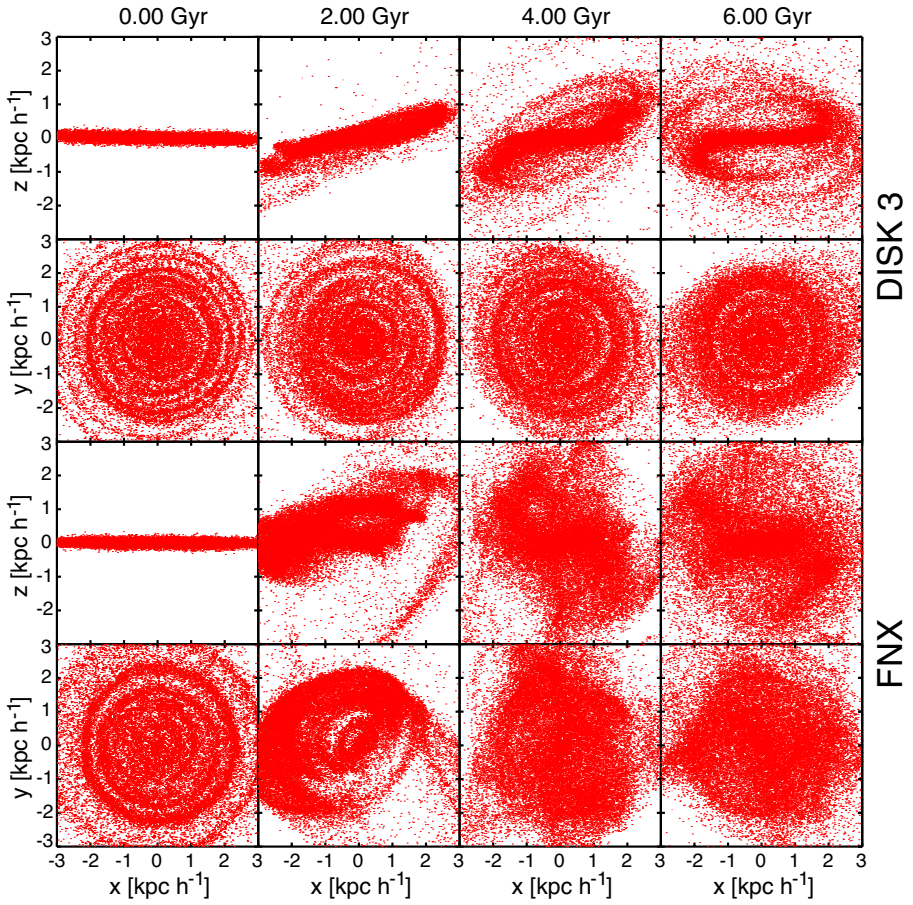

Figure 2.6 – Edge-on and face-on particle distributions of the two least massive disks before the merger (left) up to around 5 Gyr after the first pericenter of the satellite (6 Gyr; right) in steps of 2 Gyr. The orbit of the satellite has an inclination of 60 degrees. The top two panels are for the least massive disk (*disk3*), and the bottom two for the *FNX-analog*, both with $z_0 = 0.1R_d$ initially. The first and third row show the disks edge-on and the second and fourth row show the disks face-on. To show the features better we plot 5% of the particles within 0.5 kpc h^{-1}, 10% for radii between 0.5 and 1.0 kpc h^{-1}, 20% with radii between 1.0 and 1.5 kpc h^{-1}, and 50% of the particles with radii between 1.5 ans 2.0 kpc h^{-1}; every particle is plotted for larger radii.

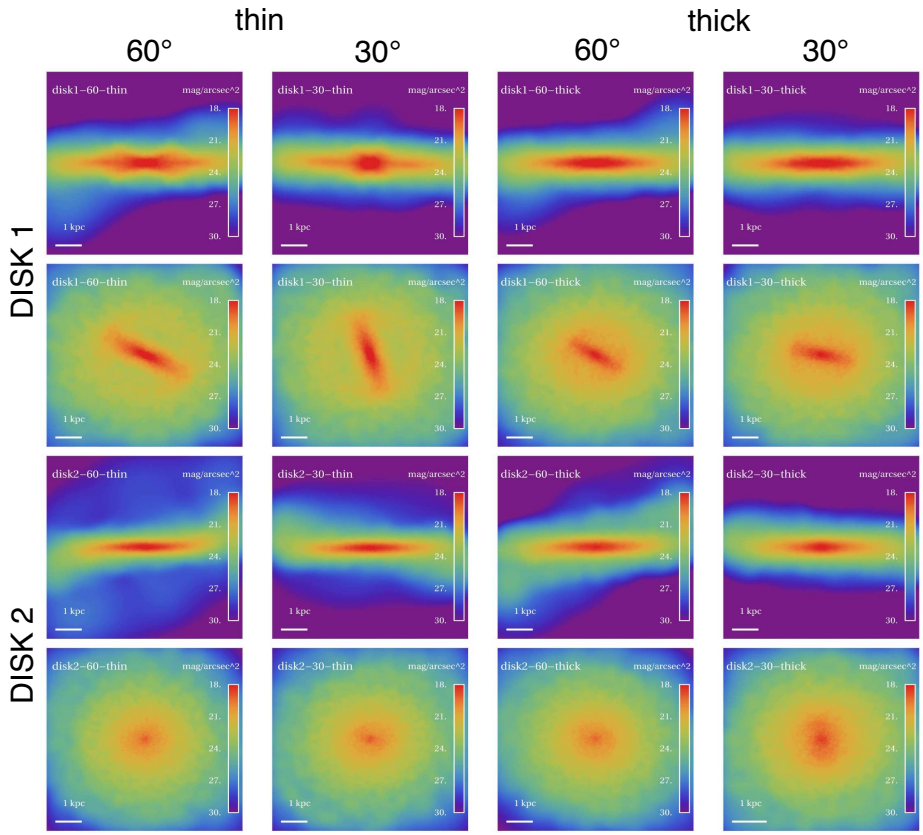

Figure 2.7 – Face-on and edge-on surface brightness maps of the final snapshots for the simulations with the two most massive disks (top: *disk1*, bottom: *disk2*). The first two columns are for $z_0 = 0.1R_d$, while those on the right have $z_0 = 0.2R_d$ initially. The first and third columns are for the 60-degree inclination satellite, the second and fourth for the 30-degree.

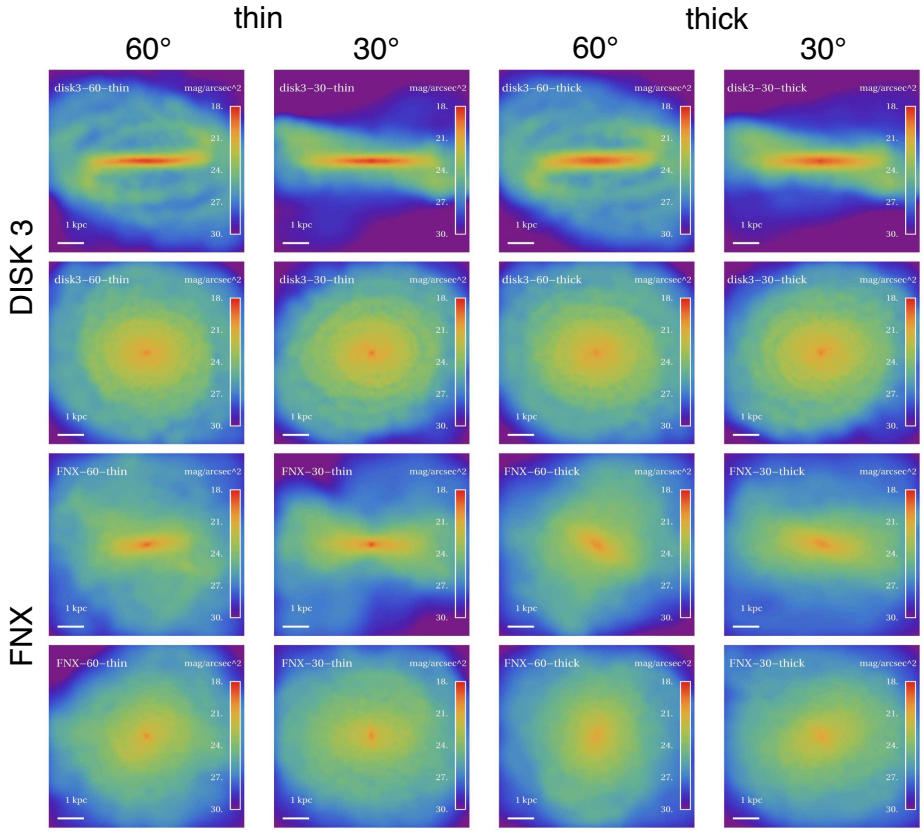

Figure 2.8 – Face-on and edge-on surface brightness maps of the final snapshots for the simulations with the two least massive disks (top: *disk3*, bottom: *Fornax-analog*). The first two columns are for $z_0 = 0.1R_d$, while those on the right have $z_0 = 0.2R_d$ for *disk3*, and $z_0 = 0.3R_d$ for the *FNX-analog* initially. The first and third columns are for the 60-degree inclination satellite, the second and fourth for the 30-degree.

are mostly lost. However, the density contrasts in the galaxies themselves are very well represented in the surface brightness maps. We compute densities by smoothing over 128 neighbors and assume a M/L ratio of 2 for all star particles in all simulated galaxies.

It is instructive to compare the right columns of Figs. 2.5 and 2.6 with the left columns of Figs. 2.7 and 2.8, respectively. Figures 2.7 and 2.8 show surface brightness maps of the final snapshots of each simulation, of which the leftmost column corresponds to the simulations with initially thin disks and the satellite on the 60 degrees orbit. The density gradients in the central parts of all the systems, the bars developed in the *disk1*s, and the spiral structures and the warps in the *disk3*s, are evident in Figs. 2.7 and 2.8. Figure 2.8 also shows that the *FNX-60-thin* remnant is still a somewhat oblate system, but that this is not true for the same setup with an initially thicker disk (*FNX-60-thick*).

The resulting surface brightness maps in Figs. 2.7 and 2.8 can, in principle, be compared to observations. Photometric images currently go down to a surface brightness of approximately 26–$27\ \mathrm{mag/arcsec^2}$ (see , e.g., Coleman et al. 2004; Martínez-Delgado et al. 2012) but occasionally go deeper as for example Hunter et al. (2011), who use azimuthally averaged surface brightness profiles to reach a surface brightness of $\mu_V = 28$–$31\ \mathrm{mag/arcsec^2}$.

The bars in all the most massive disks should all be apparent in photometric observations reaching such depths. Some of the debris around the disks, for example for *disk3-60-thin* or *disk3-60-thick*, and some subtler substructure or spiral patterns in the disks would probably also be visible. On the other hand, most of the envelopes around the disks that have formed because of the mergers, and most of the shell features and other substructure in those envelopes will only be visible by using very deep photometry. The *Fornax-analog*s all have shells in the denser part of the stellar distributions as well. These may be visible in high-quality photometric images.

All the disks in the $M_{\mathrm{vir}} = 10^{10}\ M_{\odot}\ h^{-1}$ halos have higher central surface brightness than the Local Group dwarf galaxies (excepting the LMC and SMC), but they are also much more massive. The galaxies closest to the simulated $10^{10}\ M_{\odot}\ h^{-1}$ system are IC4662 and NGC6822 (McConnachie 2012). The *Fornax-analog* has a much lower final central surface brightness than the more massive systems, especially initially, and is comparable in surface brightness to the dwarf galaxies in the Local Group in general and the Fornax dwarf galaxy in particular (McConnachie 2012).

Inner and global shape

The difference in the final morphology of the systems can also be seen when fitting an ellipsoid to the stellar mass distribution of the particles in the

simulation. We compute the shape tensor

$$S_{ij} = \sum_k (r_k)_i (r_k)_j, \tag{2.14}$$

where $(r_k)_j$ denotes the j-component of the position vector of particle k. The tensor S_{ij} is often used with a normalization by the ellipsiodal radius of the particles within the coordinate system of the ellipsoid (see, e.g., Allgood et al. 2006), but this effect is the subject of debate (Zemp et al. 2011). We do not normalize and therefore effectively give more weight to the outskirts. Figure 2.9 shows the change in the intermediate/major (b/a; top) and minor/major (c/a; bottom) axis ratios for all particles within ellipsoids with major axes of 1 (left) and 3 (right) kpc h^{-1}. The smaller ellipsoid thus focuses on the change in shape in the inner parts of the remnants, while the panels on the right show the changes in the shape of the total disk (within an ellipsoidal radius of 3 kpc h^{-1}, so including the inner parts as well). Note that in Eq. (2.14) we do not have to take into account the mass of each particle as the mass of all disk particles is the same.

The top left panel of Fig. 2.9 shows that most systems have lower b/a axis ratios at the end of the simulation that are due to the presence of bars in the case of the most massive disks. The most extreme cases (both thin *disk1*s) have final average $b/a_{1\mathrm{kpc}} \sim 0.3$ and the least massive bar of these simulations (*disk1-60-thick*) still has a final average $b/a = 0.81$ within an ellipsoidal radius of 1 kpc h^{-1}. The isolated *disk1* evolved on a longer timescale also develops a bar. During the merger the bar greatly increases in mass, however, and has a major axis of around 1 kpc h^{-1}, which extends beyond the half-mass radius of the remnant ($r_{1/2} \sim r_{1/2_{\mathrm{initial}}} \sim 0.8$ kpc h^{-1}).

The bar in *disk1* is also seen in the final intermediate-to-major-axis ratio within an ellipsoid of 3 kpc h^{-1} because of its contribution to the inner parts. Although the axis ratios stay close to $b/a \sim 1$ for *disk2* and *disk3* there is also substructure in the inner disks of these systems (see Figs. 2.7 and 2.8), but not massive enough to define the average shape of the disks. However, the final b/a ratio at larger radii is less axisymmetric for both of the *disk3*s with the satellite on the 60 degree orbit, probably because of the significant tilt of the disk during the merger and the resulting warps.

All *Fornax-analog*s are no longer axisymmetric in the final snapshot as their intermediate-to-major-axis ratio drops to $b/a \sim 0.8$–0.9 (depending on location and experiment). Nevertheless, when these relatively small changes in the intermediate-to-major-axis ratios are compared to the changes in the minor-to-major-axis ratios one notices that the shapes of all the *FNX-analog* systems evolve drastically. Overall, these changes in the minor-to-major-axis ratios are very diverse. The bottom panels of Fig. 2.9 show that some of the *FNX-analog* systems would be classified as spheroidal or elliptical; their total minor-to-major-axis ratios increase sharply with factors ranging from almost 3 to almost

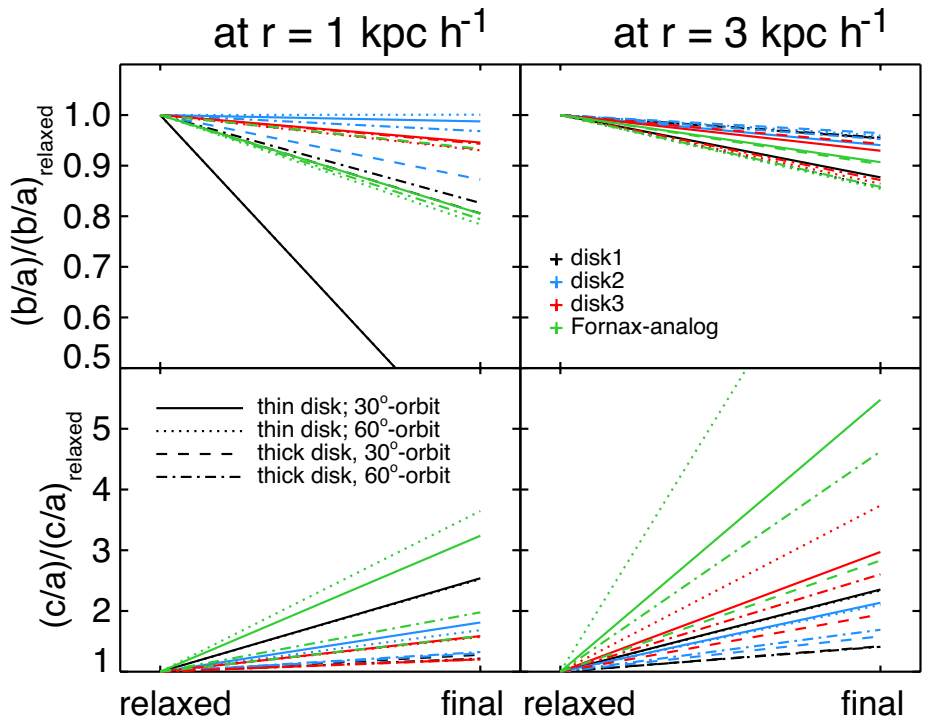

Figure 2.9 – Relative increase in principal axis ratios between initial and final snapshot for all merger simulations. Top: intermediate axis over major axis (b/a); bottom: minor axis over major axis (c/a). The axis ratios are computed with the major axis length equal to 1 kpc h^{-1} for the panels on the left and equal to 3 kpc h^{-1} for the panels on the right. Shown are 16 simulations of four disky dwarf galaxies with two sets of initial scale heights and two different satellite orbits: the most massive disk (*disk1*; black), the intermediate disk (*disk2*; blue), the least massive disk (*disk3*; red), and the *FNX-analog* (green). The color and line coding is the same as in Figs. 2.3 and 2.4. Note that the b/a and c/a values are relative to the initial value so they can both become greater than 1.

10. The initial $c/a \sim 0.06$ (thinner system) and $c/a \sim 0.16$ (thicker system) result after a minor merger in final values in the range $c/a \sim 0.31$–0.73.

The axis ratios plotted in Fig. 2.9 are with respect to the values after relaxation, before the merger, and thus show that the heating of the disks is due to the minor merger and not to numerical artifacts. The thickening due to relaxation of the initial disks is very minor. The *disk1*s and *disk2*s have relaxed axis ratios of $c/a \sim 0.075$ for the thin disks and $c/a \sim 0.115$ for the thick disks instead of the initial $c/a \sim 0.05$ (thin) and $c/a \sim 0.10$ (thick). As a second check we simulated the disks without a merger over the same complete time period, and found no significant changes. As explained earlier, only *disk1* develops a massive bar in isolation.

Both the initially thinner and thicker *FNX-analog* systems merging with the satellite on the 60 degree orbit have $c/a > 0.5$ while also having lower b/a-values: $c/a_{\rm FNX-60-thin} \sim 0.55$ compared to $b/a_{\rm FNX-60-thin} \sim 0.85$ and $c/a_{\rm FNX-60-thick} \sim 0.73$ compared to $b/a_{\rm FNX-60-thick} \sim 0.85$. The *FNX-analog* systems with the satellite on a 30 degree orbit have lower final global minor-to-major-axis ratios, $c/a \sim 0.31$ for the initial thinner and $c/a = 0.45$ for the initial thicker system, and are slightly triaxial with $b/a \sim 0.90$. This means that this object viewed from a random angle has an observational axis ratio that is greater than or equal to 0.3.

For all systems, *disk1*, *disk2*, *disk3,* and *FNX-analog*, the thinner disk experiences more thickening in a relative (but not absolute) sense than those that were thick initially. This holds for the final and initial minor-to-major-axis ratios for just the inner regions and for the whole remnant. For *disk1*, especially the initially thinner disks, the increase in disk height is probably dominated by the formation of the substantial bars. Otherwise c/a increases more for the less massive disks than for the more massive disks; the increase in c/a is inversely ranked by mass. This reflects the fact that a less massive disk is more prone to significant perturbations by the incoming satellite and so dwarf galaxies with smaller baryon fractions are more easily disturbed and will more often have thickened or perturbed morphologies (as also shown in Figs. 2.5 to 2.8).

Radial and vertical density profiles

In the top panels of Fig. 2.10 we plot the vertical density profiles of the *60-thin* simulations for all systems. We define the plane of the disk to be perpendicular to the total angular momentum vector of all stellar particles within the half-mass radius of the stellar remnant. The vertical density profiles of the remnant systems are not well described by the initial sech^2 function. This can be seen through a comparison to the dotted lines which correspond to a maximum likelihood fit to a sech^2 profile.

The top right panel shows the density profile of the initially thinner *FNX-analog* system during the merger simulation with the satellite on the orbit with an inclination of 60 degrees. After 1 Gyr there are already significant deviations from a sech^2 profile. The second panel in the top row shows that for *disk2-thin-60* the vertical density profiles broadens, but can still be approximately described by a sech^2 function even close to the time of the merger itself (around 1–2 Gyr) and at the end of the simulation (6 Gyr). The top left panel shows that for *disk1* the disk thickens more after the actual merger and that the changes in the vertical density profile are strong because of the formation of a massive bar.

The *disk3* (top row, middle right panel) has a significant amount of mass at large radii that corresponds to the extended envelope seen in Fig. 2.6 in all *disk3* simulations after first pericenter, and this renders a much worse sech^2 fit. For *disk2* and *disk1* this is much less the case, although as stated earlier a

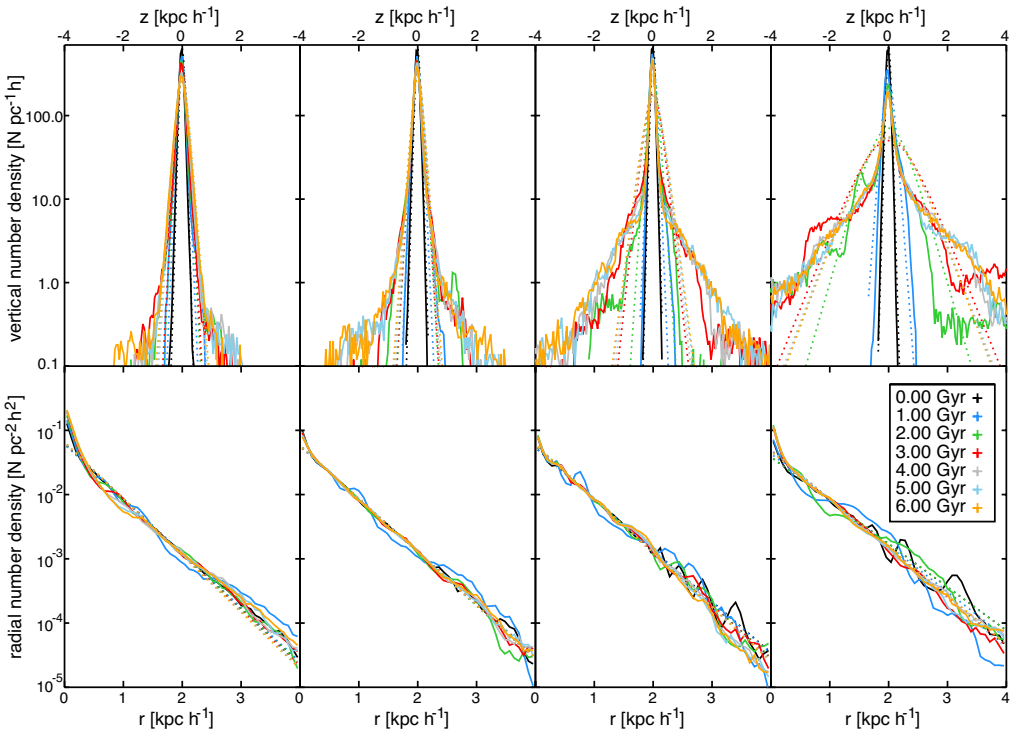

Figure 2.10 – Evolution of the vertical and radial density profiles for the different thin disks ($z_0 = 0.1R_d$ initially) with the satellite on the 60 degree orbit: *disk1* (left), *disk2* (middle left), *disk3* (middle right), and *FNX-analog* (right). Density profiles (solid lines) are shown for the initial relaxed disk (0 Gyr) up to 6 Gyr later (about 5 Gyr after the first pericentric passage of the satellite) in steps of 1 Gyr. The dotted lines in the top row show the maximum likelihood sech^2 profiles; in the bottom row the same for an exponential profile, taking into account all disk particles.

sech^2 functional form does not accurately reproduce the vertical structure of our remnants.

The progressively worse fits to the sech^2 function, going from *disk1* to *FNX-analog* are due to the increased importance of extra-planar material, which is manifested in extended wings. One can argue that just as in the case of Milky Way-like simulations discussed in the literature, a second thicker component has formed as a result of the merger.

The bottom panels of Fig. 2.10 show the radial surface density profiles with time in steps of 1 Gyr. Note the significant disturbance in all disks around the time of first pericenter (blue lines). The lower mass disks have some spiral structures initially and fall off more steeply than exponential profiles in the outskirts at later times. The most massive disk (*disk1*; leftmost panel in Fig. 2.10), on the other hand, shows a growing overdensity in the very center which corresponds to the massive bar forming in the inner parts of these remnants. Even the remnant of the *FNX-analog* can still be reasonably well fitted by a radial exponential profile as indicated by the dotted lines.

Comparison to other work on disk thickening

We compare our results of the thickening of disks due to minor mergers with a number of results from the literature. To this end we measure the thickness of our systems between 2 and 3 disk scale lengths (which would correspond to the solar neighborhood in the case of a Milky Way-like simulation). We compute two commonly used estimates of the thickness of a disk: the standard deviation of the vertical distribution of particles, $\langle z^2 \rangle^{1/2}$ (Velazquez & White 1999), and a Bayesian maximum likelihood estimate assuming a sech^2-profile.

If the vertical density profiles are accurately described by the function $\frac{1}{\pi z_0}\,\mathrm{sech}^2\left(\frac{z}{z_0}\right)$ then $\langle z^2 \rangle^{1/2} = \frac{\pi}{2\sqrt{3}} z_0$. Therefore, a comparison of these two different measures gives an indication of how far the disk still follows a sech^2. The results can be found in Table 2.2. Here we list the initial values for the scale heights of the disks (after relaxation in isolation), as well as those after the merger. For *disk1* and *disk2* the thinner disks depict a larger increase in scale height than their corresponding thicker disks (although in an absolute sense the latter are thicker at the final time), and that the scale heights of all *disk1*s increase significantly as a result of massive bars. For the lower mass disks the mean scale height increases most in simulations with the satellite on the 60 degree orbit.

Figure 2.11 shows the ratio of the difference in the vertical second moment $\Delta\langle z^2 \rangle^{1/2}$ to the initial scale length of the disk versus the ratio of the total mass of the satellite and the mass of the disk. In this figure we have added results from minor merger simulations from the literature, specifically from Velazquez & White (1999), Villalobos & Helmi (2008), and Moster et al. (2010). To make the information provided by all these studies uniform, we derive

Table 2.2 – Estimates for the scale height z_0

System	time and satellite orbit	z_0 from max-likelihood $[\mathrm{kpc}\ h^{-1}]$	z_0 from $\langle z^2\rangle^{1/2}$ $[\mathrm{kpc}\ h^{-1}]$
disk1-thin	relaxed	0.08	0.08
	final30	0.20	0.20
	final60	0.18	0.19
disk1-thick	relaxed	0.12	0.12
	final30	0.17	0.17
	final60	0.16	0.16
disk2-thin	relaxed	0.08	0.08
	final30	0.15	0.15
	final60	0.14	0.14
disk2-thick	relaxed	0.12	0.12
	final30	0.19	0.19
	final60	0.17	0.17
disk3-thin	relaxed	0.06	0.06
	final30	0.14	0.15
	final60	0.23	0.46
disk3-thick	relaxed	0.11	0.11
	final30	0.17	0.18
	final60	0.28	0.49
FNX-thin	relaxed	0.08	0.08
	final30	0.65	0.86
	final60	1.33	1.37
FNX-thick	relaxed	0.20	0.20
	final30	0.92	1.10
	final60	1.25	1.26

Notes The scale height z_0 is estimated assuming a sech^2 function (see Eq. (2.2)) for the vertical density profile.

$\Delta\langle z^2\rangle^{1/2}$ assuming that the vertical density distribution in the simulations from Villalobos & Helmi (2008) and Moster et al. (2010) is well represented by a sech^2 function. The four *FNX-analog*-disks have such a large increase in $\langle z^2\rangle^{1/2}$ that they fall completely outside the plot range (see Table 2.2).

It has been proposed that the heating in disk galaxies caused by minor mergers depends linearly (Toth & Ostriker 1992; Mo et al. 2010) or quadratically (Hopkins et al. 2008) on the ratio $M_{\mathrm{sat}}/M_{\mathrm{disk}}$. With the exception of this

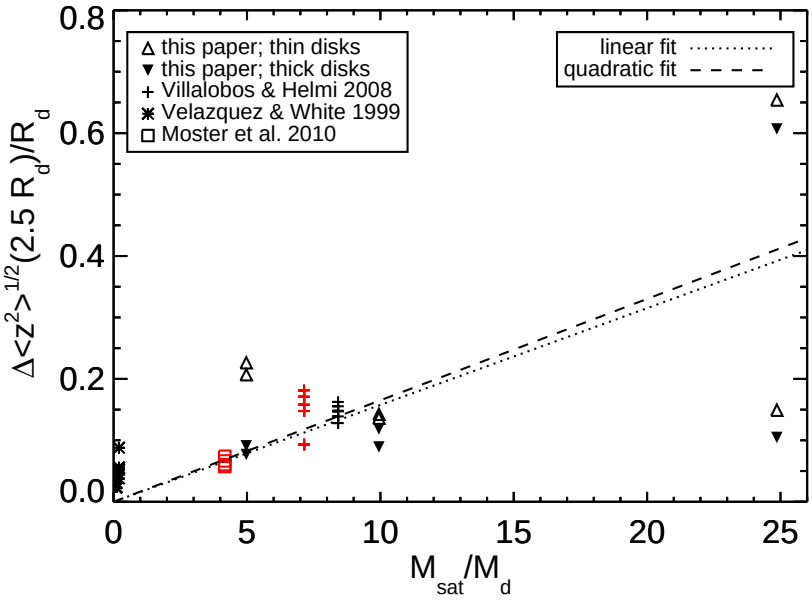

Figure 2.11 – The change in vertical second order moment of all star particles located near $2.5R_d$ (the solar radius in a Milky Way-like host), normalized by disk scale length, versus the ratio of satellite mass to host disk mass for all simulations presented here. In addition we have included results from the literature for similar studies of minor mergers. The *FNX-analog* simulations are not presented because they fall above the vertical range of this plot. The red symbols indicate that the values were read off from a plot and not taken from a table in the paper in question. Triangles pointing upward denote initially thinner disks, while the initially thicker disk are denoted by downward pointing triangles. The dotted and dashed lines show a linear and quadratic fit, respectively, to the mean values of all $M_{\rm sat}/M_{\rm disk}$ bins.

thesis, all studies so far have modeled Milky Way-like disk galaxies disturbed by satellites that are small or at best comparable with respect to the disk. The mergers discussed here, however, have $M_{\rm sat}/M_{\rm DM;host}$ constant and vary $M_{\rm disk}$, with $M_{\rm disk} << M_{\rm sat}$.

We apply a least squares fit to all data points in Figure 2.11 for a quadratic (with the coefficient of the quadratic part forced to be positive as predicted by Hopkins et al. (2008)) and a linear dependence on $M_{\rm sat}/M_{\rm disk}$. We use the mean values of the points per mass bin and exclude the extreme points of the *FNX-analog*s. For our simulations the relation now solely depends on $M_{\rm sat}/M_{\rm disk}$. As can be seen from Fig. 2.11 the scatter is very large, the obtained fits are quite similar, and unsurprisingly neither is very good. The reason for this is that the heating of stellar disks by infalling satellites does not solely depend on their mass ratios. For example, the initial structure of the disk and the presence

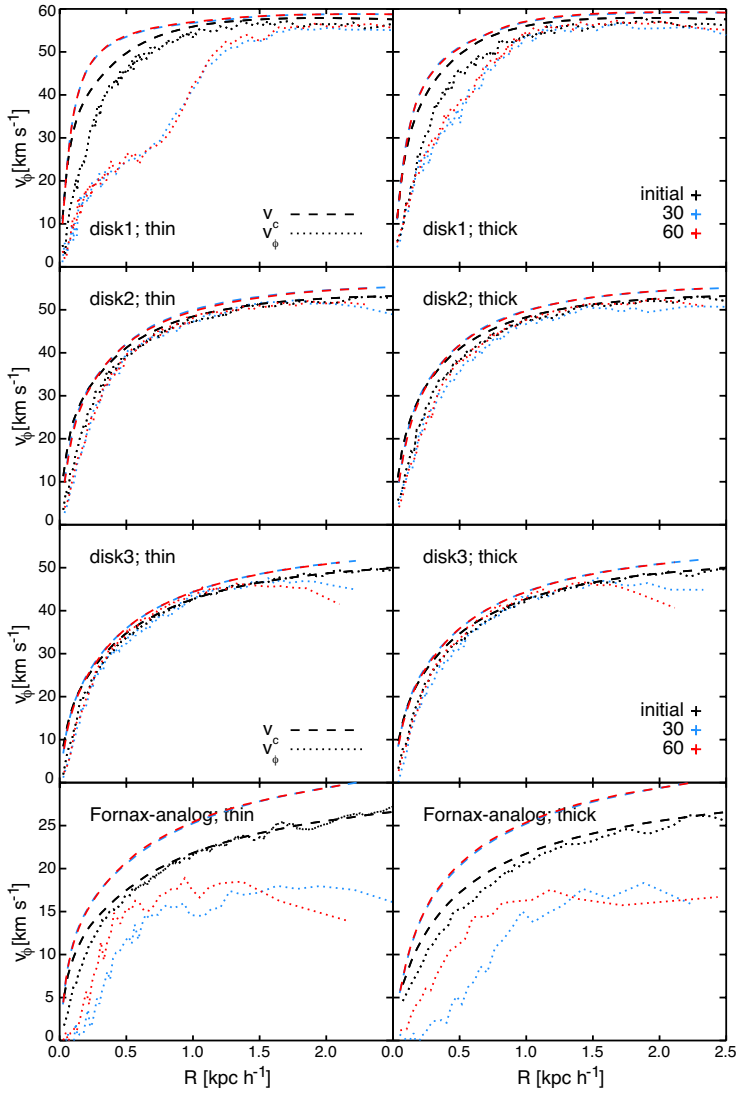

Figure 2.12 – Circular velocity (dashed lines) and average rotation (dotted lines) of all the disks before the merger (black) and 6 Gyr later for both orbits (30-degree inclination in blue, and 60-degree inclination in red). In all cases the disks are first aligned such that the total angular momentum vector of all particles within the half-mass radius of the disk is perpendicular to the plane in which the average rotational velocity is measured. All particles considered have $|z| < 0.05$ kpc h^{-1} and the bins have a variable bin size, but a fixed number of 400 particles each.

of gas in the disk, as well as the orbit of the satellite, have a very significant influence on the response of the disk on the infalling satellite (e.g., Moster et al. 2010). Moreover, the measurement of heating in different studies is done using different methods and assumptions. Although we have attempted to homogenize this as much as possible, additional scatter is introduced (e.g., in the case of the *FNX-analog*s the disk is fully destroyed and the characterization by a sech^2 is very poor). From Fig. 2.11 it is clear that these uncertainties dominate for the larger $M_{\rm sat}/M_{\rm disk}$ ratios.

The parameters of the linear term are almost the same for both the linear and quadratic dependence on $M_{\rm sat}/M_{\rm disk}$ (with the coefficient of the quadratic term six orders of magnitude smaller than the coefficient of the linear term: $y = 0.016x$ versus $y = 0.017x + 9.1\mathrm{e}^{-10}x^2$). Although this study is limited in number, and the scatter in the relation is very significant, it suggests that to the first order the heating of galactic disks by minor mergers as a function of $M_{\rm sat}/M_{\rm disk}$ can be sufficiently described with a linear model.

2.3.2 Kinematical changes

The changes induced by the merger events on the rotational velocity and velocity dispersions of the host galaxies can be seen in Figs. 2.12 and 2.13. Note that in all cases the circular velocity has increased owing to the mass deposited by the accreted satellite in the inner parts of the halo. For all the *disk1*s additional changes are mostly due to the massive bar that forms in these systems. The bar leads to the characteristic linear $v_\phi(R)$ relation of solid body rotation, and a steepening of the circular velocity curves for small R. For *disk2* and *disk3* the rotational velocities do not change significantly. In the case of *disk3* the rotational velocity drops in the outer parts where the disk is most perturbed. For the *FNX-analog* the evolution is stronger and the rotational velocity has clearly decreased. In the initially thicker disk cases, the peak rotation in the region within the stellar half-mass radius ($\sim$ 15 km s^{-1} and $\sim$ 12 km s^{-1}) is very close in magnitude to the average line-of-sight velocity dispersions in the same region ($\sim$ 10–14 km s^{-1} with $\sigma_{\rm l.o.s.} = \sqrt{\sigma_R^2 + \sigma_z^2 + \sigma_\phi^2}/\sqrt{3}$). For the initially thinner disks, the peak rotation is only a few km s^{-1} higher ($\sim$ 16 km s^{-1} and $\sim$ 18 km s^{-1}). When observing such a system, and depending on the spatial extent of the data, one could probably conclude there is hardly any rotation present.

All velocity dispersions increase for all the disks. For *disk1* and *disk2* the increase is larger in the inner parts than in the outskirts, especially for *disk1-thin* due to the bars. The *disk3*s on the other hand show a much larger increase in the outer parts which probably reflects the significant number of particles that are in the envelope that formed during the merger. Therefore, particles at one cylindrical radius now populate a much wider range of velocities. Especially σ_z, sometimes also considered a measure of the heating in stellar disks,

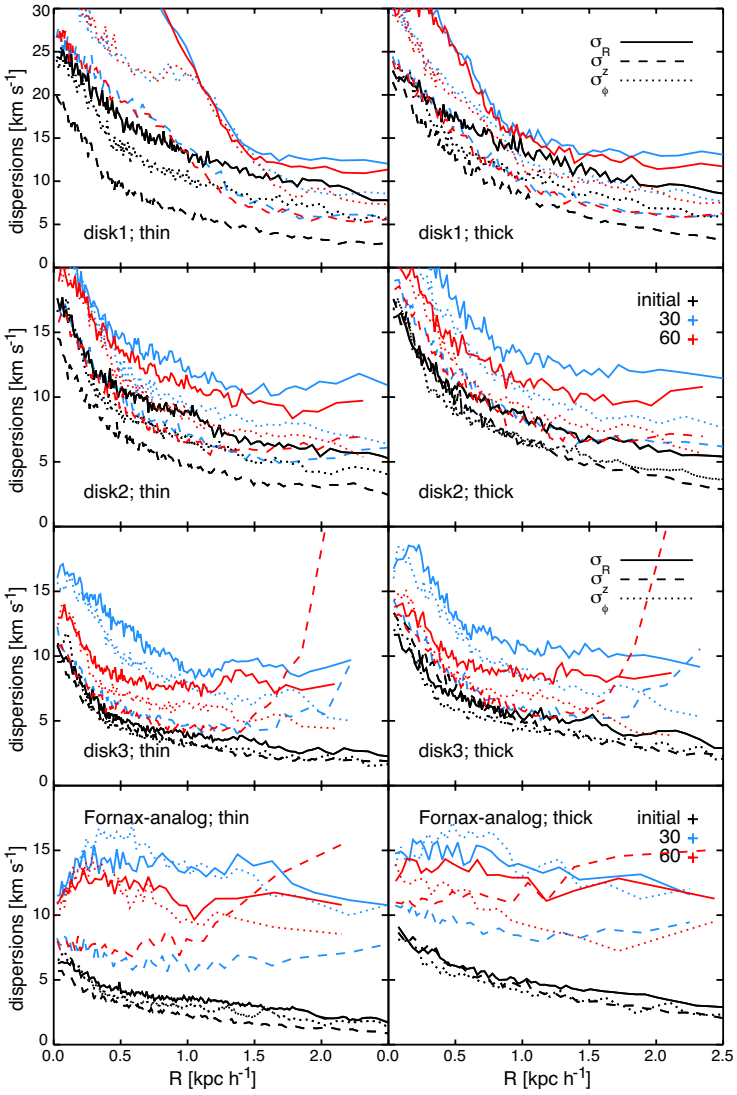

Figure 2.13 – Radial (solid lines), vertical (dashed lines), and azimuthal (dotted lines) velocity dispersions of all the disks before the merger (black) and 6 Gyr later for both orbits (30-degree inclination in blue, and 60-degree inclination in red). In all cases the disks are first aligned such that the total angular momentum vector of all particles within the half-mass radius of the disk is perpendicular to the plane in which the velocity dispersions are measured. All particles considered have $|z| < 0.05$ kpc h^{-1} and the bins have a variable bin size, but a fixed number of 400 particles each.

increases dramatically in the outskirts of the disk. Unfortunately, because of the low surface brightness in the outskirts it could be very difficult to measure this signature in dwarf galaxies observationally.

For the *Fornax-analog*s the velocity dispersions in the inner parts of the disk more than double and in some cases even triple with respect to the values before the merger. Furthermore, the velocity dispersions are more or less constant over the whole disk. Note that, as expected, for both the thin and thick *FNX-analog* the radial and azimuthal dispersions increase more for the 30-degree merger, but that the vertical dispersion increases more in the outer disk for the 60-degree merger.

The resulting kinematics can be compared to literature values of the dwarfs in the Local Group as most recently summarized in McConnachie (2012). The Fornax dwarf galaxy has an average line-of-sight velocity dispersion of 11.7 km s^{-1}. We can compare this to $\sigma_{\rm l.o.s.}$ for the four different *FNX-analog* systems presented in this chapter. We compute $\sigma_{\rm l.o.s.}$ averaged within 1.4 kpc, which is the half-mass radius of the *FNX-analog* remnants, and about 2 times the half-light radius of the Fornax dwarf galaxy, and find values in the range $\sim$ 10–14 km s^{-1}. These values are higher than similarly calculated line-of-sight velocity dispersions for the *disk3*s ($\sigma_{\rm l.o.s.} \sim$ 7–12 km s^{-1}), while the rotational velocity of *disk3* is more than twice that of *FNX-analog*. For the *Fornax-analog*s $v_\phi \sim \sigma_{\rm l.o.s.}$ around the half-mass radius and $v_\phi < \sigma_{\rm l.o.s.}$ for smaller R. Therefore, we can say that an initially disky dwarf galaxy similar to the *Fornax-analog* systems presented here can be transformed kinematically and morphologically by a minor merger with its own dark satellite to a more spheroidal system, akin to those observed.

2.4 Discussion

We have presented a series of simulations of minor mergers of dwarf galaxies and their own satellites. The satellites are presumed to be completely dark and we have shown here that for $M_{\rm sat}/M_{\rm host} = 0.2$ their effect on the morphology and kinematics of the dwarf galaxies can be severe. Moreover, for larger satellite-to-disk-mass ratios the impact of the merger is notably stronger. Therefore, it might be essential to take into account such events when considering the evolution of dwarf galaxies.

When setting up the simulations of the dwarf galaxies in the simulations presented in this chapter we were faced with a number of problems. We found that the standard methods used for setting up simulations of Milky Way-like galaxies could not be applied. The velocity structure especially needed to be revised. As a result of the dominance of the halo potential at all radii, new assumptions have to be made to solve for the velocity structure. In this chapter we decided to use the epicyclic approximation as long as it gives physical results, and we assume that the azimuthal velocity is continuous from

that point inwards. This solution is not ideal and results in an azimuthal velocity dispersion that has an unphysical bump. This bump disappears, however, when relaxing the disks, and the resulting rotation and dispersions are satisfactory. A possible improvement could be to fit a spline instead of a second order polynomial as we have done.

The concentration of the host halo plays a significant role in how much damage is induced by the satellite, as shown by comparing the *disk3* and *FNX-analog* experiments. A dwarf galaxy with a dark matter density profile that is shallower than seen in dark-matter-only simulations (as perhaps expected because of baryonic effects Mashchenko et al. 2008; Governato et al. 2010, 2012; Pontzen & Governato 2012; Teyssier et al. 2013) is therefore much more vulnerable to minor merger events by dark satellites.

It may be argued that some of the satellites in our simulations (e.g., in the case of *disk1*, *disk2,* and *disk3*) are on the verge of being too massive to be dark. However, the virial mass below which halos are expected to be devoid of stars does not have a sharp transition, but is expected to be around 10^8–10^9 $M_\odot$ (Gnedin 2000; Hoeft et al. 2006; Crain et al. 2007; Okamoto et al. 2008; Gnedin et al. 2009; Li et al. 2010; Sawala et al. 2013) (but see also Taylor & Webster 2005; Warren et al. 2007). If the satellite contained a small amount of baryons we might expect a similar result as in the case that the completely dark satellite would be more concentrated, because for the smallest halos the effects of baryons appear to be small (e.g., Governato et al. 2012). We have tested cases with different dark matter halo concentrations for the dark satellite, and in line with our expectations a more concentrated satellite survives longer and therefore has a stronger effect on (or causes more thickening of) the disk of the host dwarf galaxy.

On the other hand, although we vary the disk mass fraction to lower values (especially *disk3*) as is expected for dwarf galaxies, one could argue that our disks are still too massive for their halo mass. Following the stellar mass-halo mass relations from either abundance matching (e.g., Moster et al. 2013), or from hydrodynamical cosmological simulations (e.g., Sawala et al. 2015), our lowest stellar disk mass fraction should be a factor of 2–5 smaller. For such a disk the effect of the merger would increase significantly.

An important question is how often encounters such as those described in this chapter and Chapter 3 will take place. Although the subhalo mass function is almost self-similar and independent of host halo mass, higher satellite-to-disk-mass ratios lead to more disruptive events. So the expected fraction for significantly disruptive minor mergers for dwarf galaxies is not only given by the ($M_{\rm sat} : M_{\rm host} = 1 : 5$) fraction, but also by the fraction for minor encounters with $M_{\rm sat}/M_{\rm disk} > 1$. According to Deason et al. (2014) a significant fraction of the dwarf galaxies in the Local Group (10% for satellites and 15–20% for field dwarfs) have experienced major mergers with *stellar* mass ratios > 0.1. Including dark satellites and broadening the analysis to minor mergers

with small pericenters will increase the estimates of dwarf galaxies affected by mergers. Helmi et al. (2012) show that as the galaxy efficiency or disk mass fraction decreases substantially for lower mass halos this implies that such an encounter is much more common than previously expected. They estimate that dwarf galaxies similar to *disk3* or *FNX-analog* experience on average 1.5 encounters over a Hubble time where $M_{\rm sat}/M_{\rm disk} \simeq 1$ and only taking into account encounters where the pericenter lies within 30% of the virial radius of the host (dwarf galaxy) halo. A small first pericentric radius ensures a short timescale for the merger and also a large impact. We further quantify the expected significant merger fraction in Chapter 5.

Small galaxies in isolation are generally gas rich, an element we have not considered in our simulations. Previous work has shown that in mergers the presence of gas influences the response of the stellar component to the tidal forces (Moster et al. 2010; Naab et al. 2006), and the torques that arise during the merger can cause an accumulation of gas close to the center giving rise to an increase in star formation or even a starburst (Di Matteo et al. 2007; Teyssier et al. 2010). We plan to report on simulations of dwarf galaxies including gas in the disk and dark satellites in Chapter 3.

2.5 Conclusions

We have studied the response of disky dwarf galaxies to a $1:5$ minor merger with a dark satellite using a suite of N-body simulations. Our host halos have masses of $10^{10}\ M_\odot\ h^{-1}$ and $4\times10^{9}\ M_\odot\ h^{-1}$ and the baryon fractions that range from 0.008 to 0.04 are assumed to be in a stellar disk. The satellite is completely dark and has a prograde radial orbit with first pericenter within the half-mass radius of the disk and an inclination of either 30 or 60 degrees.

The structure and kinematics of the disks in our simulations are initialized following a careful adaptation of standard methods to this dwarf scale. We present a method to solve the velocity structure assuming that the potential is dominated by the halo at all radii and only using the epicyclic frequency up to the point where this approximation gives physical results. The resulting velocity profiles after relaxing the disk in isolation are smooth and stable.

In our experiments, the satellite loses mass very quickly while plunging into the denser central regions of the host and is completely disrupted after two to three pericenter passages. All dwarf galaxy disks are significantly disturbed by the minor merger. The most massive disks develop strong bars and thicken because of these bars, and stellar envelopes are formed around the disks. Smaller disks form more extended envelopes with a preferential orientations. This can be seen as tidal debris in what would be the inner stellar halo of the dwarf galaxy. However, in our simulations these tidal features are made of material from the disk instead of in the infalling satellite as is often assumed for observed shells, streams, and plumes.

Our suite of simulations shows that the disk mass fraction is an important parameter in minor mergers and that the disk thickens more when the ratio $M_{\rm sat}/M_{\rm disk}$ increases. For the lowest mass disks the final remnants' vertical structure can no longer be described by a sech^2 function. These systems are spheroidal and their radial profiles follow an exponential form. In these experiments, the azimuthal velocities are comparable in magnitude or even lower than the line-of-sight velocity dispersions. The remnant system has properties similar to the Fornax dwarf spheroidal, indicating that mergers between dwarfs and dark satellites may be an additional channel for the formation of small spheroidal systems.

Acknowledgements. We are grateful to Laura Sales for many useful discussions and to Carlos Vera-Ciro, Alvaro Villalobos and Volker Springel for providing code. AH acknowledges financial support from the European Research Council under ERC-StG grant GALACTICA-240271.

3

Gas and star formation in minor mergers of dwarf galaxies with dark satellites

— Based on *Dark influences II: Gas and star formation in minor mergers of dwarf galaxies with dark satellites*, T. K. Starkenburg, A. Helmi & L. V. Sales, 2016, Astronomy & Astrophysics, 587, 24 —

Abstract

It has been proposed that mergers induce starbursts and lead to important morphological changes in galaxies. Most studies so far have focused on large galaxies, but dwarfs might also experience such events, since the halo mass function is scale-free in the concordance cosmological model. Notably, because of their low mass, most of their interactions will be with dark satellites. In this chapter we follow the evolution of gas-rich disky dwarf galaxies as they experience a minor merger with a dark satellite. We aim to characterize the effects of such an interaction on the dwarfs' star formation, morphology, and kinematical properties. We performed a suite of carefully set-up hydrodynamical simulations of dwarf galaxies that include dark matter, gas, and stars merging with a satellite consisting solely of dark matter. For the host system we vary the gas fraction, disk size and thickness, halo mass, and concentration, while we explore different masses, concentrations, and orbits for the satellite. We find that the interactions cause strong starbursts of both short and long duration in the dwarfs. Their star formation rates increase by factors of a few to 10 or more. They are strongest for systems with extended gas disks and high gas fractions merging with a high-concentration satellite on a planar, radial orbit. In contrast to analogous simulations of Milky Way-mass galaxies, many of the systems experience strong morphological changes and become spheroidal even in the presence of significant amounts of gas. The simulated systems compare remarkably well with the observational properties of a large selection of irregular dwarf galaxies and blue compact dwarfs. This implies that mergers with dark satellites might well be happening but not be fully evident, and may thus play a role in the diversity of the dwarf galaxy population.

3.1 Introduction

In the Lambda Cold Dark Matter (ΛCDM) paradigm, small dark matter halos are abundant. Most of these halos, with $M_{\rm vir} < 10^9 M_\odot$, are predicted to be strongly affected by reionization, photo-evaporation, and/or supernova feedback (Gnedin 2000; Hoeft et al. 2006; Kaufmann et al. 2007; Okamoto et al. 2008; Gnedin et al. 2009; Li et al. 2010; Sawala et al. 2013; but see also Taylor & Webster 2005; Warren et al. 2007). These processes thus cause progressively larger numbers of small dark matter halos to be almost completely dark. The existence of such dark galaxies is a solution that is often suggested to the missing satellites problem (Klypin et al. 1999; Moore et al. 1999).

Dwarf galaxies are known to be very inefficient at forming stars (Blanton et al. 2001; Robertson & Kravtsov 2008), to have very low baryon fractions (Gnedin 2000; Hoeft et al. 2006; Crain et al. 2007), and to generally be gas-rich if in the field. This is consistent with the expectation that the stellar-to-halo-mass ratio must decrease steeply toward lower masses (Behroozi et al. 2013a; Moster et al. 2013; Kormendy & Freeman 2016; Garrison-Kimmel et al. 2014; Sawala et al. 2015). On the other hand, the halo mass function is predicted to be almost completely scale-free (van den Bosch et al. 2005; van den Bosch & Jiang 2014), i.e., similar for field dwarf and large disk galaxies. However, the subhalos of dwarf galaxies must have much lower baryonic component masses, and so most of their satellites will be dark (Helmi et al. 2012).

Mergers of gas-rich galaxies are often thought to give rise to bursts of star formation (Mihos & Hernquist 1994a,b; Teyssier et al. 2010; Bournaud et al. 2011), although simulations suggest this depends on the merger mass ratio (e.g., Di Matteo et al. 2007). From the observational perspective, (see e.g., Ellison et al. 2011; Willett et al. 2015), even minor mergers have been shown to significantly contribute to local star formation (Kaviraj 2014a,b). In the case of dwarf galaxies it has been suggested that interactions are responsible for the class of blue compact dwarfs (BCDs) (Paudel et al. 2015): dwarf galaxies with a significant, centrally concentrated young stellar population (e.g., Gil de Paz et al. 2003). In general many dwarf systems with increased star formation rates have been found to be irregular or to show signs of disturbances (Taylor et al. 1995; Ekta & Chengalur 2010; López-Sánchez 2010; Holwerda et al. 2013; Lelli et al. 2014b; Knapen & Cisternas 2015), but in a number of cases no visible companion has been found (Brosch et al. 2004; Ekta & Chengalur 2010; López-Sánchez 2010; Lelli et al. 2014b). Other possible origins of the increase in star formation and the irregular morphology are cosmological gas inflows (see for example Verbeke et al. 2014) or re-accretion of material blown out by previous starbursts, and varying internal instabilities (e.g., Meurer et al. 1998; van Zee et al. 2001; Lelli et al. 2014a; Elmegreen et al. 2012; Bekki & Freeman 2002).

In view of the above discussion, it appears plausible that some of these starbursts could be induced by interactions with dark satellites. Following

Chapter 2 here we focus on the effect of a merger on a gas rich dwarf galaxy. In Chapter 2 we ran a suite of collissionless simulations of dwarf galaxies and their dark satellites, and showed that these could severely alter the morphology and kinematics of the dwarf. In this chapter we extend these simulations to dwarf galaxies with varying gas fractions and study the effects of the merger on the star formation rates, gas and stellar morphology and kinematics. The initial conditions of the dwarf galaxies and their satellites and the parameters for the simulations are described in Sect. 3.2. We report our results and their dependence on properties of the systems and the interactions in Sect. 3.3. We compare these SPH-results with the collissionless simulations from Chapter 2 in Sect. 3.4 and to observational results in Sect. 3.5. We conclude by discussing our results in Sects. 3.6 and give a summary of our main findings in Sect. 3.7.

3.2 Models

We perform a suite of controlled simulations of isolated dwarf galaxies and mergers with their (dark) satellites. The simulations are run using the OWLS version (last described in Schaye et al. 2010) of the N-body/SPH-code Gadget-3 (based on Springel et al. 2001b; Springel 2005) with implementations for star formation and feedback as described in Schaye & Dalla Vecchia (2008); Dalla Vecchia & Schaye (2008).

3.2.1 Initial conditions

The setup of the initial conditions is based on Springel et al. (2005); Schaye & Dalla Vecchia (2008); Dalla Vecchia & Schaye (2008) and a more complete description can be found in Chapter 2. Here we briefly describe the initial structure of the dwarf galaxy and of the satellite. The values of the structural and orbital parameters for all the simulations are listed in Tables 3.1 and 3.2.

Main (disky dwarf) galaxies

The host dwarf galaxies have several components including a dark halo, a stellar disk and a gaseous disk. The dark matter halo follows a Hernquist profile (Hernquist 1990),

$$\rho(r) = \frac{\rho_0}{(r/a)(1+r/a)^3}, \tag{3.1}$$

where the parameters ρ_0 and a are set by an equivalent NFW (Navarro et al. 1996) profile, such that the total mass of the Hernquist halo equals the virial mass of the NFW halo and their profiles have similar inner densities ($r_s\rho_{0,\mathrm{NFW}} = a\rho_{0,\mathrm{H}}$) (Springel et al. 2005).

We consider three different concentrations $c_{\rm host} = r_{\rm vir}/r_{s_{\rm NFW}}$ for the halos: $c_{\rm host} = 5$, $c_{\rm host} = 9$, and $c_{\rm host} = 15$. The latter two are consistent with the mass – concentration relation found in large cosmological simulations (Macciò et al. 2008; Muñoz-Cuartas et al. 2011) for the mass-scale considered here. The lowest $c_{\rm host}$ corresponds to the best-fit NFW model for the Fornax dwarf spheroidal galaxy from Breddels & Helmi (2013). The velocities of the halo particles are set using the distribution function of a Hernquist halo. Since the contribution of the disk is hereby initially neglected, the halo shows a slight adiabatic contraction at the start of the simulations, which stabilizes within approximately 0.5 Gyr.

The stellar masses of the systems follow generally (extrapolated) stellar mass – halo mass relations available in the literature (Behroozi et al. 2013a; Moster et al. 2013; Garrison-Kimmel et al. 2014; Sawala et al. 2015). The gas fraction, $f_{\rm gas} = M_{\rm gas}/(M_\star + M_{\rm gas})$, ranges from $f_{\rm gas} = 0.3$ to $f_{\rm gas} = 0.9$ in agreement with observational estimates (Huang et al. 2012; McQuinn et al. 2015). This means that the baryonic mass can be quite high, and that in the most gas-rich systems $M_{\rm gas} = 9M_\star$.

Table 3.1 – Structural parameters for the host dwarf galaxies.

Model	$M_{\rm vir}$	$r_{\rm vir}$	c	$M_\star$	R_d	$\frac{z_0}{R_d}$	$f_{\rm gas}$
	$10^{10}M_\odot$	kpc		$10^8 M_\odot$	kpc		
A	5.6	77	9	1.4	0.93	0.1	0.5
B	2.2	56	15	0.27	0.78	0.2	0.75
C1	1.4	48	15	0.11	0.78	0.3	0.9
C2	...	...	...	...	0.39	...	...
C3	...	...	5	...	0.78	...	...
C4	1.4[a]	...	15	0.55	...	0.2	0.5
C5	...[a]	...	...	0.77	...	...	0.3
D1	0.97	42	5	0.044	0.95	0.3	0.9
D2	...	...	15	...	...	...	...
D3	...	...	5	...	...	0.5	...
D4	...	...	5	...	0.48	0.3	...
D5	...	...	5	...	...	0.5	...
E1	0.55[b]	27	5	0.22	0.95	...	0.5
E2	...[b]	...	...	0.31	...	...	0.3

Notes ... denotes that the value is equal to that reported in the row above.
[(a)] These systems are equivalent to the *disk3*-systems from Ch. 2 but include gas.
[(b)] These systems are equivalent to the *FNX-analog*-systems from Ch. 2 but include gas.

Table 3.2 – Parameters for the satellites and their orbits

$M_{\rm sat}/M_{\rm vir_{main}}$	$c_{\rm sat}$	$\frac{v_r}{v_{\rm vir_{main}}}$	$\frac{v_t}{v_{\rm vir_{main}}}$	$r_{\rm apo}/r_{\rm peri}{}^a$	inclination
0.2	15	-0.08	0.06	~ 40	30
...	...	...	...	~ 40	60
...	...	0	...	~ 40	0
...	25	-0.08	...	~ 40	30
...	...	0	...	~ 35	0
...	...	...	0.86	2	...
...	...	...	0.5	6	...
0.1	16	0	0.06	~ 45	0
...	25	...	...	~ 45	...
0.05	17	...	...	~ 40	...
...	25	...	...	~ 35	...

Notes ... denotes that the value is equal to that reported in the row above.
[a] The apo-to-peri ratio is defined for the first pericentric passage. For very radial orbits, this ratio is uncertain (by $\sim$ 20%) because of the dependency on the time-sampling around this passage.

Both the stellar and gaseous disk follow an exponential surface density profile with radius. The scale lengths of the stellar disks are close to the values expected from Mo et al. (1998); Springel & White (1999) for the $M_{\rm vir} = 1.4 \times 10^{10} M_\odot$ and $c_{\rm host} = 15$ systems, and also for the lowest mass dwarf ($M_{\rm vir} = 0.55 \times 10^{10} M_\odot$) with $c_{\rm host} = 5$ dark matter halo, assuming that the disk angular momentum fration equals the disk mass fraction ($j_d = m_d$). For completeness we explore for two systems ($M_{\rm vir} = 0.97 \times 10^{10} M_\odot$ and $M_{\rm vir} = 1.4 \times 10^{10} M_\odot$) smaller disk scale lengths. For all disks the exponential radial profiles and the scale lengths are stable during evolution in isolation. The stellar disk is further described by an isothermal vertical distribution with a constant scale height such that $0.1 R_d < z_0 < 0.5 R_d$:

$$\rho_{d,\star}(R,z) = \frac{M_{d,\star}}{4\pi R_d^2 z_0} \exp\left(-\frac{R}{R_d}\right) \operatorname{sech}^2\left(\frac{z}{z_0}\right). \tag{3.2}$$

We consider thicker disks for the lowest mass simulated galaxies. This is in concordance with observations (Yoachim & Dalcanton 2006; Sánchez-Janssen et al. 2010) and also expected since gas cooling is less efficient in smaller halos (Kaufmann et al. 2007; Robertson & Kravtsov 2008).

We explore two different scale lengths of the gaseous disk in comparison to the stellar disk, namely $R_g = R_d$, and $R_g = 2R_d$. The vertical distribution of

the gas is determined by requiring hydrostatic equilibrium,

$$-\frac{1}{\rho_g}\frac{\partial P}{\partial z}-\frac{\partial \Phi}{\partial z}=0. \tag{3.3}$$

Using an effective equation of state (EOS), with $\gamma_{\mathrm{EOS,eff}} = (d \ln P) / (d \ln \rho)$, this can be written as

$$\frac{\partial \rho_g}{\partial z}=-\frac{\rho_g^2}{\gamma_{\mathrm{EOS,eff}} P}\frac{\partial \Phi}{\partial z}. \tag{3.4}$$

In our simulations we use the effective equation of state of the multiphase ISM model by Schaye & Dalla Vecchia (2008); Dalla Vecchia & Schaye (2008). The gas is governed by the effective equation of state when the density of the gas is above the threshold for star formation as set by the subgrid physics discussed in Sect. 3.2.3, while at lower densities the gas is assumed to follow an isothermal equation of state.

The vertical distribution of the gas can be iteratively determined as a function of radius using a fine logarithmic grid in the R–z plane (Springel et al. 2005), where the surface density of the gas, $\Sigma_{d,\mathrm{gas}}(R)$, is set by the exponential radial profile and the chosen scale length,

$$\Sigma_{d,\mathrm{gas}}(R)=\frac{M_{d,\mathrm{gas}}}{2\pi R_g^2}\exp\left(-\frac{R}{R_g}\right)=\int \rho_g(R,z)\,\mathrm{d}z. \tag{3.5}$$

To calculate the potential in Eq. (3.4) we follow Springel et al. (2005) in using a tree code and a discretized mass distribution to represent the disk components, adding contribution of the dark matter halo analytically, and use a grid of $4096 \times 64 \times 128$ in the radial, vertical and azimuthal directions.

In Chapter 2 we adapted the way in which the velocity structure of the stellar disks is set up. Contrary to large galaxies, for lower mass systems the epicyclic approximation breaks down in a large part of the disk which, if used, can cause a non-physical streaming velocity. Therefore we set up the velocity structure only assuming the epicyclic approximation in the part of the disk where it is still valid and fit a smooth quadratical curve to the rotation curve closer in. Moreover, the potential of the model dwarf galaxies is dominated by their dark matter halo at all radii, so we assume that the velocity ellipsoid is aligned with the spherical coordinate system instead of the cylindrical coordinate system of the disks. For the gas, the initial azimuthal streaming velocity is determined through the gravitional, pressure, and centrifugal forces:

$$v_{\phi,\mathrm{gas}}^2=R\left(\frac{\partial \Phi}{\partial R}+\frac{1}{\rho_g}\frac{\partial P}{\partial R}\right). \tag{3.6}$$

Table 3.3 – Numerical parameters

Model	$\frac{M_{\rm sat}}{M_{\rm vir_{main}}}$	$N_{\rm DM}$ $\times 10^6$	$N_{\rm gas}$ $\times 10^5$	$N_\star$ $\times 10^5$	$m_{\rm DM}$ $10^4 M_\odot$	$m_{\rm bar}$ $10^2 M_\odot$
A	0.2	1	1	1	5.60	13.8
...	0.1	...	...	...	...	...
...	0.05	...	...	...	...	...
B	0.2	...	1.5	0.5	2.12	5.34
C1 − C3	...	...	1.8	0.2	1.45	5.55
D	...	...	...	...	0.97	2.21
C4	...	5	1	1	0.27	5.51
C5	...	...	...	...	...	7.71[a]
E1	...	...	...	...	0.17	3.35
E2	...	...	...	...	...	4.69[b]

Notes ... denotes that the value is equal to that reported in the row above.
[(a)] For the system C5 the value reported corresponds to $m_\star$ while $m_{\rm gas} = 3.31 \times 10^2\ M_\odot$.
[(b)] For the system E2 the value reported corresponds to $m_\star$ while $m_{\rm gas} = 2.01 \times 10^2\ M_\odot$.

Satellites

The satellite consists solely of a dark matter halo with a mass of 20% of the dwarf galaxy's halo mass in most of our simulations. Its concentration is determined by following the mass – concentration relation from Muñoz-Cuartas et al. (2011). In Sect. 3.3.2 we explore the effect of a two or four times smaller mass and a higher concentration for the satellite.

Most of the satellite orbits we consider are close to completely radial with initially none or a small (prograde) tangential velocity, although we also explore more circular orbits (see Table 3.2 and Sect. 3.3.2). At the start of the simulations the satellite is placed at a distance of $0.67 r_{\rm vir}$ from the center of the host with a radial velocity that is small with respect to the local circular velocity (so the satellite is initially close to apocenter). The orbit is either in the plane of the host disk or has an inclination of 30 (or in one case 60) degrees, similar to other studies of disk thickening (Villalobos & Helmi 2008; Moster et al. 2010).

3.2.2 Numerical parameters

We consider two different numerical setups for the host dwarf galaxies. For the *disk3-gas* (models C4 and C5) and *FNX-gas* (models E1 and E2) systems that we compare to the collissionless simulations of Chapter 2, we use 5×10^6

particles to represent the dwarfs' dark matter halo and 10^5 particles for the gaseous and for the stellar disk irrespective of the value of $f_{\rm gas}$. For all other hosts the 2×10^5 baryonic particles are divided among gas and stars according to $f_{\rm gas}$ so that all gas and star particles have initially equal mass, and the dark halo is represented by 10^6 particles.

The satellite is in all cases represented by 5×10^5 particles which gives a dark matter particle mass for the satellite of $2 \times 10^3\ M_\odot \lesssim m_{\rm sat} \lesssim 2 \times 10^4\ M_\odot$. The softening lengths used are 0.025 kpc and 0.016 kpc for the host halo and satellite respectively, and 0.008 kpc for both the gas and stars. These values are chosen following Villalobos & Helmi (2008) and Athanassoula et al. (2000) and produce stable systems. All numerical parameters are summarized in Table 3.3.

3.2.3 Star formation and feedback prescription

We use the star formation and stellar feedback prescription from Schaye & Dalla Vecchia (2008) and Dalla Vecchia & Schaye (2008). The star formation prescription is based on empirical laws and has very good numerical properties. Schaye & Dalla Vecchia (2008) have shown how the gas surface densities in the Kennicutt-Schmidt law (Kennicutt 1998) can be related to pressure by assuming that the scale height of the gas disk is of order of the local Jeans scale and that the gas is in local hydrostatic equilibrium and self-gravitating. This is combined with a polytropic effective equation of state for the multiphase interstellar medium with a slope of $\gamma_{\rm EOF} = 4/3$, which always ensures a constant Jeans mass (so independent of the local gas density). We follow Schaye (2004) in using a density threshold $n_H = 0.1\ {\rm cm}^{-3}$ which corresponds to a surface density threshold of $\sim 10\ M_\odot\ {\rm pc}^{-2}$ and a temperature threshold of 10^4 K (Schaye & Dalla Vecchia 2008). We do include radiative cooling but no metals and therefore no metal-line cooling or chemical enrichment.

The feedback model is described in Dalla Vecchia & Schaye (2008) and consists of kinetic supernova winds. The model is governed by the wind speed v_w, and mass loading $\eta = \dot{M}_w/\dot{M}_\star$, which are related to the fraction of the kinetic energy injected by supernovae (SNe) per solar mass, $\epsilon_{\rm SN}$, also called the feedback efficiency as

$$f_w = \frac{\eta v_w^2}{2\epsilon_{\rm SN}}. \tag{3.7}$$

Following Dalla Vecchia & Schaye (2008) we set $\epsilon_{\rm SN} = 1.8 \times 10^{49}\ {\rm erg}\ M_\odot^{-1}$ which is appropriate for a Chabrier (2003) initial mass function, a stellar mass range 0.1 – $100\ M_\odot$ and all stars above $6\ M_\odot$ ending as core-collapse SNe. The wind particles remain as such for $t_w = 1.5 \times 10^7$ yr and during that time are not able to be kicked again by another SN or participate in star formation, but they are not decoupled hydrodynamically.

Both observational data (Schwartz & Martin 2004; Martin 2005) and theoretical models (Okamoto et al. 2010; Lagos et al. 2013) suggest that wind

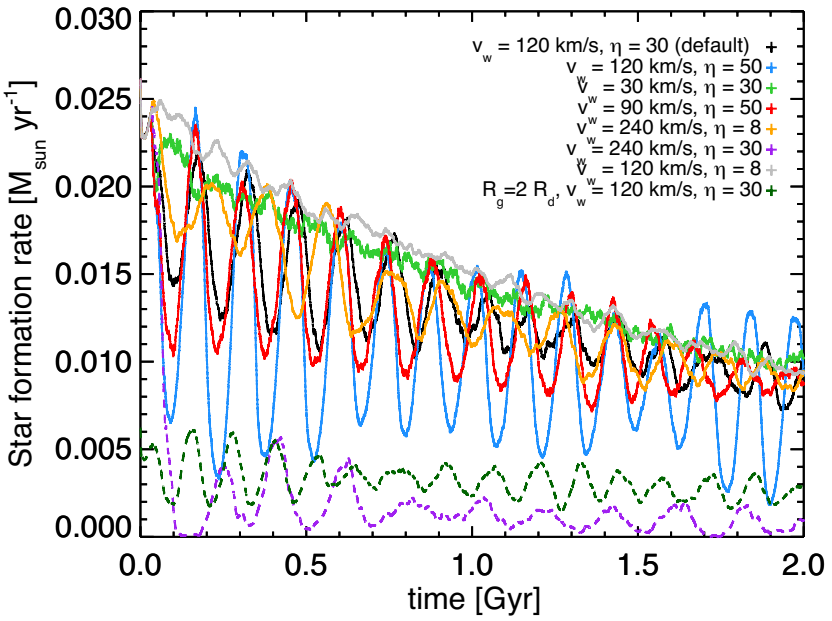

Figure 3.1 – Star formation rates for model C1 ($M_{\rm vir} = 1.4 \times 10^{10} M_\odot$) with different values of the feedback parameters: wind velocity and mass loading depicted in different colors as indicated by the inset for $R_g = R_d$, except for dark green where $R_g = 2R_d$.

velocities are lower and the mass loading rates are higher for low mass galaxies and low star formation rates. Therefore, rather than making a single choice for the numerical parameters, we experimented with a selection of different parameters values as described in the next section.

3.2.4 Evolution in isolation

Exploration of subgrid parameters

To identify a reasonable default model for the dwarf galaxies we explored a small set of combinations of the large parameter space and varied two of the stellar feedback parameters, namely the wind speed v_w (30, 90, 120, 240, and 600 km/s) and the mass loading η (2, 8, 10, 20, 30, 40, 50).

Our goal is for a galaxy in isolation to have a fairly continuous star formation rate on a timescale comparable to that of the merger. This is important to be able to pin down to the effect of the merger. However since we do not model fresh gaseous infall all star formation rates will decline due to gas depletion. We also pay attention to ensure that the gas is not all converted into stars or blown away by stellar feedback too quickly. Nonetheless, a tight

correlation exists between the initial gas mass and its distribution and the early star formation rate. Via the threshold for star formation, this also depends on the gravitational potential (and hence on the mass and concentration of the dark matter halo and the mass, scale length, and scale height of the stellar disk).

The star formation rate over a period of 2 Gyr for the dwarf galaxy model C1 ($M_{\rm vir} = 1.4 \times 10^{10} M_\odot$, $f_{\rm gas} = 0.9$, $R_g = R_d$, and $z_0 = 0.3 R_d$), for varying feedback parameters is shown in Fig. 3.1. The star formation rates for all prescriptions are within a factor of a few of each other and in all cases star formation is sustained over a long timescale. For the more extended gas disk ($R_g = 2R_d$, dashed dark green) the star formation rates are about a quarter of the $R_g = R_d$-case (black). For the most efficient feedback ($v_w = 240 {\rm km/s}$ and $\eta = 30$ so $E_{\rm wind}/E_{\rm SN} = 96\%$, dashed purple) the gas disk is blown apart right after the onset of star formation and subsequent star formation occurs at a similar rate as for the more extended gas disk. The periodicity seen in the first ~ 1 Gyr is driven by the fact that star formation starts in the whole disk at the same time. This is enhanced if the disk is not perfectly centered in the potential but is reduced at later times and for lower star formation rates. The amplitude of the oscillations in star formation also depends on the star formation and feedback parameters. For example the amplitude of the periodicity is larger for higher mass loading of the wind (compare for example the gray, black, and blue star formation rates in Fig. 3.1). Reassuringly, the evolution is very similar for settings with comparable feedback efficiencies (see for example the red, yellow, and black curves in Fig. 3.1 all with $E_{\rm wind}/E_{\rm SN} \approx 24\%$).

We tested the influence of decoupling the wind particles from star formation by comparing with a run without decoupling, and found that this does not change the star formation rate and evolution of the gas disk.

We further explored the effects of using higher values for the density threshold n_H (1 and 10 cm^{-3}), as proposed in the recent literature (e.g., Governato et al. 2010), but found that this restricts star formation to the very center of the galaxy and does not enhance the fragmentation of the disk gas as we do not include metal-line cooling, and therefore does not lead to a more realistic system.

As default model we take the star formation and feedback parameters corresponding to the black curve in Fig. 3.1 for $R_g = R_d$ (dark green for $R_g = 2R_d$). The default wind velocity is $v_w = 120$ km/s with a mass loading of $\eta = 30$, resulting in $f_w = 24\%$.

The default model

Figure 3.2 shows snapshots of the gas distribution and state for one of the most massive dwarf galaxies, model A ($M_{\rm vir} = 5.6 \times 10^{10} M_\odot$ and $M_\star = 1.4 \times 10^8 M_\odot$), evolved in isolation. For all plots in this chapter the plane of the disk is defined

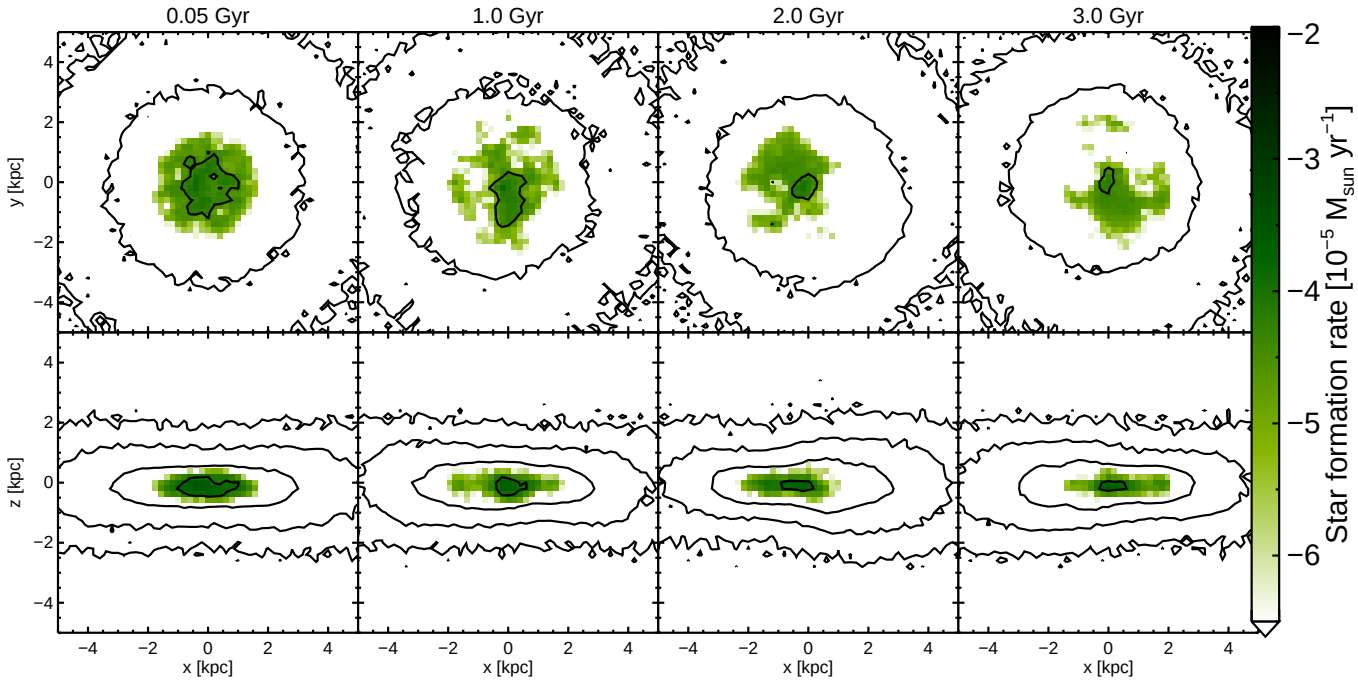

Figure 3.2 – Face-on (top) and edge-on (bottom) density contours of the gas in the disk of model A with $R_g = 2R_d$, evolved in isolation. The contour levels are at 0.25, 1, 4, and 16×10^{20} N cm^{-2}. The local star formation regions (and their amplitude) are shown in green at different moments during the simulation.

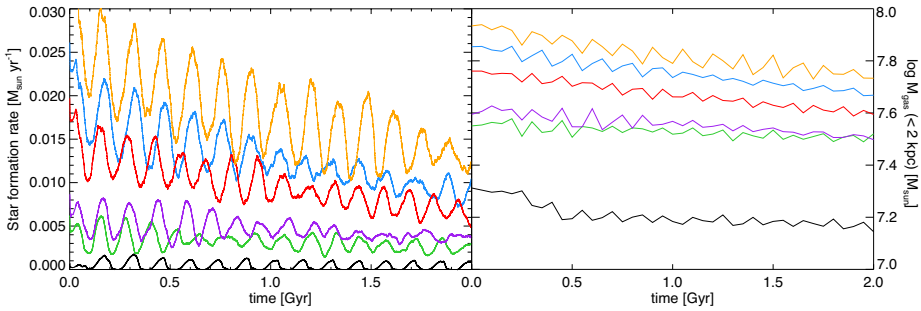

Figure 3.3 – Star formation rates (left panel) and central gas masses (right panel) for all systems in isolation with $R_g = R_d$ for models A (orange), B (red), C1 (blue), D1 (black), and with $R_g = 2R_d$ for models A (purple) and C1 (green). Note that although model C1 (blue) is less massive than B (red), the star formation rate is higher for C1 because it has a higher gas mass in the center due to its higher initial gas fraction.

as the plane perpendicular to the angular momentum vector of the inner 50% of the initial stellar disk particles. As mentioned above the stellar feedback parameters are set such that the star formation rate and the disk of the dwarf galaxy are reasonably stable for several Gyr. Since the gas in the outskirts of the disk is not dense enough, most of the star formation takes place within the central $\sim 2\,\mathrm{kpc}$ ($\sim R_g = 2R_d$ for this model). Due to the stellar feedback which blows gas away that eventually falls back again, the star formation is patchy and locally bursty.

The star formation rates (SFR) for a subset of the dwarf galaxies run in isolation using our default star formation and feedback parameters are plotted in the left panel of Fig. 3.3. The average amplitude of the star formation rate clearly depends on the total mass of the galaxy, the amount of gas in the disk and its initial extent. Indeed, for a more extended disk set up in equilibrium, a smaller fraction of gas will be above the density threshold for star formation.

The amount of gas in the central part of the disk is shown in the right panel of Fig. 3.3. That both the gas fraction and the mass of the dwarf galaxy are important is made explicit by comparing model B ($M_{\rm vir} = 2.2 \times 10^{10} M_\odot$, $M_\star = 2.7 \times 10^7 M_\odot$ and $f_{\rm gas} = 0.75$, red) and model C1 ($M_{\rm vir} = 1.4 \times 10^{10} M_\odot$, $M_\star = 1.1 \times 10^7 M_\odot$, $f_{\rm gas} = 0.9$, blue).

The panel on the right in Fig. 3.3 shows that although the more massive dwarf galaxy model B has 2.5 times more mass in dark matter and stars initially, the lower mass system model C1 actually has a slighty higher gas mass ($M_{\rm gas} = 9.9 \times 10^7 M_\odot$ versus $M_{\rm gas} = 8.2 \times 10^7 M_\odot$, due to the higher gas fraction) and a higher star formation rate. After 2 Gyr the stellar masses of the two systems are similar and also the gas fractions are more comparable than initially.

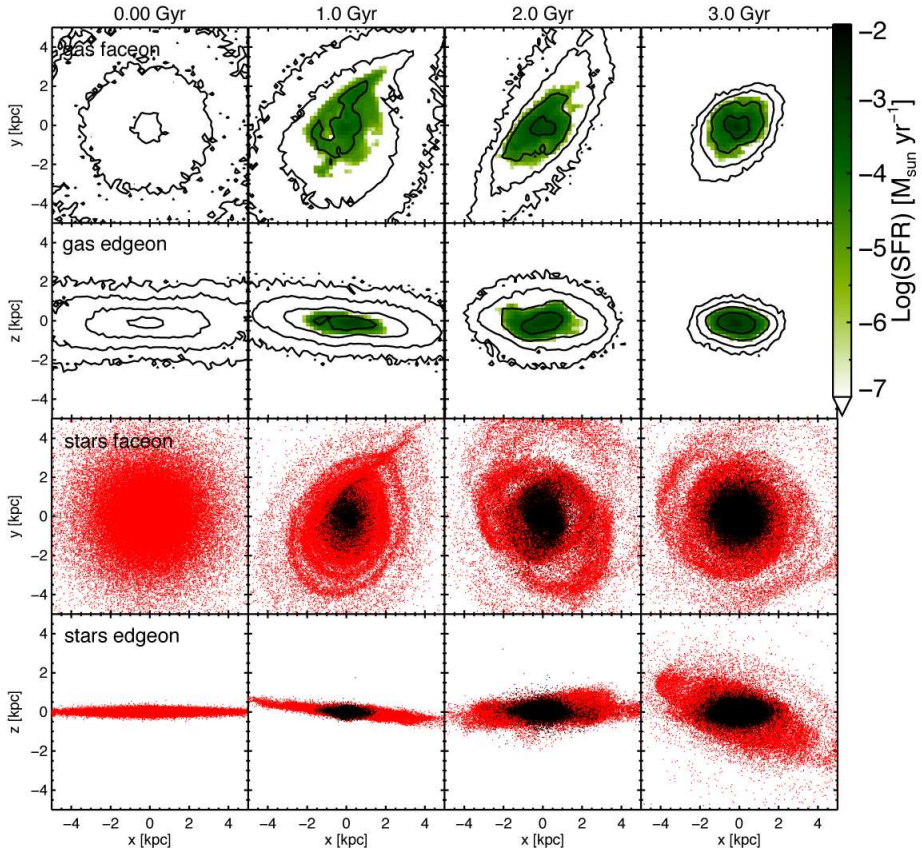

Figure 3.4 – Evolution of model A ($M_\star = 1.4 \times 10^8 M_\odot$) with $R_g = 2R_d$ merging with a 20% mass satellite on a co-planar, very radial orbit. The top rows show the face-on and edge-on, respectively, view of the gas in the disk (contours at 0.25, 1, 4, and 16×10^{20} N cm^{-2}) with the gas that is currently forming stars highlighted in green (see colorbar for relative values). The bottom panels show the old stellar component in red, and newly formed star particles in black, at different times during the merger.

Although the simulated systems have slowly declining star formation rates in general (as a result of the lack of external gas infall), they agree quite well with observations, also in terms of gas content (Hunter & Elmegreen 2006; Weisz et al. 2012; Ott et al. 2012; Warren et al. 2012; Huang et al. 2012; McQuinn et al. 2015). However, the lower mass disks tend to be more extended, slightly thinner, and have lower surface brightness compared to observations. We make a more detailed comparison with observations of the isolated and merger remnant dwarf galaxies in Sect. 3.5.

3.3 Starbursting dwarfs as the result of a merger

In this Section we compare first the behaviour of one of the highest (model A) and one of the lowest (model D1) mass dwarfs, as they interact with a dark satellite. We describe the general properties and then address in more detail how the interacting systems vary depending on the properties of the satellite, its orbit, and the host. In all cases explored the evolution is quite different from the dwarfs in isolation, as the majority of the systems experience starbursts of varying strength.

3.3.1 Two examples

Figure 3.4 shows a series of snapshots of the evolution of the system of Fig. 3.2, model A ($M_\star = 1.4 \times 10^8 M_\odot$) with $R_g = 2R_d$, now merging with a satellite on a co-planar very radial orbit. The stellar disk thickens, tilts, and develops tidal arms and rings. The gaseous disk depicts minor tidal arms and becomes quite asymmetric. Most importantly gas is driven into the center of the dwarf galaxy due to tidal torques, which leads to a strong increase of the star formation rate as we discuss below.

Fig. 3.5 shows the evolution for the lower mass model D1 ($M_\star = 4.4 \times 10^6 M_\odot$) merging with the satellite on a very radial 30 degrees inclined orbit. Similar to what was found in Chapter 2, for this smaller mass object the effect of the satellite on the stellar disk is much stronger. The stellar morphology of the remnant is spheroidal, for both the old and the newly formed stellar populations (see the rightmost panels of Fig. 3.5). The gas disk is severely disturbed, although no strong tidal tails form. As can be seen in the third panel of the top two rows, the presence of the satellite can cause off-center starbursts.

Fig. 3.6 shows clearly the effect of the merger on the SFR for these two systems. Both for model A (blue) and D1 (black) the star formation rates are increased by factors ~ 3 up to 12. This happens not only during the merger process itself with sharp strong peaks around pericenter passages, but more strikingly for a rather extended period. The relative amplitude of the increase in the SFR is similar for both systems, while in an absolute sense, the more massive object has a higher SFR, reaching values of $0.04 M_\odot$ yr^{-1}. Note as well

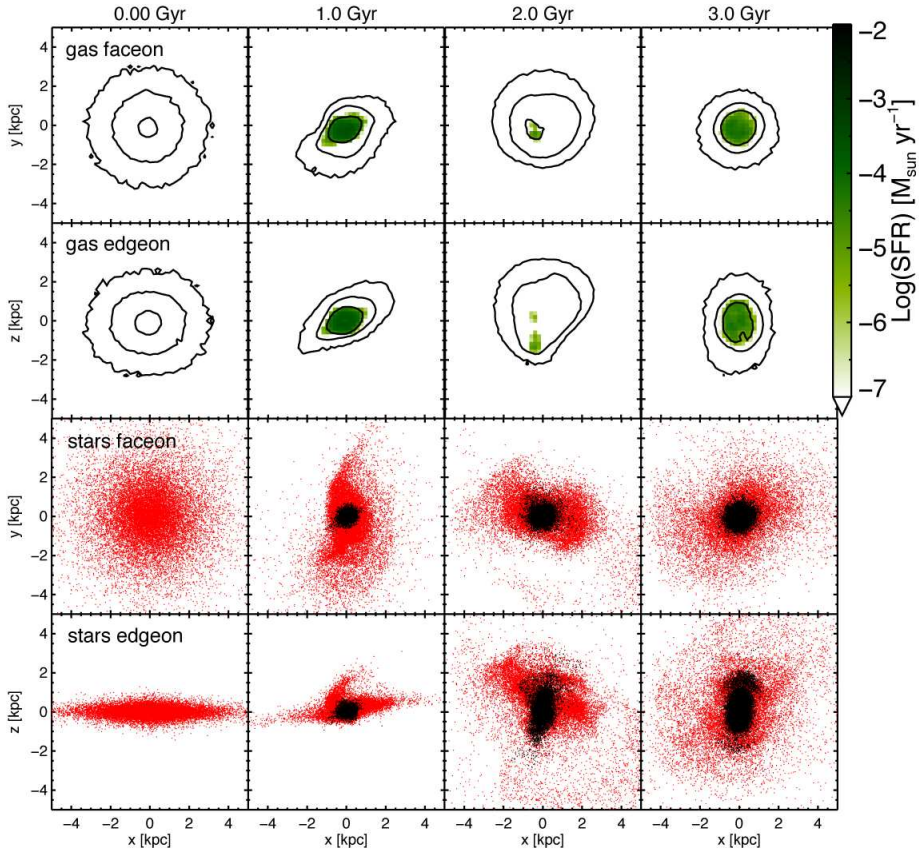

Figure 3.5 – Same as Fig. 3.4 for model D1 ($M_\star = 4.4 \times 10^6 M_\odot$ with $R_g = R_d$), merging with a 20% mass satellite on a 30-degrees inclined, very radial orbit.

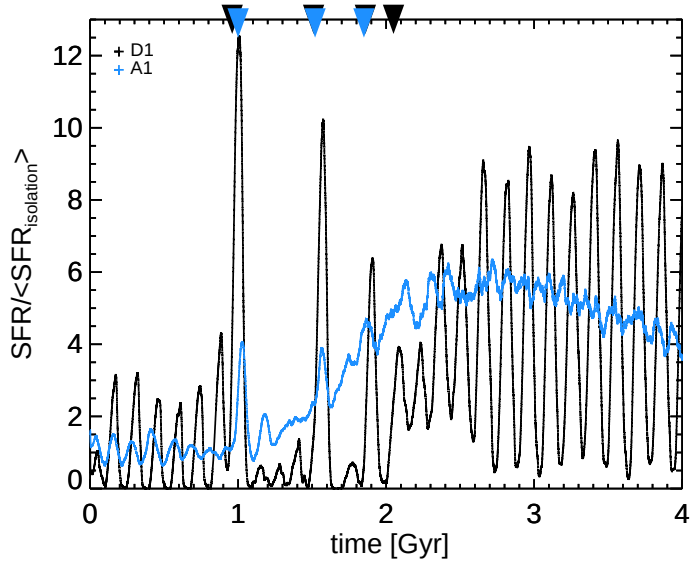

Figure 3.6 – Star formation rates with respect to the average of the SFR in isolation for the first Gyr, for the systems A1 (see Fig. 3.4) and D1 (see Fig. 3.5) experiencing a 20% mass ratio merger.A number of pericentric passages of the satellite during the different simulations are indicated by the arrows at the top of the figure.

from Figs. 3.4 and 3.5 that in both cases the gas disk at the end of the simulation is much more compact than initially.

In Figures 3.7 and 3.8 we plot the evolution in the rotational velocity for the two systems shown in Figs. 3.4 and 3.5, respectively. The rotational motion of the gas disk of model A seems to increase first (see the left middle panel of Fig. 3.7) and then strongly decreases as the gas disk shrinks until the significantly smaller maximum circular velocity $\sim$ 30 km/s is reached. Nonetheless, the velocity field generally remains rather robust during the merger. For the lower mass system, which depicts a smaller amplitude of rotation initially, the velocity field is much less conspicuous and ordered during and after the merger. Note that at the end, the maximum rotation signal is found for what we have defined as the "face-on" view of the system, although this characterization is debatable given the spheroidal shape of the remnant.

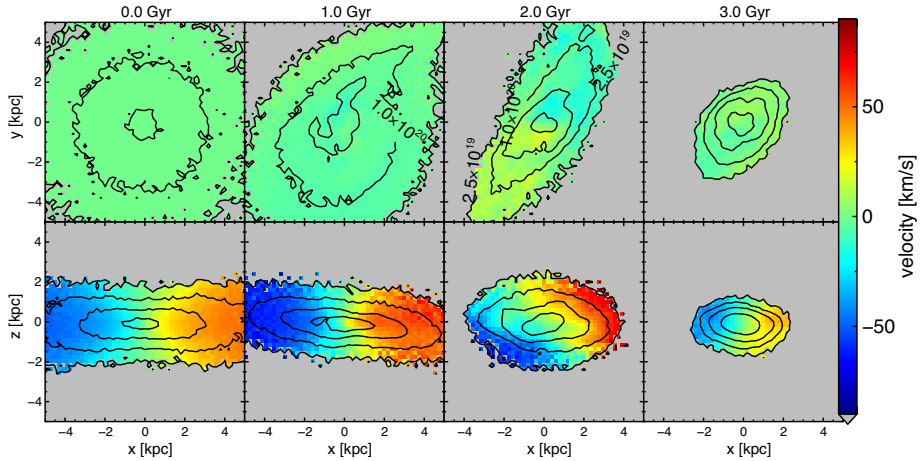

Figure 3.7 – Face-on (top) and (bottom) edge-on gas contours for model A with $R_g = 2R_d$ merging with a 20% mass satellite on a radial, co-planar orbit depicted in Fig. 3.4, initially (far left) and after 1 (middle left), 2 Gyr (middel right) and 3 Gyr (far right). The plane of the disk in determined by the angular momentum of the inner 50% of the initial stellar particles, so the rotation in the gas can be in a different plane.

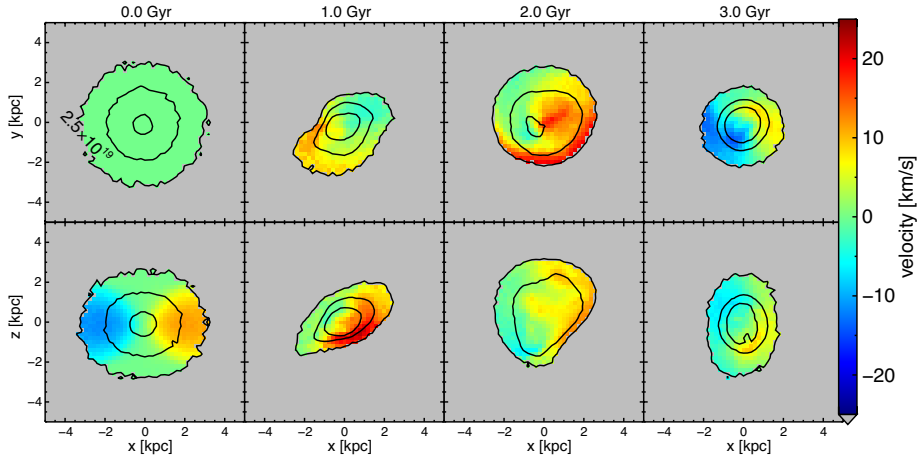

Figure 3.8 – Same as Fig. 3.7 now for the D1 system depicted merging with a satellite as shown in Fig. 3.5.

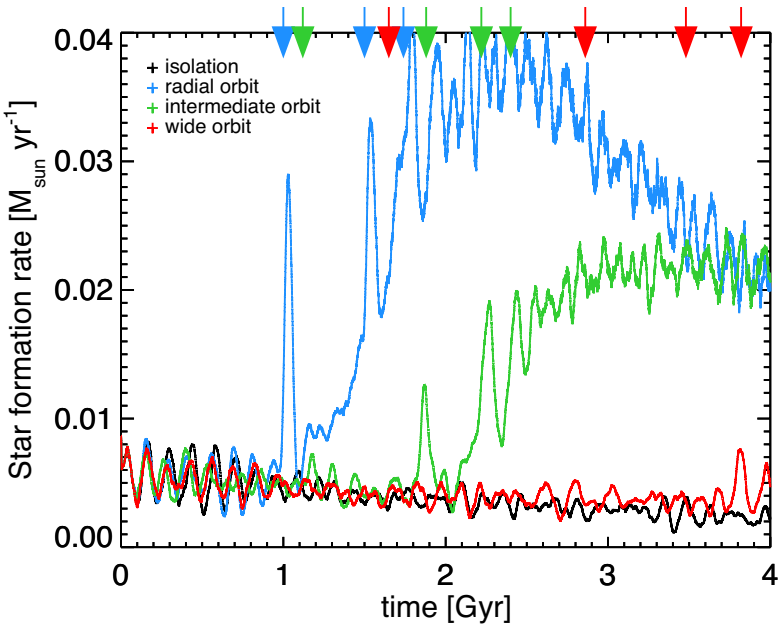

Figure 3.9 – Star formation rates for model A with $R_g = 2R_d$: in isolation (black) and experiencing a 1:5 merger with a high concentration, $c = 25$, satellite on a planar orbit: radial with first pericenter within the stellar disk (blue), less radial with first pericenter just outside the stellar disk (light green), and even less radial with $r_{\rm peri} \approx 20$ kpc (red). A number of pericentric passages of the satellite during the different simulations are indicated by the arrows at the top of the figure.

3.3.2 Variation in properties of the satellite

For a significant effect, the satellite must reach the stellar and gas disks of the dwarf galaxy within a short timescale to be apparent in our simulations. Satellites on orbits that are close to circular will take a longer time to sink to the center. This is longer than the few Gyr run-time of our non-cosmological simulations to limit environmental and cosmological effects, such as the lack of cosmic gas inflow. Moreover, the strength of the perturbation depends on the average density ratios of the satellite to the host. To explore the dependencies of the mergers on the satellite's properties we consider a number of different orbits, and satellites with different concentrations (and central densities), for three different mass ratios: $1:5$ (our default), $1:10$, and $1:20$.

The satellite orbit

Figure 3.9 compares the star formation rates for the dwarf galaxy model A experiencing a 1:5 merger with the same (high concentration) satellite on three different orbits. For less radial orbits the disk forms large tidal spiral arms

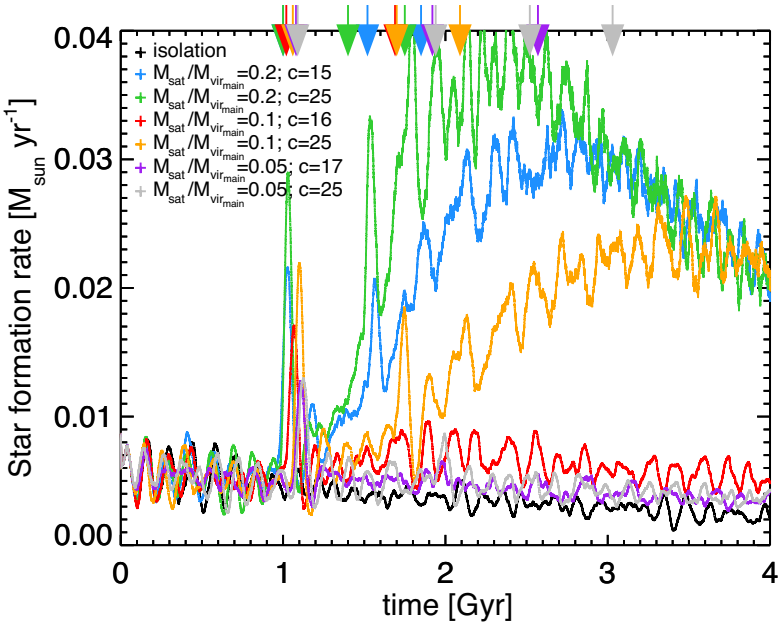

Figure 3.10 – Star formation rates for model A with $R_g = R_d$: in isolation (black), and with a satellite on a planar radial orbit with $M_{\rm sat}/M_{\rm vir_{main}} = 0.2$ ($c_{\rm sat} = 15$ blue; $c_{\rm sat} = 25$ green), $M_{\rm sat}/M_{\rm vir_{main}} = 0.1$ ($c_{\rm sat} = 16$ red; $c_{\rm sat} = 25$ orange), and $M_{\rm sat}/M_{\rm vir_{main}} = 0.05$ ($c_{\rm sat} = 17$ purple; $c_{\rm sat} = 25$ gray). A number pericentric passages of the satellite during the different simulations are indicated by the arrows at the top of the figure.

(compare for example Figs. 3.A1 and 3.A2 in the Appendix) and the subsequent increase in star formation only starts when the satellites comes within ~ 3 kpc of the center. For the most extreme example shown here (the red line in Fig. 3.9) this happens only at 3.5 – 4 Gyr, i.e. at the end of the simulation run.

For more circular orbits the spiral arms that are generated in the gas (and stellar) disk are more pronounced. Nevertheless, for the radial orbit the gas is much more concentrated after the merger, which suggests that more gas is funnelled to the center due to tidal torques.

We also experimented with different inclinations for the satellite orbit with respect to the plane of the disk (see Figs. 3.A3 and 3.A4 for examples). In general we find that an inclination of 30 degrees has a larger effect on the morphology and kinematics of the stellar disk (see also our collissionless simulations described in Chapter 2) but drives less gas to the center and produces a smaller increase in star formation rates compared to a co-planar orbit.

Satellite mass and concentration

For our default setup the satellite mass is 20% of the virial mass of the host dwarf galaxy. This choice is motivated by the fact that interactions with such objects can be devastating and may not be so rare. Helmi et al. (2012) have estimated that dwarf galaxies experience on average 1.5 such encounters in a Hubble time, but encounters with smaller mass objects are certainly more common in the ΛCDM cosmological model.

We explore the effect of 1:10 and 1:20 mergers for the most massive dwarf galaxy (model A) with $R_g = 2R_d$, and place the satellites on a radial, planar orbit. We consider satellites following the mass–concentration relation from Muñoz-Cuartas et al. (2011) and also having a higher concentration of $c_{\rm sat} = 25$.

The resulting SFR are shown in Fig. 3.10. In all cases the amplitude of the starburst depends most strongly on the mass and secondly on the concentration of the satellite, although the latter dependance is weaker the lower the mass of the satellite. Note also that the onset of the major starburst is later for smaller mass satellites. This is because the satellite sinks in more slowly, i.e. the pericenter passages where star formation is triggered occur later.

For all satellites, higher concentration leads to slower mass loss, hence to more damage to the host. This results in a larger increase in its SFR and to a stronger morphological disturbance of stellar and gaseous disks, with the final gas distribution being more centrally concentrated. While gas gets blown out of the disk in all cases, in the interaction with the highest mass and $c_{\rm sat} = 25$ satellite the gas reaches $\sim 4r_{\rm vir}$, about twice as far as for the other cases.

In summary, in all cases (although very minor for $M_{\rm sat}/M_{\rm vir_{main}} = 0.05$), there is a first strong peak of star formation at the first pericentric passage of the satellite, and a more extended in time starburst, also driven by the merger. Secondary peaks associated to subsequent pericentric passages are also present but are generally less conspicuous.

The structure of the dwarf galaxy itself can significantly alter the effects of the minor merger on the gas and star formation. We vary the halo mass and concentration, the gas fraction and extend of the gas disk, and the scale length and scale height of the stellar disk. Of these, varying stellar disk parameters causes only very minor differences on the gas and star formation.

3.3.3 Influence of properties of the host dwarf galaxy

Gas distribution

We explore now the evolution of a disky dwarf galaxy when the gas disk has different extent than the stellar disk, since this characteristic is often seen in large spiral galaxies. A comparison between the merger properties for model A with $R_g = 2R_d$ and with $R_g = R_d$ can be seen in Fig. 3.11.

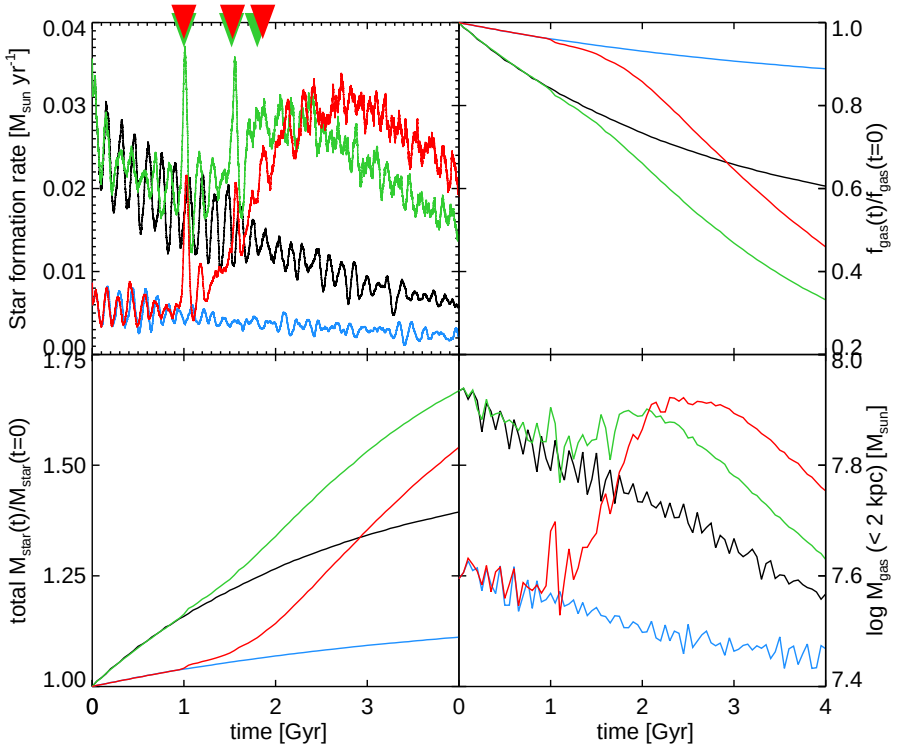

Figure 3.11 – Star formation rates, relative gas fractions, relative stellar masses, and gas masses in the central parts for model A with $R_g = R_d$ and $R_g = 2R_d$ in isolation (black and blue, respectively) and during the merger (green and red, respectively). The arrows at the top of the top-left figure indicate a few pericentric passages of the satellite during the simulations shown.

Due to the lower initial star formation rate for the more extended (and hence lower surface density) gas disk, this system has a larger gas reservoir at the time of the merger (see top right panel). The bottom right panel of Fig. 3.11 shows that the increase in gas mass near the centre is much higher for the initially more extended disk during the merger (red curve) than for the less extended gas disk (green). However, the final increase in stellar mass is still higher for the system with $R_g = R_d$, mostly due to its initially larger star formation rate.

In general more extended disks have lower star formation rates both in isolation and during the merger. This is because the same amount of gas is distributed over a larger area and therefore the amount above the star formation threshold is much lower.

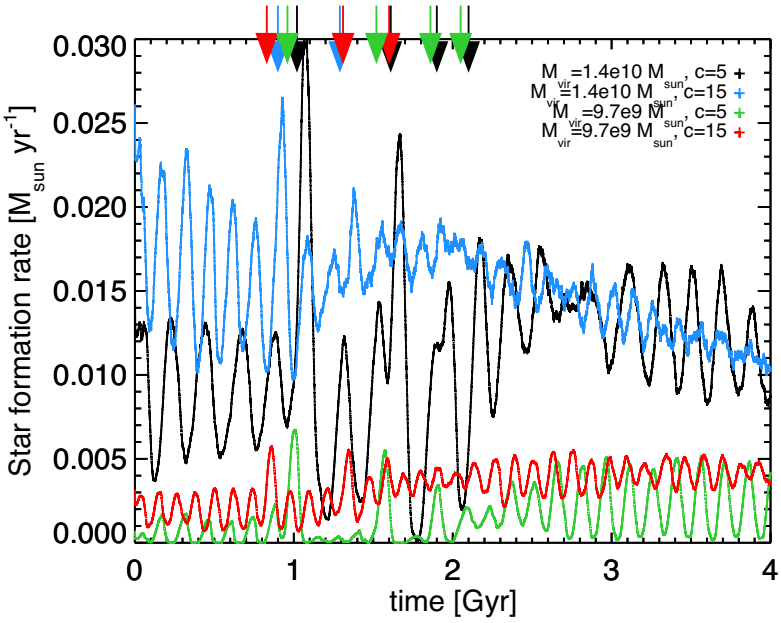

Figure 3.12 – Star formation rates for models C and D with $R_g = R_d$, $f_{\rm gas} = 0.9$, $z_0 = 0.3R_d$, and a dark matter halo concentration of either $c = 5$ (C3 and D2) or $c = 15$ (C1 and D1), during the 1:5 merger with a satellite on a prograde orbit with an inclination with the plane of the disk of 0 (for models C) or 30 degrees (for models D). A number pericentric passages of the satellite during the different simulations are indicated by the arrows at the top of the figure.

Host's dark matter halo mass and concentration

Figure 3.12 shows the star formation rates for the dwarf galaxies models C1 and C3, and D1 and D2 which have different dark matter halo concentration and mass. Even though the difference in halo mass between models C and D is only a factor 1.4, due to the steepness of the halo mass – stellar mass abundance matching relations (Behroozi et al. 2013a; Moster et al. 2013; Garrison-Kimmel et al. 2014; Sawala et al. 2015) the difference in stellar mass and gas mass is a factor 2.5. For these runs the stellar disk is thick initially ($z_0 = 0.3R_d$), $R_g = R_d$, $f_{\rm gas} = 0.9$, and the satellite has a mass of 20% of the host halo on radial orbit with an inclination of 0 or 30 degrees. As noted before, higher (central) mass implies initially higher SFR, and thus also during and after the merger (compare black and green, and blue and red curves). A less concentrated host halo initially has a puffier gas disk and lower SFR, but during a merger the enhancement in the SFR is larger, as depicted by the black curve in Fig. 3.12 for model C3. Therefore we see that the susceptibility of the system to a merger depends both on virial mass of the host and on its concentration.

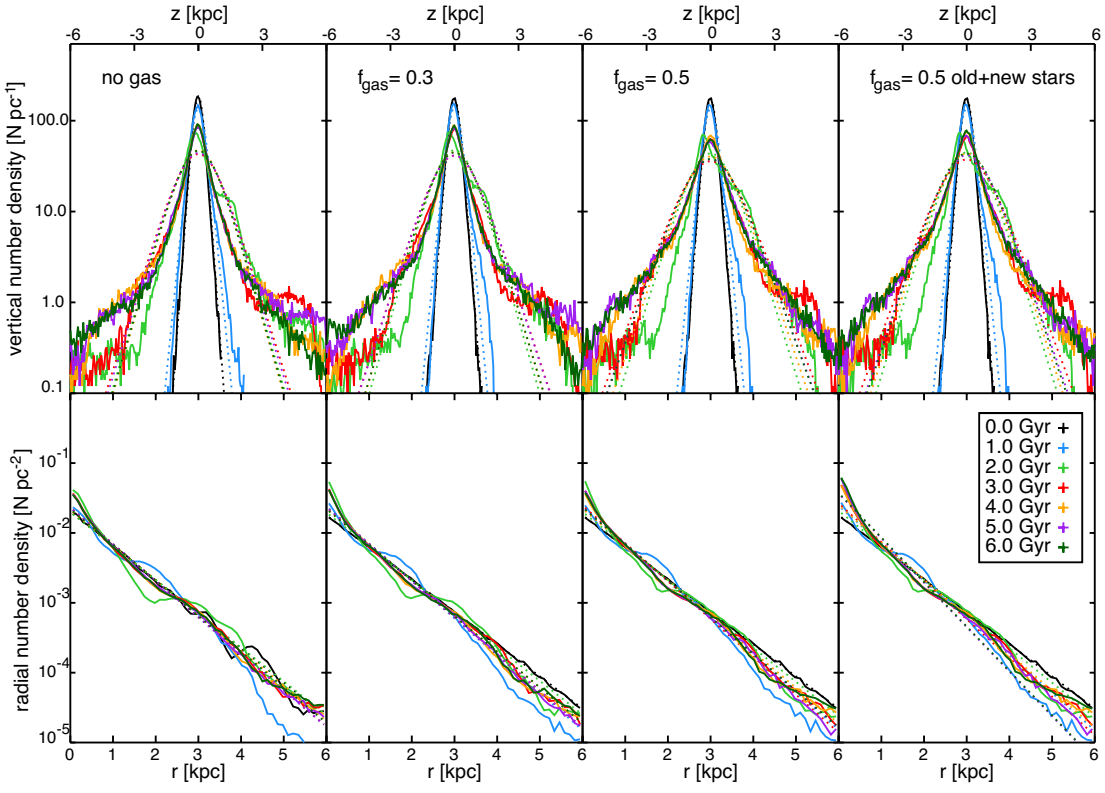

Figure 3.13 – Vertical (top panels) and radial (bottom panels) density profiles (solid lines) during the merger simulations with intervals of 1 Gyr for the *FNX*-like system: fully collissionless (left), with $f_{\rm gas} = 0.3$ and $f_{\rm gas} = 0.5$ (middle), and with $f_{\rm gas} = 0.5$ including the newly formed stars (right). The dotted lines show the maximum likelyhood fitted profiles: isothermal (sech^2) and exponential in the top and bottom panels, respectively.

3.4 Comparison with collissionless runs

In this section we compare the dwarf galaxies models C4 and C5 (*disk3-gas*) and E1 and E2 (*FNX-gas*) with the results from the "equivalent" collissionless simulations in Chapter 2. Our focus is on how the presence of the gas changes the characteristics of the merger remnants.

The morphological and kinematical changes to the stellar component of both dwarf systems are very similar to the fully collissionless runs. We exemplify this in Fig. 3.A5 of the Appendix, and more quantitatively in Figure 3.13. This figure shows the vertical and radial density profiles of the stellar disks of the panels) and for the counterparts with $f_{\rm gas} = 0.3$ and $f_{\rm gas} = 0.5$ (central panels). In all three cases the strongest changes occur during the first pericenter passages of the satellite, within 2 Gyr of the start of the simulations. The differences in the structural evolution of the stellar disks are surprisingly small. The major difference is that for the fully collisionless system the radial profile of the disk is slightly more unstable and has more substructure. Even the newly formed stars in the runs including gas do not significantly change the stellar density profiles as can be seen in the rightmost panels of Fig. 3.13, but they give rise to a small central bulge (compare the bottom panels). For the more massive *disk3* (models C4 and C5) the inclusion of gas also has a small effect, and leads to a slightly thicker stellar disk in the post-merger phase, more so for higher gas fractions.

The effect of the merger on the kinematics of the stars do not differ much when gas is included in the disk. For example, for the *FNX*-like system in both cases the rotation decreases over the whole disk while the circular velocity increases due to the accretion of the dark matter satellite. All velocity dispersions increase, and even increase slighly more in the presence of a gas disk. This might be due to the fact that the gas disk is not very thin due to the low mass of the dwarf galaxy halos and therefore exerts less of a pull toward the disk midplane compared to a purely stellar disk.

Therefore, the presence of gas in the disk has no significant influence on the effects of minor mergers on dwarf galaxies. This is in striking contrast to what happens in similar simulations for higher (Milky Way) mass galaxies (see discussion in Sect. 3.6).

3.5 Comparison to observations

We now compare the properties of our simulated dwarf galaxies, in isolation and during the merger, with the observational samples described in Table 3.4. This comparison includes systems from HI-selected, as well as mass-selected samples and general compilations.

The left panel of Fig. 3.14 shows the SFR versus stellar mass $M_\star$ for the systems discussed in this chapter compared to observational values reported

Table 3.4 – Observational samples used

Reference	Sample	Properties used
Hunter & Elmegreen (2004) and Hunter & Elmegreen (2006)	94 Im, 24 BCD, and 18 Sm galaxies	$M_{\rm HI}$, M_V, $B-V$, R_d, SFR, μ_0
Weisz et al. (2012)	185 galaxies from 11HUGS[a] and the *Spitzer* LVL survey[b]	$M_\star$, M_B, SFR
Huang et al. (2012)	229 low HI mass galaxies from the ALFALFA survey[c]	$M_\star$, $M_{\rm HI}$, SFR
Ott et al. (2012)	VLA-ANGST survey: 35 galaxies from the ANGST survey[d]	M_B, SFR
Warren et al. (2012)	31 nearby low-mass galaxies from THINGS[e] and the VLA-ANGST survey[f]	M_B, SFR
McQuinn et al. (2015)	12 galaxies from the SHIELD survey[g]	$M_{\rm HI}$, $M_\star$, SFR, M_B
Karachentsev et al. (2004)	all-sky catalog of basic optical and HI properties of (451) neighboring galaxies with $D < 10$ Mpc or $V_{\rm LG} < 550$ km/s	$v_{\rm rot}$, b/a

Notes [(a)] Kennicutt et al. (2008); Lee et al. (2011); [(b)] Dale et al. (e.g., 2009); [(c)] Giovanelli et al. (2005); [(d)] Dalcanton et al. (2009); [(e)] Walter et al. (2008); [(f)] Ott et al. (2012); [(g)] Cannon et al. (2011).

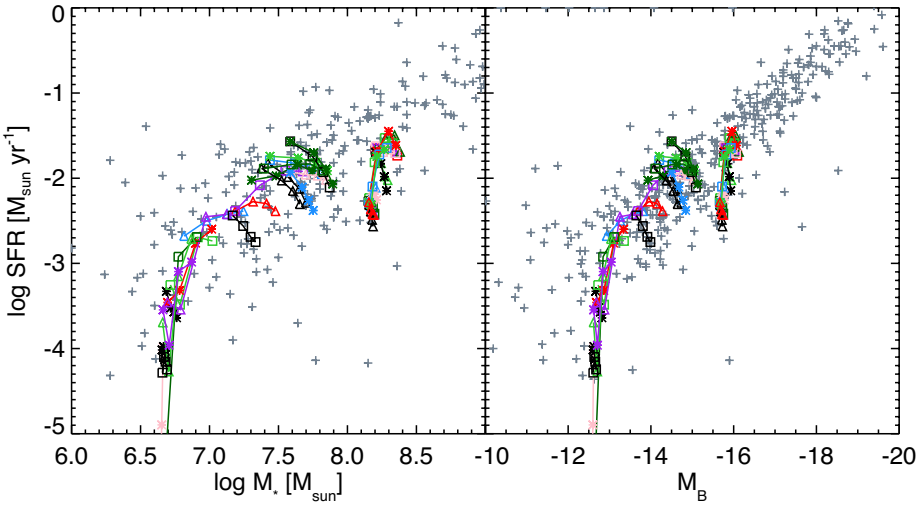

Figure 3.14 – Star formation rates versus stellar masses and B-magnitude in intervals of 1 Gyr in comparison to the dwarf galaxies from Weisz et al. (2012), Huang et al. (2012) and McQuinn et al. (2015) for the left panels, and in addition for the right panel from Ott et al. (2012), Warren et al. (2012), and Hunter & Elmegreen (2006). Note that the stellar mass grows during the simulations.

in Weisz et al. (2012), Huang et al. (2012), and McQuinn et al. (2015). For each simulation the evolution of the SFR and $M_\star$ are plotted at four epochs in steps of 1 Gyr, from 1 Gyr after the start of the simulation. The black symbols correspond to the runs in isolation while in color we show the mergers. Overall the star formation rates match very well those from observations for their stellar masses.

To estimate the luminosities and surface brightness of our simulated galaxies we need to assume mass-to-light ratios for the stellar particles. One possibility for the stellar particles formed during the simulation would be to use stellar population models as we know their ages. For the stellar particles initially present in the simulation however the age distribution would be arbitrary. Therefore, we instead fitted a linear relation to the $\log M_\star$–B magnitude distribution for the galaxies in the observations of Weisz et al. (2012) and McQuinn et al. (2015) and apply it to the simulated dwarf galaxies. The resulting estimated values are roughly consistent with an average mass-to-light ratio of $M_\star/L_{B,\star} \sim 0.5$, which is quite reasonable as the light is very strongly dominated by young stars. The right panel of Fig. 3.14 shows SFR against the B-magnitude for our systems and for a larger sample of observations. Good agreement is also found in this case.

Figure 3.15 shows that also the initial gas fractions and their evolution in time agrees very well with observations. The downward trend seen in the

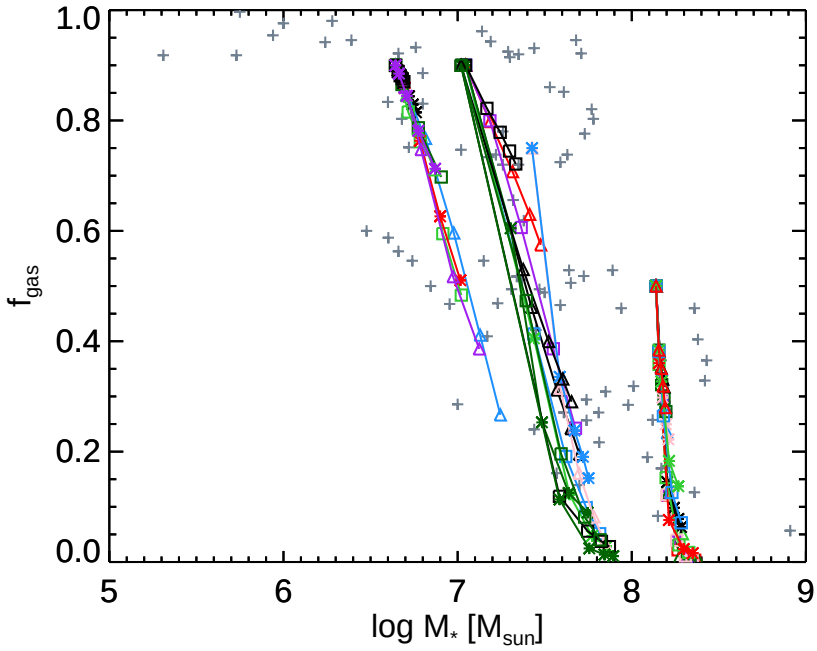

Figure 3.15 – Gas fractions versus stellar masses in intervals of 1 Gyr in comparison to the dwarf galaxies from Huang et al. (2012), and McQuinn et al. (2015). Since the stellar mass grows during the simulations and that we do not include fresh gas inflow, the gas fraction of our simulated systems necessarily decreases.

simulated systems is due to the fact that we do not include fresh gas inflow. However, sampled at an arbitrary point in time, the match is quite remarkable.

We compute radial surface brightness profiles for the face-on disks and fit an exponential profile to derive the disk scale length and half-light radius. This process is similar to that of Hunter & Elmegreen (2006) and we compare our disks with their observational results. We derive central surface brightness using the mass/luminosity within the innermost, 0.1 kpc, bin in projection. The results are shown in Fig. 3.16. It is clear that while the higher mass disks match very well with the observations, the lower mass systems seem to be more extended and fainter, compared to the observations. There are two main possible reasons for this: low surface brightness, extended systems are harder to observe. On the other hand, the method we used to compute the initial size of the systems and to set up our simulations (using the disk mass and properties of the halo following Mo et al. 1998) might break down for lower mass systems, as they typically are thicker and deviate from being thin disks.

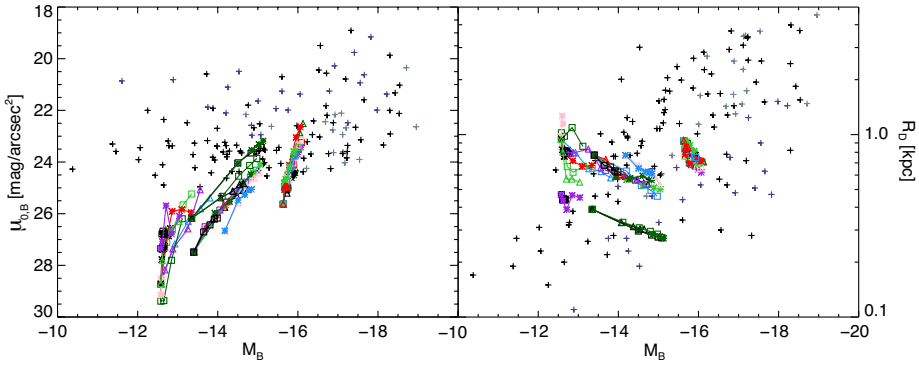

Figure 3.16 – Central surface brightness (left) and disk scale lengths (right) versus absolute magnitudes in intervals of 1 Gyr compared to irregular dwarf galaxies (black), blue compact dwarfs (dark blue), and Magellanic spirals (gray) from Hunter & Elmegreen (2006). Note that the stellar mass grows (mostly in the center) and so the magnitude and disk scale length decreases and the central surface brightness increases during the simulations.

To estimate the effect of this we have also run the two lower mass systems with initial disk scale lengths half their default values and, not surprisingly, we find that they agree better.

In Fig. 3.17 we compare our "observed" axis ratios and rotational velocities to the observed axis ratios of all galaxies with $w_{50} < 200\,\mathrm{km/s}$ from the catalog of nearby galaxies (450 when the Milky Way is excluded) by Karachentsev et al. (2004). The intrinsic axis ratios are computed by fitting an ellipsoid to the stellar particle distribution (normalized by the ellipsoidal distance of the particles within this ellipsoid, Allgood et al. 2006). The ellipsoids are centered around the center of mass defined by the stellar component and the axis ratios computed for particles within major axis length of $a \sim 1.4\,\mathrm{kpc}$, but we find similar results when considering particles within $a \sim 4\,\mathrm{kpc}$ and even $a \sim 14\,\mathrm{kpc}$. These intrinsic minor-to-major axis ratios are in agreement for most of the merger remnants, but the default initial disks are often thinner than the observations[1]. However, most systems will not be observed edge-on, and therefore to provide more realistic estimates of "observed" axis ratios we put each system at 100 random inclinations and compute projected axis ratios at five evenly spaced epochs during the simulation.

For the rotational velocities, we assume that for the observational sample $v_{\mathrm{rot}} \approx 0.5 \times w_{50}$ and compute the rotational velocities for our modelled systems as the mean between the minimum and maximum value of the velocity maps

[1]Initially thicker disks ($z_0 = 0.5 R_d$), which might be expected for dwarf galaxies that form in gas that has cooled less efficient than in larger disks (Kaufmann et al. 2007; Robertson & Kravtsov 2008), already agree well with the observational points.

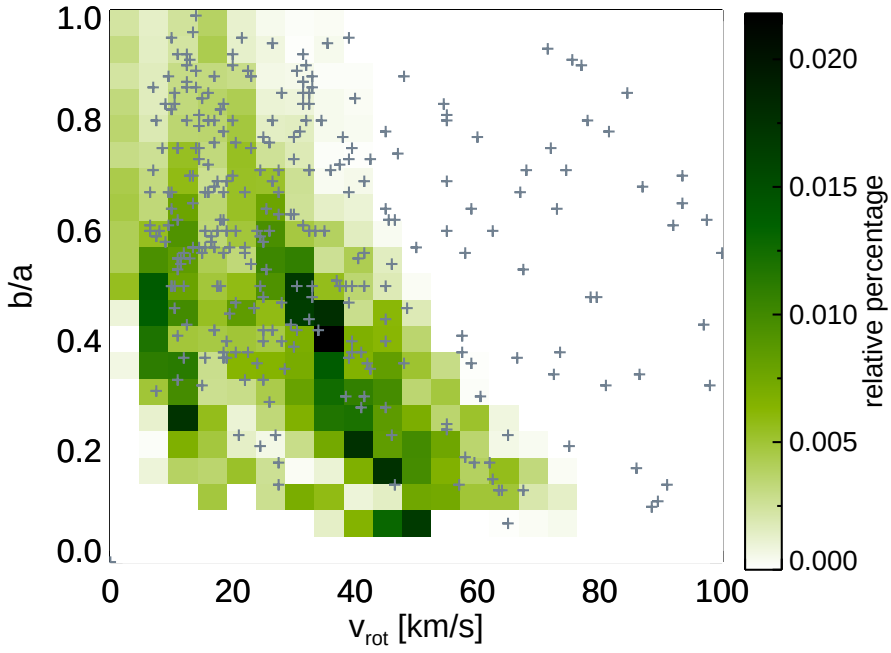

Figure 3.17 – Distribution of "projected" axis ratios and rotational velocity for 100 random inclinations at intervals separated by 1 Gyr during each of the simulation runs, compared to galaxies with $v_{\rm rot} = 0.5 \times w_{50} \leq 100$ km/s from the catalog of nearby galaxies (Karachentsev et al. 2004) (gray). Darker colors indicare a higher density of objects in this plane.

(as in Fig. 3.7), which give the velocities in the disk within the column density contour of 2.5×10^{19} N cm^{-2} (which is close typically to $\sim 2R_D$).

Inspection of Figure 3.17 shows when including the (random) inclination angle, the sample of simulated dwarf galaxies agrees very well with the observed sample. Surprisingly, even the trend that the lower-mass stellar disks are more extremely perturbed by the minor merger is apparent.

Overall, our systems agree well with properties of observed dwarf galaxies.

3.6 Discussion

In this chapter we show the effects of minor mergers with a dark satellite on gas-rich dwarf galaxies. The isolated systems a carefully set up and we have explored the effects of varying the subgrid parameters on the results. Our star formation and feedback prescriptions lead to reasonable dwarf galaxies when

evolved in isolation, and their properties are fairly stable against varying these parameters. Only extremely efficient feedback gives a completely different and unrealistic evolution. We have also carried some of the merger experiments for different feedback schemes and found that the effects of the merger on the gas and star formation evolution to be very robust against such changes.

When comparing the fully hydrodynamic models to the collissionless minor merger simulations of Chapter 2 we have found that the evolution of the stellar components of the dwarf galaxies is rather similar. Even though the gas absorbs and dissipates some of the energy injected via the merger, the morphological transformations that the stellar disks experience are still very important. This is in contrast to what has been reported in the literature for Milky Way-size systems where the effect is significantly reduced when gas is included (e.g., Hopkins et al. 2009; Moster et al. 2010). This is probably due to the gas being much colder in larger disk galaxies and therefore having a stronger stabilizing effect on the stars in the disk.

An important question is how often the process discussed in this chapter would happen for dwarf galaxies in different environments, at different redshifts and with different masses. As the CDM halo mass function is almost scale-free (with small differences due to halo formation times van den Bosch et al. 2005; van den Bosch & Jiang 2014), dwarf galaxies will have a spectrum of perturbers very similar to that of an $L_\star$ galaxy. Helmi et al. (2012) estimate that the number of minor mergers for low galaxy efficiency systems ($M_d/(M_{\rm vir} \times f_{\rm bar}) = 5\%$) where the satellite is at least as massive as the disk at pericenter, with the pericenter within 30% of the virial radius, is ~ 1.5 within a Hubble time. The simulations discussed in this chapter were for systems with even smaller galaxy efficiencies experiencing 1:5 and 1:10 mergers with dark satellites, albeit on very radial orbits. This means that almost every dwarf galaxy should have experienced a minor merger with major effects during its lifetime. Predictions and their dependencies on environment, redshift and dwarf galaxy mass will be presented Chapter 5.

Several definitions of a starburst exist in the literature (e.g., Knapen & James 2009; McQuinn et al. 2010; Bergvall et al. 2015). The birthrate parameter, b=SFR/$\langle$SFR$\rangle$ is often used, and compares the current SFR or the peak of the burst to the average SFR over the past Gyr or even the lifetime of the system. For the more massive systems in our simulations the SFR in isolation is very similar to their initial stellar mass divided by a Hubble time, and the birthrate goes up to $b \sim 3$, or even $b \sim 10$, during the merger, depending on the configuration. The lower mass systems have typically more bursty star formation histories even in isolation. We may characterize $b \sim 1$ between these small bursts, $b \sim$a few during bursts in isolation, but during the merger we find $b > 10$. Therefore the increase in star formation rates the simulated systems experience can be qualified as starburst events. Also when computing the gas consumption timescale, $\tau_{\rm gas} = M_{\rm gas}$/SFR, there is agreement with

the literature. For the star formation rates in isolation, the gas consumption timescales are long $\tau_{\rm gas}^{\rm isolation} > 10$ Gyr, while these drop significantly by factors of a few during the merger events.

Although observations suggest that only a small fraction of dwarf galaxies are currently experiencing a starburst ($\sim 6\%$ according to Lee et al. 2009), this might be just a fraction of the total number of dwarf galaxies that experienced starbursts in their lifetimes (Lee et al. 2009).

3.7 Conclusions

We performed a suite of controlled, minor merger simulations between carefully set-up gaseous dwarf galaxies and their (dark) satellites. These interactions can give rise to a strong increase in the star formation rates in the dwarf galaxies. The increase is in the form of large sharp bursts during pericenter passages, as well as of extended boosts due to tidal torques funnelling gas toward the center. The gas and stellar disks show severely disturbed morphologies in most cases, especially for lower mass hosts experiencing a 1:5 merger. The gas disks can develop grand tidal tails and their remnants depict a much more concentrated final distribution in some cases. For the lowest mass systems explored ($M_\star \lesssim 1.1 \times 10^7 M_\odot$), the merger can completely destroy the stellar disk. These objects become spheroidal-like and have bursty star formation in their center. In contrast to simulations of Milky Way-like systems, the presence of gas in the disk of the dwarf galaxies does not diminish the effect of the merger on the stellar component. Our simulations that include gas show that the strong heating and evolution of the stellar disk is almost completely identical to the collisionless case.

We have explored the dependence of the mergers and their remnants on the host and satellite masses, dark matter halo concentrations, satellite orbits, gas fractions, and structure of the stellar and gas disks. To have a significant impact, a dark satellite must have at least 10% of the mass of the host. More generally, the strength of the merger's effects decreases with lower satellite masses, but this depends on satellite halo concentration: a very dense low-mass dark satellite can survive longer than one of lower concentration, and therefore have stronger effects. Orbits in the plane of the disk cause stronger starbursts, while inclined orbits perturb the stellar components more effectively. Satellites on radial orbits cause stronger starbursts than those on more circular ones.

When the hosts have lower concentrations, the merger induces stronger morphological changes (as in Chapter 2) but in general also lower star formation rates. This is because SFR correlates with gas density, which depends in turn on the total mass distribution in the region probed by the gas disk. Also the gas fraction and distribution, as well as stellar disk masses and distributions, determine the amount of gas that has high enough densities for

star formation, thereby directly affecting the amplitude of the starburst that a dwarf experiences during a merger.

Both our initial systems and their remnants compare well with the observational properties of a large selection of irregular dwarf galaxies and blue compact dwarfs. Even systems that are strongly perturbed as a result of a merger with a dark satellite fall within the scatter seen in the observations. This implies that such events might well be happening but may not be fully evident. We have yet to identify the "smoking gun" of the dark merger scenario. However, this also shows that the effects of interactions with dark satellites, which are naturally expected within a CDM cosmology, are likely to play a role in the diversity of the dwarf galaxy population.

Acknowledgements. We are grateful to Claudio Dalla Vecchia, Joop Schaye, Carlos Vera-Ciro, Alvaro Villalobos and Volker Springel for providing code. AH acknowledges financial support from the European Research Council under ERC-StG grant GALACTICA-240271 and the Netherlands Research Organisation NWO for a Vici grant.

3.A Additional figures

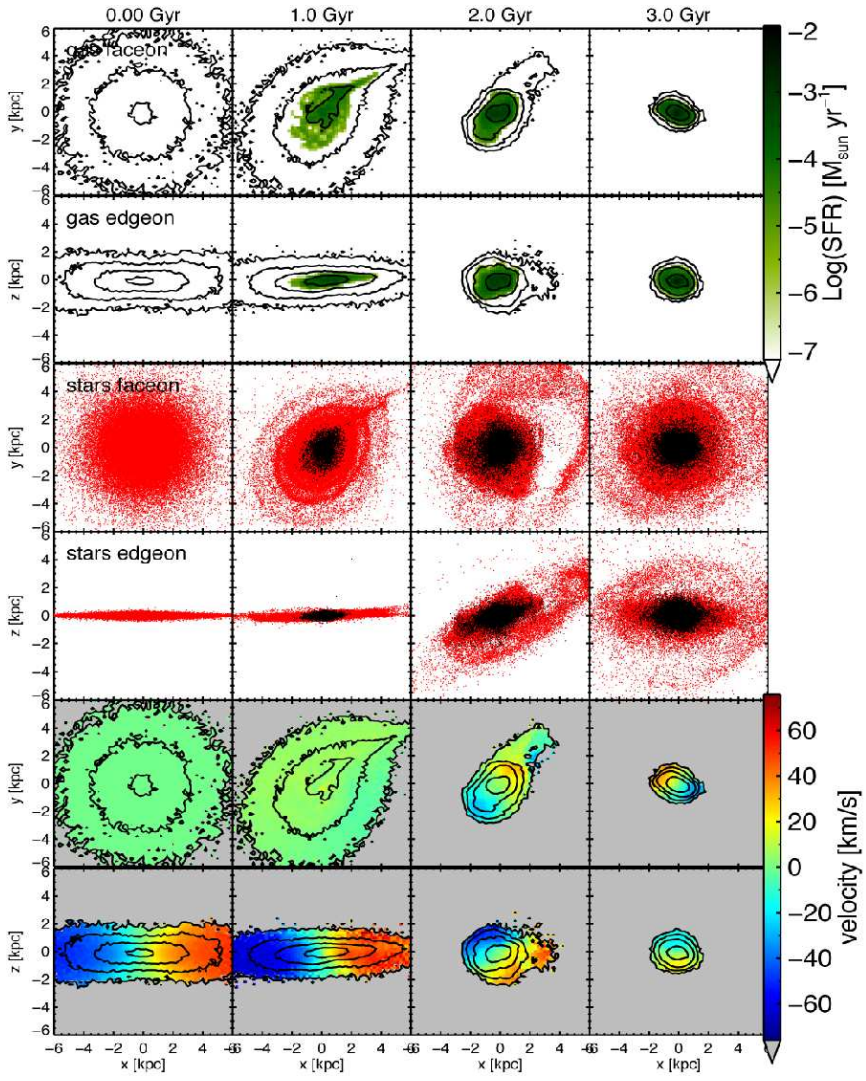

Figure 3.A1 – Evolution of model A with $R_g = 2R_d$, merging with the $c = 25$ satellite on a planar, very radial orbit, at different times during the merger. The top rows show the face-on and edge-on, respectively, view of the gas in the disk (contours at 0.25, 1, 4, and 16×10^{20} N cm^{-2}) with the gas that is currently forming stars highlighted in green (see colorbar for relative values). The third and fourth rows from the top show the old stellar component in red, and newly formed star particles in black. The bottom panels show the gas contours with the gas velocity perpendicular to the contour plane.

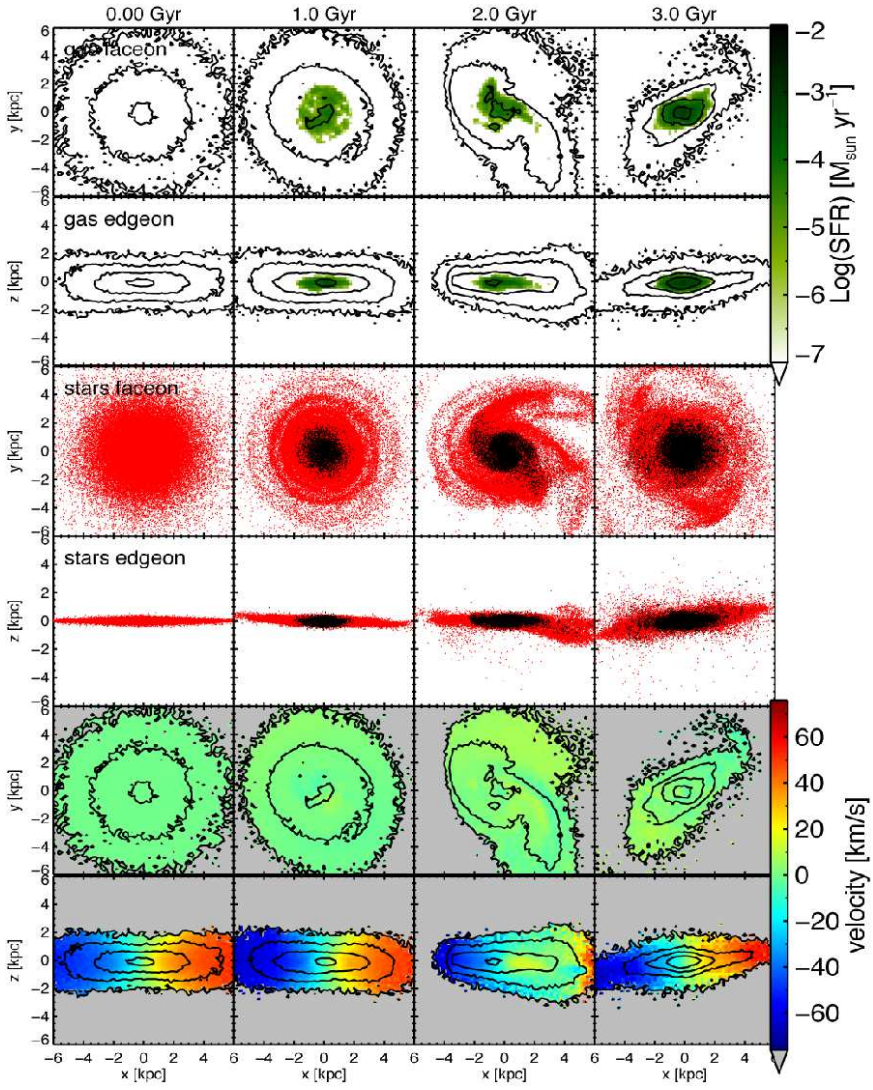

Figure 3.A2 – Same as Fig. 3.A1 for model A with $R_g = 2R_d$, with the $c = 25$ satellite on a planar, less radial orbit.

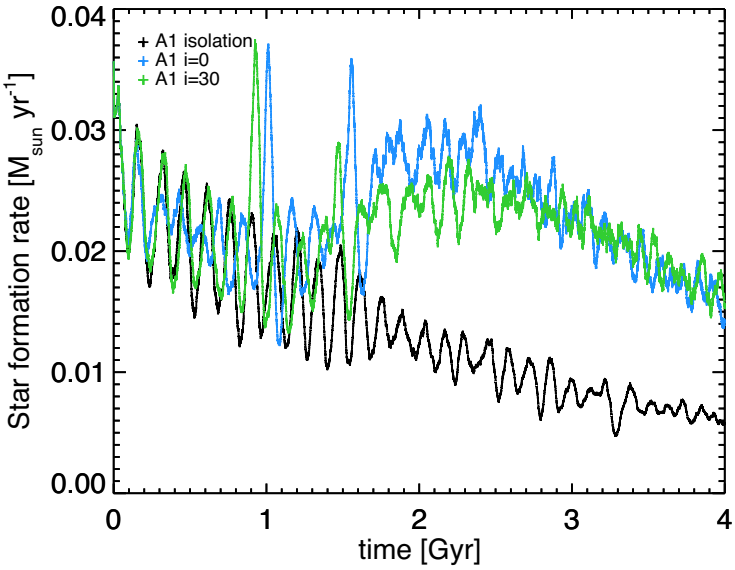

Figure 3.A3 – Star formation rates for model A with $R_g = R_d$ during the 1:5 merger with a satellite on a prograde, very radial orbit with an inclination with respect to the plane of the disk of 0 or 30 degrees.

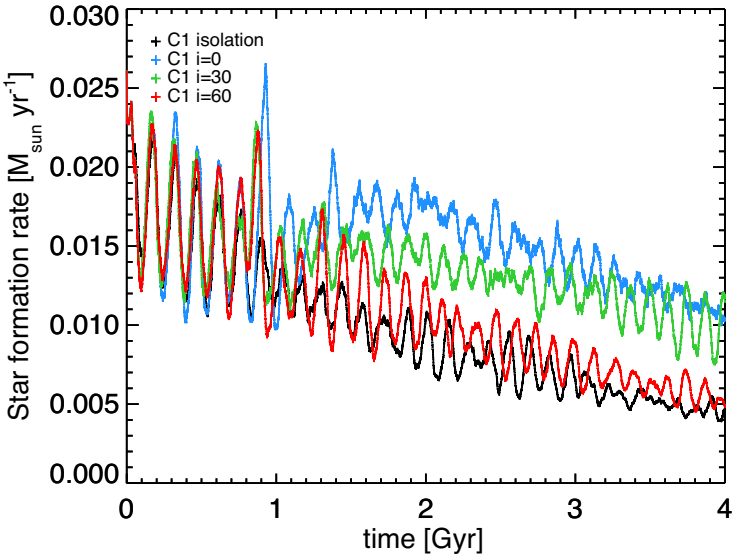

Figure 3.A4 – Star formation rates for model C1 with $R_g = R_d$ during the 1:5 merger with a satellite on a prograde, very radial orbit with an inclination with respect to the plane of the disk of 0, 30, or 60 degrees.

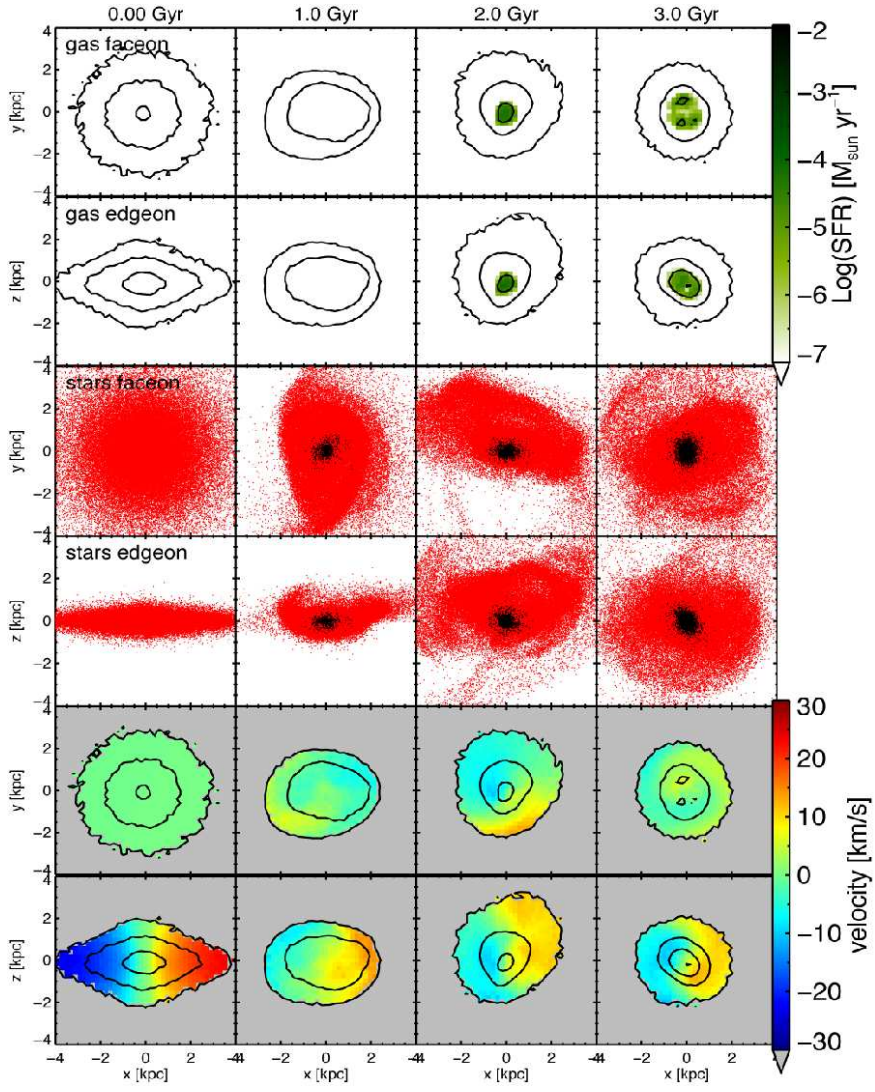

Figure 3.A5 – Same as Fig. 3.A1 for the *Fornax-analog* dwarf galaxy with $f_{\rm gas} = 0.5$ (model E1), merging with the 20% mass satellite on a 30-degrees, radial orbit.

4

Structural characterization of minor mergers of dwarf galaxies with dark satellites

— Based on *Dark influences III. Structural characterization of minor mergers of dwarf galaxies with dark satellites*, T. K. Starkenburg, A. Helmi & L. V. Sales, submitted to Astronomy & Astrophysics —

Abstract

In the current concordance cosmology small halos are expected to be completely dark and can significantly perturb low-mass galaxies during minor merger interactions. These interactions may well contribute to the diversity of the dwarf galaxy population. Dwarf galaxies in the field are often observed to have peculiarities in their structure, morphology, and kinematics as well as strong bursts of star formation without apparent cause. We aim to characterize the signatures of minor mergers of dwarf galaxies with dark satellites to aid their observational identification. We explore and quantify a variety of structural, morphological, and kinematic indicators of merging dwarf galaxies and their remnants using a suite of hydrodynamical simulations. The most sensitive indicators of mergers with dark satellites are large asymmetries in the gaseous and stellar distributions, enhanced central surface brightness and starbursts, and velocity offsets and misalignments between the cold gas and stellar components. In general merging systems span a wide range of values of the most commonly used indicators, while isolated objects tend to have more confined values. Interestingly, we find in our simulations that a significantly off-centered burst of star formation can pinpoint the location of the dark satellite. Observational systems with such characteristics are perhaps the most promising for unveiling the presence of the hitherto, missing satellites.

4.1 Introduction

In a Λ cold dark matter (ΛCDM) universe the halo mass function is scale-free: independently of their mass, halos have their own system of substructures (van den Bosch et al. 2005; van den Bosch & Jiang 2014). Below a halo mass of $\sim 10^{9.5}\ M_{\odot}$ however star formation is expected to be largely inhibited due to reionization, photo-ionization of the gas, and possibly feedback (Gnedin 2000; Hoeft et al. 2006; Kaufmann et al. 2007; Okamoto et al. 2008; Gnedin et al. 2009; Li et al. 2010; Sawala et al. 2013). The galaxy mass function is thus not scale-free, while the stellar mass-halo mass function is predicted to steepen toward lower halo masses (Behroozi et al. 2013a; Moster et al. 2013; Kormendy & Freeman 2016; Garrison-Kimmel et al. 2014; Sawala et al. 2015). Therefore, dwarf galaxy halos have significantly lower baryon fractions and their satellites are expected to be predominantly completely star-less, or dark (Helmi et al. 2012).

Although the Hubble sequence (Hubble 1926) generally describes well the properties of large galaxies, on the scale of dwarfs no clear classification scheme exists. The simplest separation is given by the fact that star forming dwarfs often show irregular morphologies, while those quiescent have generally a spheroidal appearence. It is still not well understood how these classes of objects are related (see e.g. Mateo 1998; Tolstoy et al. 2009). Furthermore, blue compact dwarfs (BCDs), and more generally starbursting dwarf galaxies, have central regions that are very blue reflecting a centrally concentrated young stellar population so bright that an underlying older, population is not readily apparent (e.g., Gil de Paz et al. 2003; Paudel et al. 2015). Just like dwarf irregulars, BCDs can furthermore depict irregular morphologies and kinematics, with star formation regions far from the center (Taylor et al. 1995; Ekta & Chengalur 2010; López-Sánchez 2010; Holwerda et al. 2013; Lelli et al. 2014b; Knapen & Cisternas 2015). Off-center bursts of star formation have also been observed in a number of extremely metal-poor galaxies as well as large differences in the average line-of-sight velocities between the HI gas and the stellar component (Filho et al. 2013, 2015). As galaxy mass lowers, it appears as if a higher fraction of the systems are peculiar.

We have recently postulated that this may be partly explained by dwarf galaxies experiencing minor mergers with dark companions (Helmi et al. 2012). In Chapter 2 and Chapter 3 (Starkenburg & Helmi 2015; Starkenburg et al. 2016, respectively), we have shown that such minor mergers can significantly alter the morphological properties of dwarf galaxies. The disturbances induced by dark objects are much more dramatic on this scale because of the lower galaxy formation efficiency (i.e. lower baryon fractions) in dwarfs compared to giant galaxies. One of the most direct imprints in gas-rich dwarfs is a vast increase in star formation: both in short bursts (during close passages of the satellite) as well as sustained high star formation rates lasting several Gyrs. In

Chapter 3 we have shown that the general properties of our simulated dwarf systems compare very well to a large sample of dwarf irregular galaxies and blue compact dwarfs from the literature.

In this chapter we provide a quantitative characterization of the morphological and kinematic properties of the dwarf systems during the minor merger events and thereby facilitate a more detailed comparison to observations. For the analysis we use morphological descriptions that have been applied to characterize where galaxies lie along the Hubble sequence, to disentangle interacting from isolated systems, and to describe the stellar distributions in major mergers of $\sim L_\star$ or larger spiral galaxies, such as the *CAS* (Concentration, Asymmetry and Smoothness) and *GM* (Gini coefficient and M20) indicators (see e.g. Conselice et al. 2000; Conselice 2003; Abraham et al. 2003; Lotz et al. 2004, and references therein). These have also been applied to describe the stellar components of isolated irregular dwarf galaxy samples (Conselice 2003; Lotz et al. 2004), to characterise the gas distribution in starbursting dwarf galaxies (Lelli et al. 2014b) and in simulations of major mergers (Holwerda et al. 2011a) as well as a variety of observational samples (Holwerda et al. 2011b,c,d,e, 2012, 2013, 2014).

This chapter is organised as follows. The hydrodynamical simulations are described concisely in Sect. 4.2, while in Sect. 4.3 we focus on one specific simulated system and highlight key tidal features as the merger takes place. In Sect. 4.4 we introduce the morphological and kinematic indicators used and compare the results to some observational samples. We present a brief comparison to two dwarf galaxies with peculiar properties, namely IC10 and NGC6822 in Sect. 4.5. The summary and conclusions are given in Sect 4.6.

4.2 Method

We analyze the structural properties of dwarf galaxies during minor mergers with dark satellites for a suite of hydrodynamical simulations recently presented in Chapter 3. The simulations span a range of initial conditions for the dwarf galaxy, its satellite and a variety of orbital configurations for the interaction. They were performed using the OWLS (Schaye et al. 2010) version of Gadget-3 (based on Springel et al. 2001b; Springel 2005) with implementations for star formation and feedback as described in Schaye & Dalla Vecchia (2008); Dalla Vecchia & Schaye (2008).

The host dwarf galaxy consists of a dark matter halo, a stellar disk and a (generally more radially extended) gaseous disk. Both the stellar and gaseous disks follow an exponential surface density profile with radius, while the vertical distribution of the gas is determined by requiring hydrostatic equilibrium, and assuming an effective equation of state of the multiphase ISM model by Schaye & Dalla Vecchia (2008); Dalla Vecchia & Schaye (2008). Star formation occurs when the density of the gas is above a threshold of

$0.1\,\mathrm{cm}^{-3}$, while at lower densities the gas follows an isothermal equation of state. Feedback and stellar winds are included such that the systems, when evolved in isolation, are self-regulating over the timescale of the simulations.

The satellite is a dark subhalo (no baryons) that follows an NFW-profile with two different concentrations ($c = 15$, $c = 25$). In most of the simulations, it has an initial mass of 20% of that of the dwarf galaxy's halo, but we also consider 5% and 10% mass ratios. The satellite is typically placed on a fairly radial orbit with different inclinations and is launched close to its apocenter near the virial radius of the host.

For the numerical parameters, we use 10^6 particles for the dwarf's dark matter halo, a softening length $\epsilon_{\rm halo} = 0.025$ kpc, 2×10^5 particles in baryonic mass, divided among the stellar and gas disks according to the gas fraction $f_g = M_{\rm gas}/(M_{\rm gas} + M_\star)$, with softening length $\epsilon_{\rm bar} = 0.008$ kpc. The satellite is modeled with 10^5 particles that have a softening length $\epsilon_{\rm sat} = 0.016$ kpc.

We will focus mostly on one of the simulated dwarfs, which we refer to as model-A (see Chapter 3), and which has $M_{\rm vir} = 5.6 \times 10^{10}\ M_\odot$, a concentration $c = 9$, and $M_\star = M_{\rm gas} = 1.4 \times 10^8\ M_\odot$ ($f_g = 0.5$). The stellar disk has a radial scale-length $R_d = 0.93$ kpc and vertical scale-height $z_0 = 0.1R_d$. We will also report results for smaller mass systems in the range $M_{\rm vir} = 9.7 \times 10^9$–$2.2\times10^{10}\ M_\odot$, and $M_\star = 4.4\times10^6$–$2.7\times10^7\ M_\odot$, with gas fractions of $f_g = 0.75$–0.9, and a range of disk thickness and halo concentrations (models B, C, and D in Chapter 3).

4.3 Tidal effects

As an example, we present in Fig. 4.1 the evolution of the model-A dwarf as it experiences a 20% minor merger. In this example the dwarf has initially a very extended gas disk, with scale length $R_g = 4R_d$. This set-up is motivated by observations showing that gas may spread out much farther than the stars (see e.g. Begum et al. 2008; Filho et al. 2015, and references therein).

The satellite in Figure 4.1 has a high concentration ($c = 25$) and is launched from apocenter at a distance of ~ 51 kpc on a fairly radial orbit with tangential velocity $v_t = 0.5v_{\rm vir}$. During close passages to the disk the satellite (marked with a cross) induces large tidal tails in both the gas and stars, as shown in the second column of this figure.

During the second pericentric passage (third column of Fig. 4.1), the satellite meets up with a gaseous tidal tail and causes a local overdensity where star formation takes place (as can be seen from e.g. the newly born stars plotted in blue in the middle panel). The star formation rate density in this tidal structure is higher than in the center so that the brightest star forming core at this point in time is actually located more than 7 kpc from the center. Intriguingly, such features are also found in XMP galaxies (Filho et al. 2013).

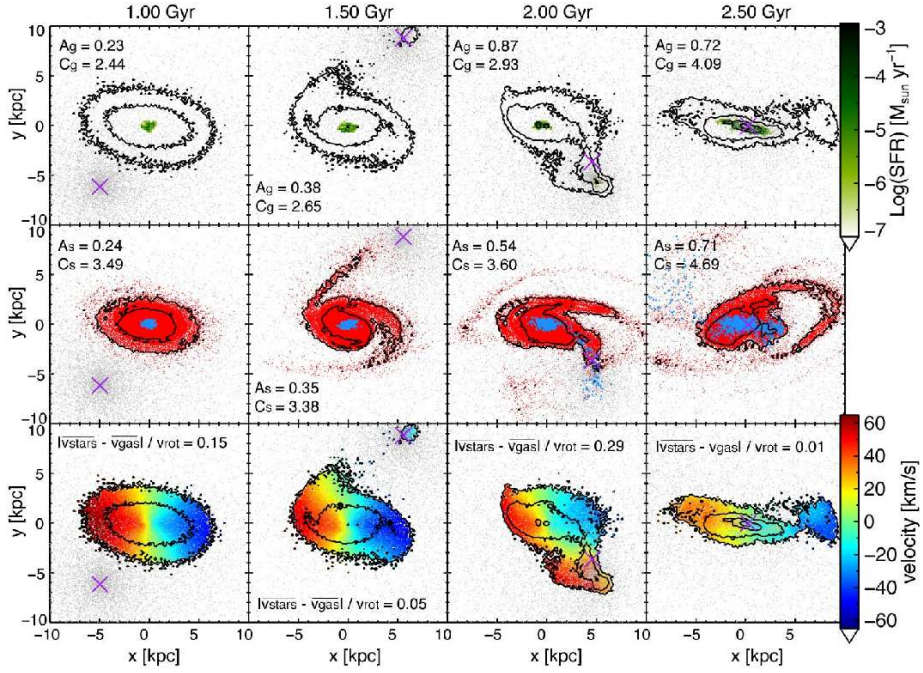

Figure 4.1 – Evolution of the model-A dwarf galaxy with $R_g = 4R_d$, merging with a 20% mass ratio dark satellite with $c = 25$ on a co-planar relatively radial orbit. All figures show an inclined view of the disk, 60 degrees from face-on. The top row shows the cold gas in the disk (contours at 0.4, 1, 4, and 10×10^{20} N cm^{-2}) with the star-forming gas highlighted in green (see colorbar for SFR values). The central row panels show the old stars in red, and those newly formed in blue, along with two surface brightness contours of 25 mag/arcsec^2 and 28 mag/arcsec^2, obtained assuming an $M/L = 0.5$ for all stellar particles. The bottom panels show the gas contours with the gas velocity maps. In all panels the satellite is shown in grey (5% of the particles are plotted), with the purple cross denoting its center of mass. The insets indicate the values of asymmetry, concentration and difference in average velocity between stars and gas computed as described in Sect. 4.4.

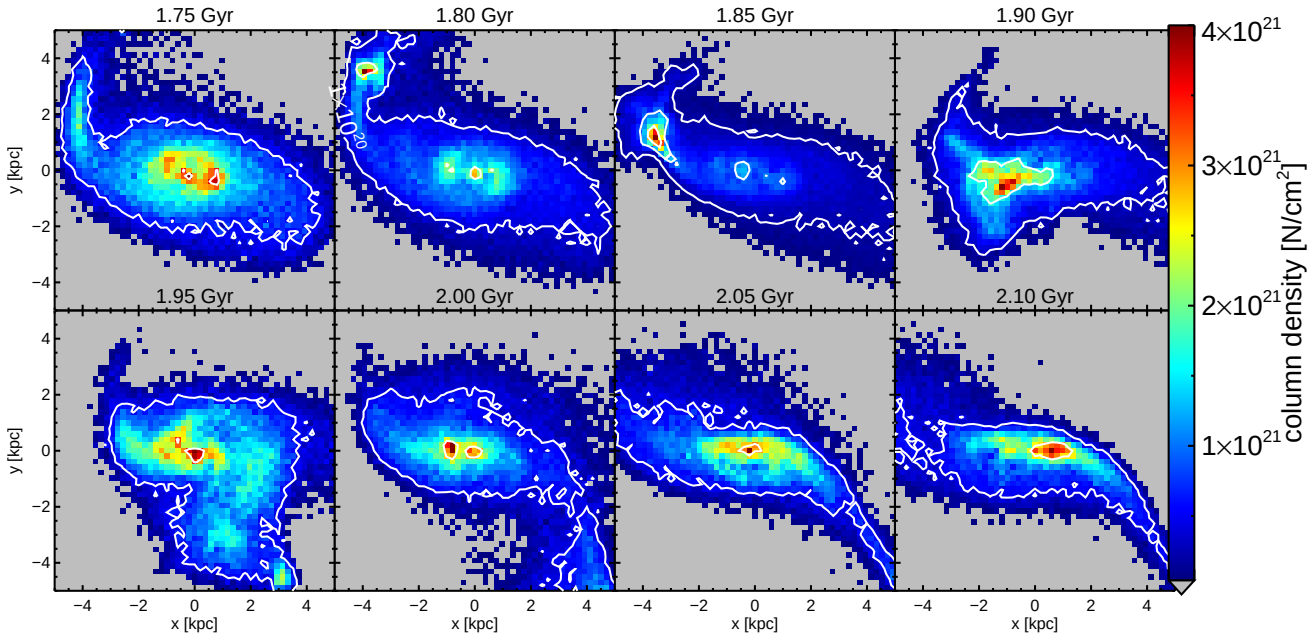

Figure 4.2 – Evolution of the inner parts of the dwarf galaxy shown in Fig. 4.1 around the time the satellite merges with the host. The threshold is 0.4×10^{20} N cm^{-2} and the contours indicate 1, 4, and 10×10^{20} N cm^{-2}; see colorbar for the relative values.

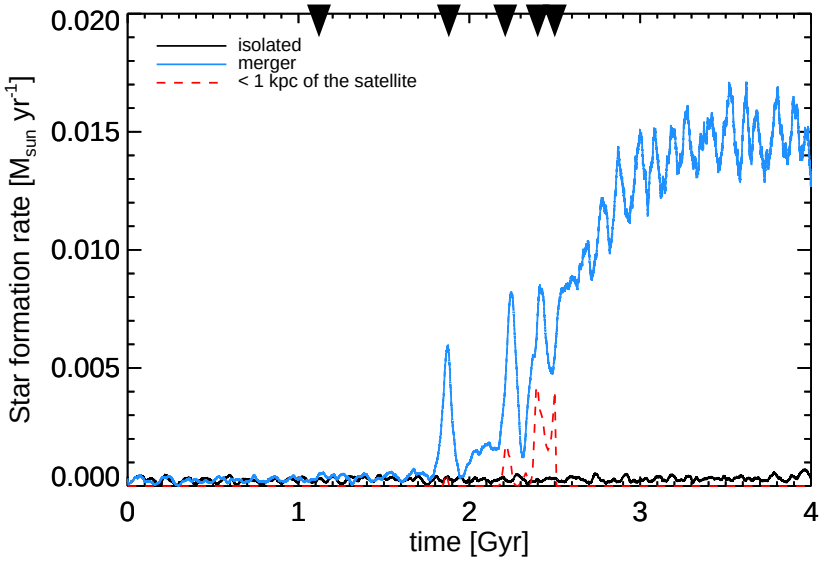

Figure 4.3 – The blue curve shows the evolution of the star formation rate of the dwarf galaxy shown in Figures 4.1 and 4.2, while the black curve is for the same model-A dwarf run in isolation. The star formation rate in the tidal tail within 1 kpc of the position of the satellite is shown with the red dashed curve, and makes up to 75% of the total SFR in the system around the time of the merger. The satellite is completely disrupted after 2.5 Gyr, but its effects on the SFR are longlasting. The pericenter passages of the satellite are indicated by the black arrows.

4.3.1 Morphological parameters

Fig. 4.2 zooms into the gas column densities in the inner parts of the dwarf galaxy around this time. Note again the high gas densities in the tidal tails and how they correlate with the position of the satellite. Also, and as expected, the young star particles trace the motion of the satellite through the disturbed dwarf galaxy (see the blue points in the middle row of Fig. 4.1). Since these dominate the light, the associated local star-forming regions may well be the analogues of what is seen in XMP galaxies (Filho et al. 2013, 2015).

Figure 4.3 shows the star formation rate (SFR) during the encounter. The blue curve shows that the total SFR has pronounced peaks during the pericentric passages of the satellite. Interestingly, during the later passages, up to 75% ($4 \times 10^{-3}\ M_{\odot}\ \mathrm{yr}^{-1}$) of the total star formation takes place in the tidal tail at the location of the satellite (red curve). Subsequently the total SFR increases, due to the gas that is channeled to the center, and reaches a plateau

around a value that is at least a factor 10 higher than for the equivalent dwarf in isolation.

In summary, besides the characteristic starburst, signatures of the merger can be found in the morphology of the old stellar disk, the distribution and morphology of the young stellar population that is formed during the encounter, and in the morphology and kinematics of the gas. The gaseous and stellar disks show distinguishable effects both in the outskirts and in the inner parts. Interestingly, in the simulated system shown here star forming regions outside the center pinpoint the location of the merging dark satellite.

4.4 Quantitative measures of structure

Although clear effects can be seen in the simulated dwarf galaxy which are due to the minor merger, it is important to quantify these in order to make comparisons to observations. A variety of quantitative structural descriptions of the morphology and kinematics of galaxies have been put forward in the literature. Morphologically the structure is often characterized by the *CAS* (concentration, asymmetry, and smoothness; Conselice 2003) and *GM* (Gini and M20; Lotz et al. 2004) indicators. Additionally for dwarf irregulars and BCDs, the difference in central surface brightness obtained by fitting the inner and outer regions is also used (Hunter & Elmegreen 2006; Papaderos et al. 2008). For XMP galaxies, the often used indicators include differences in the average velocity, and in the position angles of the HI gas and stellar components (Filho et al. 2015, 2013). We apply the morphological indicators to our simulations and present the results in Sect. 4.3.1, while we focus on the results of the kinematic indicators of the stellar and gas disks in Sect. 4.4.1.

We estimate the morphological *CAS* and *GM* parameters, including modifications by Lelli et al. (2014b); Holwerda et al. (2011d), on a grid with initial size of 20 by 20 kpc which is cropped to the regions above a fixed threshold, and a default bin size of 0.2 kpc. The thresholds adopted are close to those reported for observational studies in the literature, $N_{HI} > 4 \times 10^{19}$ cm^2 for the surface density of neutral gas and $\mu_V < 28$ mag/arcsec^2 for the V-band magnitude, respectively. This means that in practice each bin holds at least 12 gas particles. For the stars, assuming an average $M/L = 0.5$, appropriate for the V-band, each bin holds at least 4 stellar particles. The calculations are done on the stellar densities though (in $M_\odot$/kpc^2).

For many of the indicators it is necessary to define the center of the system. This is done by fitting a 2-dimensional Gaussian to the projected density (although our results are robust to the centering method used), with the threshold values described above. We have tested the effect of different thresholds ($N_{HI} > 10^{19}$ cm^2, $N_{HI} > 10^{20}$ cm^2, $\mu_V < 26$ mag/arcsec^2, and $\mu_V < 30$ mag/arcsec^2), and assumptions regarding the mass-to-light ratios for the newly formed and original stellar populations, and found that when a

sufficient area of the system is visible (as smaller systems can mostly disappear below the thresholds) the numerical values for the morphological parameters can change but the trends stay intact.

Definitions

We now describe in detail the different morphological indicators we use in our analysis.

- *Concentration*
  This describes the distribution of light over the image:

  $$C = 5\log\left(\mathrm{r}_{80}/\mathrm{r}_{20}\right) \tag{4.1}$$

  where r_{80} and r_{20} are the radii which contain 80% and 20% of the total light (Conselice 2003), where for a purely exponential profile $C = 2.7$, and for a de Vaucouleurs profile $C = 5.2$. Note that since the projected surface brightness and gas column densities are computed on a grid, we determine a slightly coarse value of C.

- *Asymmetry*
  This describes the relative difference in intensity when the image is rotated 180 degrees:

  $$A = \frac{\sum_{i,j} |I(i,j) - I_{180}(i,j)|}{\sum_{i,j} I(i,j)} \tag{4.2}$$

  where $I(i,j)$ is the intensity of the pixel (i,j) (Conselice 2003). Note that with this definition, $0 < A < 2$.

- *Outer Asymmetry*
  To give more weight to the outer parts, Lelli et al. (2014b) have defined an outer asymmetry parameter as:

  $$OA = \frac{1}{N} \sum_{i,j} \frac{|I(i,j) - I_{180}(i,j)|}{|I(i,j) + I_{180}(i,j)|} \tag{4.3}$$

  (Lelli et al. 2014b), where we define N as the number of the pixels with $|I(i,j) + I_{180}(i,j)| > 0$. Note this outer asymmetry (OA) indicator is more susceptible to noise.

  Both for the A and OA parameters the detectability of asymmetries in the outskirts depend greatly on the surface brightness or column density thresholds, especially for low mass and low surface brightness galaxies.

- M_{20}
  This parameter is a relative second order moment of the 20% brightest pixels and was originally introduced as an alternative to the concentration parameter:

$$M_{20} = \log\left(\frac{\sum_i^k M_i}{M_{\rm tot}}\right) \tag{4.4}$$

  where $\sum_i^k I_i < 0.2 I_{\rm tot}$ and $M_i = I_i[(x_i - x_c)^2 + (y_i - y_c)^2]$ (Lotz et al. 2004). Its advantage compared to the concentration is that there is no assumption of circular symmetry and that it is more sensitive to phenomena like multiple nuclei that are thought to be common in merging, or post-merging, systems.

- *Gini coefficient*
  This statistic originally used in economics to describe the distribution of wealth within a society, was adapted to galaxy morphology by Abraham et al. (2003). It correlates with concentration but does not assume circular symmetry. We use the Gini coefficient based on the second intensity moment weighted by position:

$$G(M) = \frac{1}{2\bar{M}N(N-1)} \sum_{i,j} |M_i - M_j| \tag{4.5}$$

  where again $M_i = I_i[(x_i - x_c)^2 + (y_i - y_c)^2]$, and $\bar{M}$ denotes the mean of M_i over all N pixels (Lotz et al. 2004; Holwerda et al. 2011d). $G(M)$ is larger when the brightest pixels are farther from the center. We only consider the pixels above the threshold in this calculation, which tends to lower the values of $G(M)$ compared to including the background pixels.

- *Excess central surface brightness:* $|\mu_{0,HSB} - \mu_{0,LSB}|$
  We compute this by taking the difference in the central bin's surface brightness obtained from exponential fits to the inner and outer parts of the system.

Results

Fig. 4.4 shows the evolution of three morphological indicators: asymmetry, concentration and M_{20}, for the gas distributions in the system shown in Fig. 4.1, for five different random inclinations. This figure evidences that the indicators have a strong time dependence as the merger occurs, and that each evolves quite differently with time. For example, the asymmetry

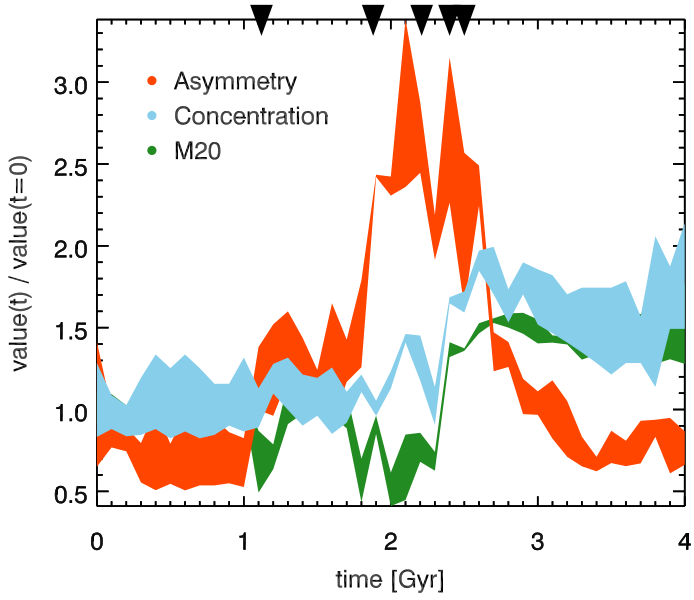

Figure 4.4 – The distribution of the asymmetry A (red), concentration C (blue), and M_{20} (green) values for the gaseous disk for 5 random inclinations in time intervals of 0.1 Gyr for the model-A dwarf during the minor merger shown in Fig. 4.1. These quantities have been normalised to their median (over all inclinations) initial value. The pericenter passages of the satellite are indicated by the black arrows.

(in red) increases with time reaching a peak value when the satellite fully merges, as a consequence of the extended tidal tails clearly seen in Fig. 4.1, and decreases strongly afterwards. The concentration (in blue) also increases significantly around the time of the merger but it remains high afterwards, as a result of the strong central influx of gas. On the other hand, the M_{20} (in green) depicts an oscillatory behaviour with peaks that roughly coincide with each pericenter passage of the satellite. Because M_{20} is negative, and in this figure it has been normalised to the initial value, these peaks actually imply that the 20% brightest pixels are more centrally concentrated, with the dips indicating high gas densities at larger radii, suggesting that star formation occurs at larger distances. The plateau value at late times reflects the strong centrally concentrated sustained enhancement in gas density. The parameters describing the stellar distribution follow similar trends. Fig. 4.5 shows the distribution of photometric indicators for all the merger simulations we have carried out with the model-A dwarf. These simulations include a range of different orbits (orbital inclinations and eccentricities), concentrations

and masses for the satellite, and varying extents of the gaseous disk. For each simulation the parameters are calculated initially (i.e. in isolation) and at 1, 2, 3, and 4 Gyr and at five random inclination angles for each point in time.

This figure shows that isolated systems (blue for gas, and green for stars) tend to occupy small regions of parameter space, whereas for mergers (red for gas and black for stars) a broad range of parameter values appears to be plausible. At face value, there is no parameter (combination) for which mergers and isolated systems can be fully separated. This might not be unexpected given the time variability of the parameters. Furthermore, cases in which the effects of the merger on the gas and stellar disks are small (e.g. if the satellite sinks in very slowly or has too low mass, or for specific viewing angles), will be hard to disentangle from systems in isolation.

Most isolated systems have low values for concentration, asymmetry, outer asymmetry, and $G(M)$. On the other hand, for the mergers, the asymmetry parameters for both the gas and the stars spread over a much larger range. Also the outliers in M_{20} correspond to merging systems. The difference in central surface brightness can reach up to to 3 magnitudes/arcsec^2 for merging systems, but is smaller than 1 magnitude/arcsec^2 for all isolated cases.

It is therefore easier to demark regions populated by isolated systems in the parameter subspaces plotted in Fig. 4.5. For example $A < 0.38$ for the gas, $A < 0.3$ for the stars, $OA < 0.4$ for gas and stars, $G(M) < 0.4$ for the gas, and a relation $C \lessapprox 2M_{20} + 7$ for the gas and $C \lessapprox 2M_{20} + 8$ for the stars. These regions are indicated by grey lines in the figure. Interestingly we find $G(M) > 0.4$ for the HI component of merging systems, while $G(M) > 0.6$ has been put forward by Holwerda et al. (2011d), and $A > 0.4$ has been used for the stellar component in major mergers (Conselice 2003).

In Fig. 4.5 we have focused on the model-A dwarf, a relatively massive system with $M_\star = 1.4 \times 10^8 M_\odot$, and demonstrated that it may be possible to disentangle partly mergers from isolated systems. However, for lower mass dwarfs, with initial $M_\star = 4.4 - 27 \times 10^6 M_\odot$, the morphological parameters of either isolated and merging systems strongly overlap. Although a 20% merger can cause irregular features in the gas and stellar distributions (ideally resulting in higher asymmetry and outer asymmetry values), often these features are not strong enough (given reasonable thresholds) to be clearly identified by the *CAS* or *GM* indicators as being different from irregular gas densities and patchy star formation that may happen in isolation as well. Therefore, such morphological indicators are not useful to identify merger candidates in the case of low mass dwarfs.

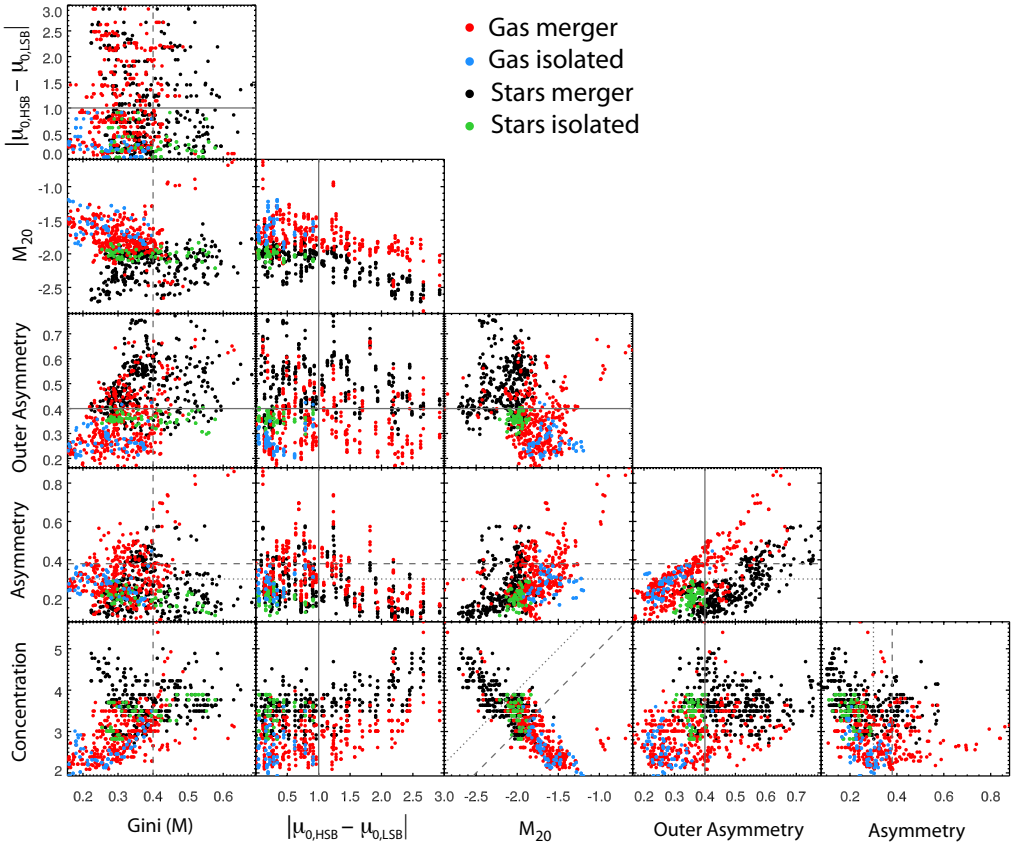

Figure 4.5 – The concentration C, asymmetry A, outer asymmetry OA, M_{20}, Gini(M), and excess central surface brightness $|\mu_{0,HSB} - \mu_{0,LSB}|$, for the gas in merger simulations (red) and in isolation (blue), and for the stars in merger simulations (black) and in isolation (green). The simulations shown correspond to the model-A dwarf, and encompass 14 different runs with varying satellite masses, halo concentrations, orbits, and radial extend of the gas disks with respect of the stellar disks (with $R_g = R_d$, $2R_d$, or $4R_d$) as described in Sect. 4.2. For more details on the simulations, see Chapter 3. The dotted, dashed and solid lines indicate regions where the isolated and merger systems are well separated for the stars, for the gas or for both, respectively.

Comparison to observations

Lotz et al. (2004) have estimated the asymmetry, concentration, and M_{20} parameters for 22 systems from a sample of isolated dwarf irregular galaxies observed in the B-band by van Zee (2000, 2001). Many of these systems are brighter than those in our simulations and seem to be more clumpy. Although the range of concentrations is similar ($2.39 < C < 4.17$), the values for M_{20} are higher ($-1.79 < M_{20} < -0.70$) than we find for the stellar components even in isolation. This implies a smoother distribution in the simulations, and this could be the result of an initial smooth set up as well as to the absence of H_2 or metal-line cooling in the simulations which could induce a patchier star formation. On the other hand, the asymmetry values are in the range of $0.01 < A < 0.45$ (Conselice 2003) and are consistent with what we find for the stellar components of isolated systems.

Lelli et al. (2014b) have described the gas outer asymmetry for 18 starburst dwarf galaxies and for a control sample of 17 dwarf irregular galaxies from the VLA-ANGST survey (Ott et al. 2012). The outer asymmetry values of the observed starburst systems are in the range $OA = 0.42 - 0.77$, with a median value of ~ 0.6, i.e. similar to the values we find in our merger simulations. On the other hand, all the simulated dwarf galaxies in isolation have outer asymmetries lower than 0.4, and hence are more comparable to those in the dwarf irregular sample, which typically have $OA \sim 0.3 - 0.5$.

From these comparisons, we may conclude that both the stellar and gas components of dwarf irregular galaxies have similar parameter distributions to the simulated dwarfs in isolation. Furthermore, the outer asymmetries seen in the gas in observations of starburst dwarf galaxies agree with those of interacting simulated dwarfs.

4.4.1 Kinematic parameters

Besides morphology, kinematics can also encode information about past merger events. For example, in our merger simulations the 3-dimensional direction of the total angular momentum vectors of the cold gas and of the stars can differ significantly, and up to 60 degrees, while for the isolated simulated dwarfs the difference is < 5 degrees. However, angular momenta cannot be directly measured from observations and so we discuss below some of the kinematic indicators that may be used instead.

- *Difference in average velocity between gas and stars*
  This has been found to be quite large for a number of extremely metal-poor (XMP) galaxies (Filho et al. 2013). In our simulations the average line-of-sight velocities are mass-weighted and computed for all particles within a bin with surface brightness or column density above the thresholds. We compare this difference to the "maximum" rotational

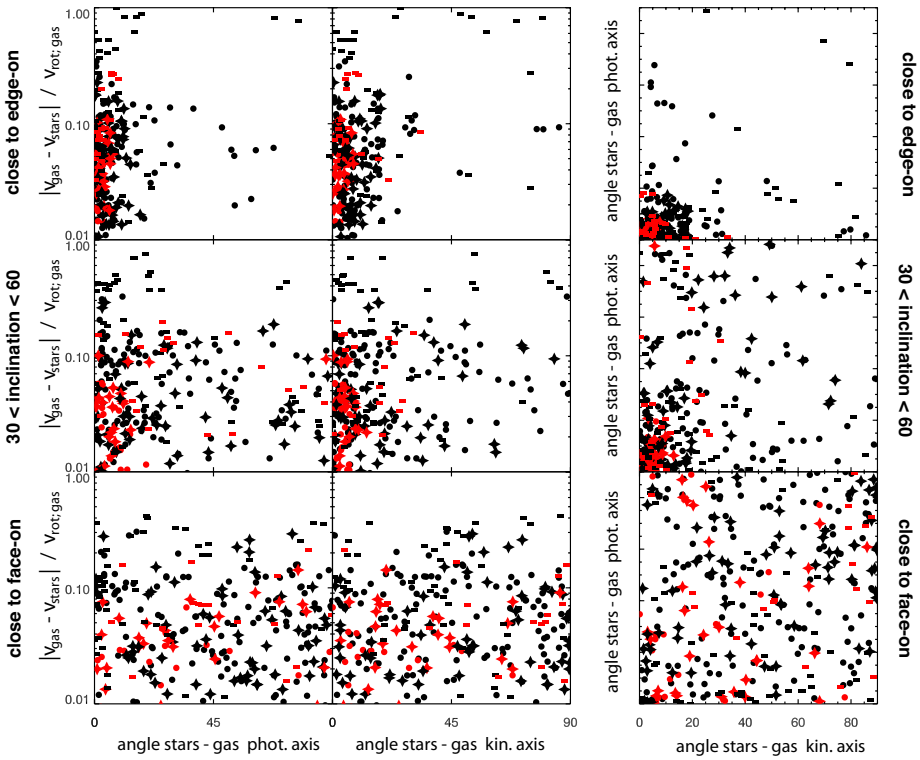

Figure 4.6 – Average velocity differences between the gas and the stellar disk normalized to the average observed rotational velocity of the gas, difference in position angle between the projected distributions of the gaseous and stellar disks, and between the projected stellar disk and the kinematic axis of the gas, for merger simulations (black) and for systems in isolation (red). The different rows correspond to different ranges of viewing angles. In this figure we have included the model-A dwarf with $M_\star = 1.4 \times 10^8\ M_\odot$ (solid circles), as well as values for systems with $M_\star = 4.4 \times 10^6\ M_\odot$ (dashes) and with $M_\star = 1.1 - 2.7 \times 10^7\ M_\odot$ (diamonds).

velocity defined as $\frac{1}{2}(|\max(v_{\rm proj})| + |\min(v_{\rm proj})|)$, where these stem from the projected gas velocities within the observed region.

- *Misalignment between stars and gas*
  A relatively straightforward measurement consists in comparing the orientation of the major axis of the surface brightness to that of the projected cold gas distribution. These are computed by fitting a 2D-gaussian to these projected distributions.

  Since measuring velocity fields for stars is challenging, in general it will not be possible to estimate the misalignment between the kinematic axes of stars and of gas. Therefore instead, we compare the orientation of the photometric major axis of the stars to the gas kinematic major axis which can easily determined observationally from HI velocity maps.

  The gas kinematic major axis is determined in our simulations using the line connecting the maximum and minimum velocities observed. To obtain an estimate of the uncertainty in the orientation we compute the kinematic axis 50 times, each time using two randomly chosen values amongst those ranked in the top 10% as maximum and minimum. From this random sampling we estimate an uncertainty of 9.8 degrees, for the merging systems (lower for isolated systems). However, this estimate depends strongly on the amplitude of the velocity field, e.g. for systems close to face on, the uncertainty can be as large as ~ 54 degrees.

Figure 4.6 presents the results for all our simulated systems. We have separated the analysis according to the projected inclination because this has a significant impact on the ability to separate isolated from merging systems.

For low mass systems (indicated by the dashes), we find the largest average velocity differences between stars and gas in mergers, while for all isolated systems, independently of their mass, $\Delta \lesssim 0.1 v_{\rm rot}$, and this appears to be relatively robust to inclination effects. Inspection of the simulations shows that the largest amplitude is reached around the time the satellite reaches the disk, i.e. around the first pericenter passages.

The velocity differences in our simulations are typically smaller (a few km/s) than those observed for XMP dwarfs by Filho et al. (2013)[1]. However, the normalised velocity differences are $0 \lesssim \Delta_{\rm HI}/w_{50} \lesssim 1$, and hence consistent with those in our simulations.

Comparison of the different rows in Figure 4.6 directly shows that the effects of inclination are important. Especially for nearly face-on systems, the separation between mergers and isolated dwarfs is not straightforward. This is entirely due to the large uncertainties in the determination of the orientation

[1] These authors disregard offsets smaller than 10 km/s because the uncertainties and their expectation that HI velocity dispersions are ~ 10 km/s for dwarf galaxies.

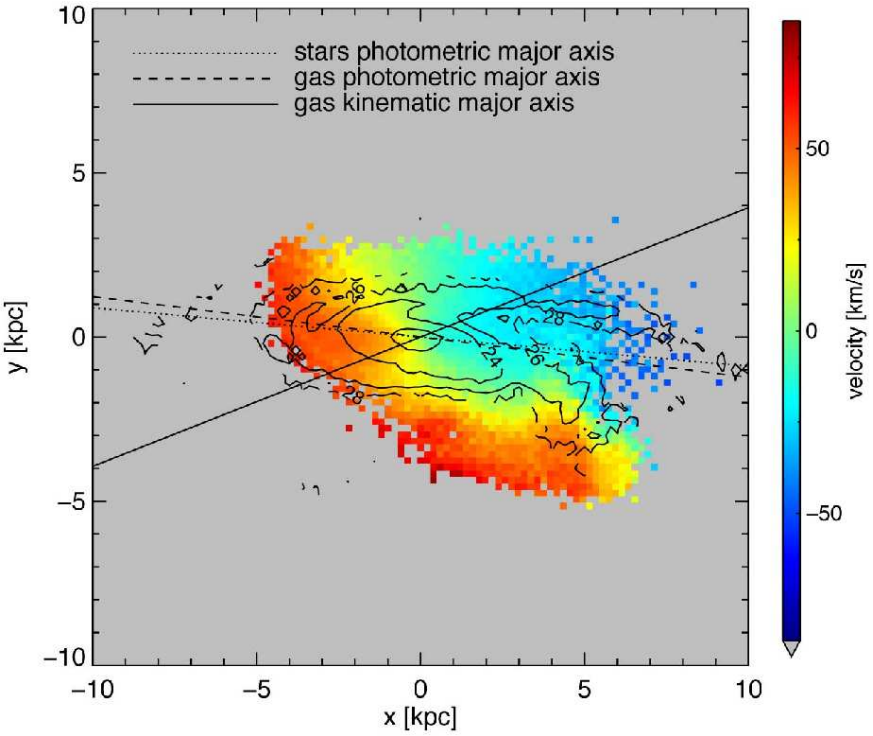

Figure 4.7 – The gas line-of-sight velocity field with the stellar surface brightness overplotted as contours for the model-A dwarf system during the minor merger shown in Fig. 4.1 at $t = 2$ Gyr, but now for an inclination angle of $i = 72.6$ degrees from face-on. The kinematic axis for the gas (solid line) and the major axis of the surface brightness distribution (dotted line) are misaligned. The fitted profiles to the stellar and gas (dashed line) distributions have similar orientations, and this is because they are dominated by the behaviour in the central regions.

of the photometric and kinematic axes. For example, isolated systems have close to circular spatial distributions, so that major and minor axes directions are hard to define. Furthermore, the line-of-sight velocities are typically small in this case and so also the rotation axis is not well constrained. This leads to more scatter in these distributions.

For other inclinations, the isolated systems tend to be clustered around small average velocity differences, and small misalignments. In other words, mergers are clearly more likely to have misaligned stellar photometric and gas photometric or kinematic major axes. The lack of correlation seen in the bottom left panel of Fig. 4.6 is a result of the misalignment between the photometric and kinematic axes for the gas in the case of mergers.

Fig. 4.7 provides a visual impression of a projection where the gas kinematic and the stellar distribution major axes are misaligned for the system from

Fig. 4.1 at 2 Gyr seen for an inclination of 72.6 degrees. The gas column density distribution and stellar surface brightness distribution have roughly the same orientation (the misalignment angle is ~ 2 degrees), but for both the orientation in the inner regions is different from that in the outer parts. The gas kinematic axis however has a significantly different major axis orientation, offset by ~ 28 degrees.

4.5 Some intriguing cases

So far we have focused on general trends followed by our morphological and kinematic indicators, and especially on the differences between isolated and merger systems to facilitate the observational identification of dwarf galaxies undergoing a merger when the secondary is not visible, in our case being a dark satellite. We now make a rough comparison to a few intriguing cases from the literature.

The system depicted in Fig. 4.1 shows a distribution of gas and stars that shares characteristics with the irregular dwarf galaxy IC10 (see also Fig. 1.4): a disturbed gas and stellar distribution with multiple star forming cores and an extended HI distribution with plums and spurs with velocities that differ from that of the main gas disk (see for example Ashley et al. 2014). On the other hand, the HII regions have a low metallicity (Garnett 1990) which has been suggested as being due to the influx of fresh pristine gas from the environment (Sánchez Almeida et al. 2014). However, another interpretation is possible since as we have seen the merger leads to an extended starburst that is fueled from gas that was originally present in the outskirts of the main system, and which presumably also had a lower metallicity (see also Chapter 3).

Another intriguing system, though for different reasons, is the dwarf irregular galaxy NGC6822. In addition to a disturbed gas and stellar distribution and a high rate of recent star formation, this system has a star formation core located very far from the center. This outer star forming region was proposed to indicate the location of a companion system, also due to a significant velocity offset (de Blok & Walter 2000), but this has been discarded because no older stellar population has been found at that location (Cannon et al. 2012). An interaction with a dark substructure will however display exactly this signature: a star formation region at a large distance without an underlying older population and a metallicity similar to the main system.

4.6 Conclusions

We have investigated the distribution of quantitative morphological and kinematic parameters (often used to characterize interacting, starburst, or peculiar systems), measured during a minor merger between a dwarf galaxy

and a dark satellite. For our system with $M_\star > 10^8\ M_\odot$ the very disturbed morphologies for the gas and stellar distributions induced by the merger are reflected most notably in asymmetry parameters during the merger itself. A post-merger system however stands out the most in its high values for concentration related parameters, such as C, M_{20} and the Gini coefficient. This is the result of an increase in central stellar and gas density due to gas being driven toward the center by tidal torques and causing a nuclear starburst episode, which can last several Gyrs.

Kinematic based parameters can be used to identify merger systems, for example via the large differences between average projected gas and stellar velocities. This works particularly well for smaller mass systems ($M_\star < 2 \times 10^7\ M_\odot$), for which the morphological indicators fail. Misalignments between the gas kinematic major axis and the stellar surface brightness major axis are also useful, but can only be applied for systems that are far from face-on.

Although we still have to determine the smoking-gun that will allow to determine that an interaction between a dwarf galaxy and a dark satellite has taken place, in our simulations star forming cores located far from the center actually seem to pinpoint the location of the satellite. This could be the way to shed light on a missing satellite.

Acknowledgements. We are grateful to Claudio Dalla Vecchia, Joop Schaye, Carlos Vera-Ciro, Alvaro Villalobos and Volker Springel for providing code. AH acknowledges financial support from the European Research Council under ERC-StG grant GALACTICA-240271 and the Netherlands Research Organisation NWO for a Vici grant.

5

On the rate of minor mergers of dwarf galaxies and dark satellites in ΛCDM

— Paper in preparation, T. K. Starkenburg, A. Helmi, et al. —

Abstract

Within hierarchical structure formation models, mergers are known to play an important role and to cause large changes in galaxies, including morphological transformations or starburst episodes. On the scale of low mass galaxies, interesting new types of interactions are possible. Dwarf galaxies are expected not only to experience significant mergers with other galaxies, but likely also with halos devoid of stars. To estimate the importance of mergers with dark satellites on the recent lives of dwarf galaxies we have coupled a semi-analytic galaxy formation model to a large cosmological N-body simulation. This allows us to trace the merger histories of a sample dwarf galaxies with present-day virial masses in the range $10^8 - 10^{10} M_\odot$. We have found that roughly 27% of these dwarfs have experienced at least a 20% virial mass ratio merger since $z \sim 2$, and 11% since $z \sim 0.5$. For a system with $M_{\rm vir} \sim 10^{9.5}\ M_\odot$ (comparable in mass to the Fornax dwarf spheroidal galaxy), the probability that it has experienced such a merger in the last 2 Gyr, and hence whose consequences might still be observable, is 4%. We also find that dark satellites are generally much more massive that the stellar components of the dwarf galaxies at the time of infall, and that in a small fraction of the cases already have their first pericentric passage close to the stellar disk. Their influence on the evolution of dwarf galaxies should therefore not be neglected.

5.1 Introduction

The formation of structure in our Universe is thought to come about in a hierarchical fashion: with the highest density peaks collapsing first and growing by the gravitational accumulation of more and more matter (Peebles 1982; Blumenthal et al. 1984; Davis et al. 1985; Fakhouri & Ma 2008; Neistein & Dekel 2008; Cole et al. 2008). Within matter overdensities galaxies grow as a result of gas inflow, accretion of satellites, and major and minor mergers. Much work has been done to characterize the effects these mergers have on galaxies, to trace their morphological transformation and thereby connect evolution to the observed diversity in galaxy morphology (e.g. Toomre & Toomre 1972; Toomre 1977; Barnes 1988; Hernquist 1989; Barnes & Hernquist 1992; Di Matteo et al. 2007, 2008; Cox et al. 2008; Bournaud 2011).

The observed properties of galaxies can be used to constrain the importance of the various processes involved in galaxy evolution. For example the existence of thin disk and bulge-less galaxies is often assumed to be indicative of a (recent) quiet merger history (Toth & Ostriker 1992; Walker et al. 1996; Wyse 2001; Kormendy & Fisher 2005; Kautsch et al. 2006; Stewart et al. 2008, 2009; Hopkins et al. 2009). On the other hand, a significant fraction of starbursting systems and irregular or peculiar galaxies (see for example Arp's Atlas of peculiar galaxies, Arp 1966) are thought to be in or to have recently experienced a merger or a tidal interaction (e.g. Ellison et al. 2011; Willett et al. 2015; Kaviraj 2014a,b; Paudel et al. 2015).

In this context a very relevant prediction from current large cosmological simulations is the expected merger fraction of galaxies. Fakhouri & Ma (2008); Fakhouri et al. (2010) describe the merger fraction of halos over a range of present day masses, merger mass ratios, and redshifts, and the dependence on these three quantities. They find that the mean merger rate per halo is nearly independent of the descendant mass (the mass of the halo in question at $z = 0$), and that the merger rate is nearly independent of redshift when calculated per redshift unit (Fakhouri et al. 2010 see also Berrier et al. 2006; Genel et al. 2009). On the other hand, Gottlöber et al. (2001) argue that the merger rate depends on the environment of the halos, with higher rates in the field than in groups than in clusters.

Less attention has been paid to the effect of mergers on low mass galaxies. Observationally starbusts and irregular features and kinematics have been reported in the literature (Taylor et al. 1995; Gil de Paz et al. 2003; Ekta & Chengalur 2010; López-Sánchez 2010; Holwerda et al. 2013; Lelli et al. 2014b; Knapen & Cisternas 2015), although the link to a merger is less clear (Brosch et al. 2004; Ekta & Chengalur 2010; López-Sánchez 2010; Lelli et al. 2014b; Paudel et al. 2015) and other explanations for such peculiarities have been suggested (e.g. Verbeke et al. 2014; Meurer et al. 1998; van Zee et al. 2001; Lelli et al. 2014a; Elmegreen et al. 2012; Bekki & Freeman 2002). Theoretically,

mergers between dwarf galaxies have mostly gained attention in the context of the Local Group (e.g., Yozin & Bekki 2012; Kazantzidis et al. 2011; Łokas et al. 2014; Angulo et al. 2009; Klimentowski et al. 2010; Ashley et al. 2013; Deason et al. 2014; Amorisco et al. 2014; Łokas et al. 2014).

Dwarf galaxies are known to be very inefficient at forming stars (Blanton et al. 2001; Robertson & Kravtsov 2008), and to have very low baryon fractions (Gnedin 2000; Hoeft et al. 2006; Crain et al. 2007). This results in a halo mass–stellar mass relation that drops sharply toward lower masses (Guo et al. 2010; Behroozi et al. 2013a; Moster et al. 2013; Kormendy & Freeman 2016; Garrison-Kimmel et al. 2014; Sawala et al. 2015). Moreover, while small dark matter halos are abundant, they are predicted to be strongly affected by reionization, photo-evaporation, and/or supernova feedback (for $M_{\rm vir} \lesssim 10^9 M_\odot$), (Gnedin 2000; Hoeft et al. 2006; Kaufmann et al. 2007; Okamoto et al. 2008; Gnedin et al. 2009; Li et al. 2010; Sawala et al. 2013; but see also Taylor & Webster 2005; Warren et al. 2007). As a consequence, dwarf galaxies experiencing a merger will be more vulnerable to tidal effects and the satellites of dwarf galaxies will be predominantly dark (Helmi et al. 2012).

In fact, in Chapter 2, and Chapter 3 we have studied the possibly life-changing event that a minor merger with a dark satellite can be for a dwarf galaxy. As described in those Chapters, such events can lead to drastic changes in the morphology, structure, kinematics, and star-formation history of a low mass galaxy. In Chapter 4 we identified a set of observables and quantitative indicators that could be used to establish if dwarf galaxies are experiencing such encounters. Given their tentatively dramatic impact on the evolution of dwarf systems, it is important to establish the likelihood of such events, i.e. to quantify the expected rate of occurrence of minor mergers between low mass galaxies and dark satellites.

Based on the Aquarius simulations of six Local Group-like environments (Springel et al. 2008), Helmi et al. (2012) have estimated that a dwarf galaxy with a galaxy efficiency of $\eta_{\rm gal} = M_\star/(M_{\rm vir} f_{\rm bar}) \sim 5\%$, where $f_{\rm bar} = 0.17$, the cosmic baryon fraction, experiences on average 1.5 encounters with a satellite that at first pericenter is at least as massive as the dwarf's stellar disk. In this Chapter we extend this analysis to much larger scales, larger mass ranges in centrals and satellites, and a larger variety of galaxy environments. We will not just trace the merger fraction for dark matter halos, but estimate this for dwarf galaxies merging with *dark* satellites for different redshift ranges and lookback times.

To this end, we combine the cosmological N-body simulation Millennium-II (Boylan-Kolchin et al. 2009) with a semi-analytic model of galaxy formation and explore the merger histories of a sample of dwarf galaxies in the original simulation, and in two scaled down versions. The advantage of the scaled versions is that they allow us to follow the dynamics of lower mass substructures, i.e. originally below the resolution limit of Millennium-II. On the other

hand, particularly for the scale we are interested in, the semi-analytic galaxy formation model is needed to identify which low mass halos have stars and which have remained dark.

This Chapter is organized as follows. In Sect. 5.2 we shortly describe the Millennium-II simulation, the scaling toward lower masses, and the semi-analytic code. We also describe in this section some properties of galaxies with emphasis on the selected sample of dwarfs. In Sect. 5.3, we trace their merger histories, particularly with dark infalling satellites, and compute the merger fractions. We also explore some of the properties of the mergers and their environment. Lastly, we discuss our results in Sect. 5.4 and present our conclusions in Sect. 5.5.

5.2 Method

We apply the semi-analytic modeling code from Starkenburg et al. (2013) (see also Li et al. 2010), to the large cosmological N-body simulation Millennium-II (Boylan-Kolchin et al. 2009). We will here give a short description of the N-body simulations, the post-processing, and the semi-analytic model, while more details can be found in the respective papers.

5.2.1 Millennium-II

Millennium-II is a large cosmological N-body simulation run using a version of the GADGET Tree-PM code (lastly described in Springel 2005; Springel et al. 2001b). It models the formation of structure following 2160^3 particles in a comoving box of side length $L = 100\ h^{-1}\mathrm{Mpc}^3$ with a particle mass of $6.885 \times 10^6\ h^{-1} M_\odot$ and a Plummer-equivalent force softening of $1\ h^{-1}\mathrm{kpc}$. The mass resolution means that a halo corresponding to a Milky Way-like galaxy will have $\sim 10^5$ particles and the halo of a dwarf galaxy of $M_{\mathrm{halo}} = 2 \times 10^8\ M_\odot$ will be just above the resolution limit of 20 particles. The concordance cosmology assumed is described by $\Omega_{\mathrm{tot}} = 1.0$, $\Omega_{\mathrm{m}} = 0.25$, $\Omega_{\mathrm{b}} = 0.045$, $\Omega_\Lambda = 0.75$, $h = 0.73\ \mathrm{km/s/Mpc}$, $\sigma_8 = 0.9$, and an initial power law index of $n_s = 1$. The Millennium-II simulation has 8 outputs at very high redshifts and 60 between $z \sim 20$ and $z = 0$, spaced in approximately equal logarithmic redshift bins. For all results presented in this paper we focus on the evolution at $z \leq 2$.

The N-body simulation is post-processed to identify and compute the properties of dark matter halos, gravitationally self-bound subhalos, and to construct merger trees. At each snapshot Friends-Of-Friends dark matter halos are identified using a FOF group-finder (Davis et al. 1985) with a linking length of 20% of the mean interparticle separation. Self-bound halo substructure is subsequently identified using the SUBFIND algorithm (Springel et al. 2001a) which finds local density maxima in the FOF-halos and performs an unbinding

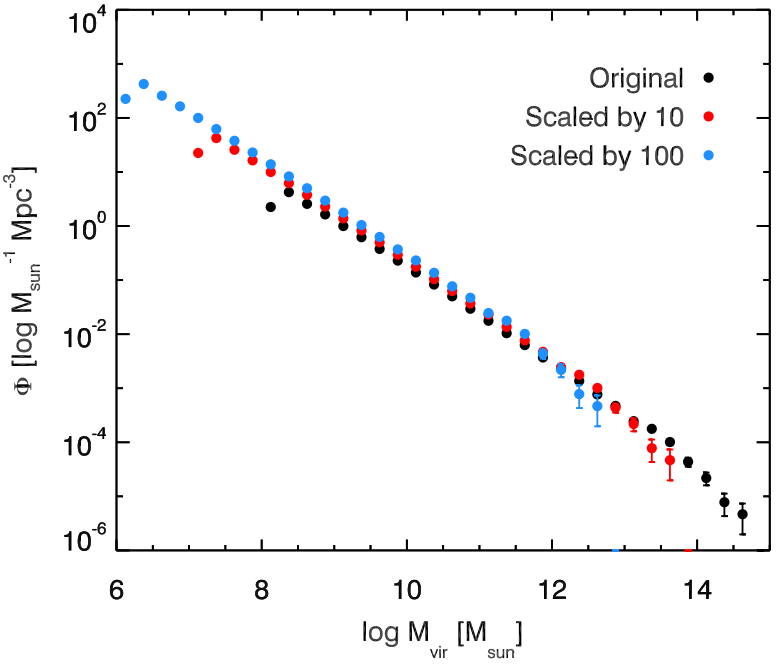

Figure 5.1 – The virial mass function of central subhalos at $z = 0$ for the original Millennium-II simulation (black), mass-scaled by a factor 10 (red), and mass-scaled by a factor 100 (blue). Note that this plot shows the mass function of the individual subhalos that are the central halos in their FOF-group, and not the mass function of the FOF-halos themselves.

procedure to determine which particles of the FOF-halo are bound to the individual density peaks. All self-bound structures with at least 20 particles are classified as subhalos. With these subhalos merger trees are constructed constrained by the requirement that each subhalo has at most one descendant. This descendant is the subhalo in snapshot S_{n+1} that has the most particles of the subhalo at snapshot S_n weighted by particle rank based on the binding energy of the particles. Progenitor-descendant connections can occasionally skip a snapshot if a subhalo passes through a high density region and is therefore not found by SUBFIND then. Based on these progenitor-descendant connections merger trees are costructed through all snapshots, for each halo containing pointers, if present, to its progenitor, descendant, next most massive progenitor of its descendant, the dominant subhalo in its FOF group, and the next most massive subhalo in its FOF group (Boylan-Kolchin et al. 2009).

To detect mergers experienced by dwarf galaxies we scale the Millennium-II simulation down by a factor 10 and a factor 100 in mass. This means that in the rescaled versions we reach mass resolutions of $6.885 \times 10^5\ h^{-1} M_\odot$ and $6.885 \times 10^4\ h^{-1} M_\odot$ which resolves dark matter halos down to $M_{\rm halo} = 2 \times 10^7\ M_\odot$ and $M_{\rm halo} = 2 \times 10^6\ M_\odot$, respectively. Naturally, we correspondingly also scale positions and velocities by the same factor, namely $10^{1/3}$ in the first case, and by $100^{1/3}$ in the second case.

Throughout this paper a virial mass $M_{\rm vir}$ denotes $M_{\rm 200crit}$, i.e. the mass within the radius where the mean density of a halo is 200 times the critical density of the universe at that redshift. We mainly use this mass for selecting galaxies and halos within a specified range at redshift $z = 0$. $M_{\rm vir}$ is well defined only for galaxies that are the central (i.e. most massive or dominant) halo within their FOF-halo. $M_{\rm halo}$ denotes the total mass of all the particles gravitationally bound to a subhalo, and M_z denotes $M_{\rm halo}$ at $z > 0$, usually used in the context of this Chapter at the snapshot before merging.

Figure 5.1 shows the halo mass function at $z = 0$ for the original Millennium-II simulation (in black) and for both scaled versions (red and blue, by factors 10 and 100 respectively). The scaled versions agree very well with the original Millennium-II within the range where they overlap, except for the very first and last mass bins. On the high mass end incompleteness and limited volume affect progressively the counts in the scaled versions. On the low mass end the resolution is the driver of the differences. Figure 5.1 clearly shows that by combining results from the original simulation (black), a version scaled down in mass by a factor 10 (red), and one scaled down by a factor 100 (blue), we have extended the well-resolved halos towards masses slightly above $M_{\rm vir} = 10^6\ M_\odot$.

5.2.2 The semi-analytical model

The galaxy formation model we use is a modified version of the Munich semi-analytic model that has been shown to work well for the satellites in the Local Group (Starkenburg et al. 2013). A slightly different version of the model ran on the Millennium-II simulation is described in Guo et al. (2011).

The merger trees and subhalo properties obtained from the N-body simulation are used in the semi-analytic model to follow the evolution of the galaxies that reside in the halos. The model is based on a set of simple but astrophysically and/or observationally motivated "prescriptions" which take into account the relevant baryonic physical processes for galaxy formation and evolution. This results in a model that is fast and can compute the properties and evolution of all galaxies in a large cosmological simulation, but does not explicitly follow their dynamics and by itself does not provide spatial information.

The semi-analytic model we use was first introduced in Kauffmann et al. (1999), was further expanded, updated, modified, and described in Springel

et al. (2001a); De Lucia et al. (2004); Croton et al. (2006); De Lucia & Blaizot (2007); De Lucia & Helmi (2008); Li et al. (2009, 2010), and lastly in Starkenburg et al. (2013). In particular, the version we apply uses the "ejection" feedback scheme introduced in De Lucia et al. (2004). In comparison, the feedback schemes of Croton et al. (2006); De Lucia & Blaizot (2007) significantly over-predict the number of galaxies with stellar mass between 10^7 and 10^{10} $M_\odot$ (Guo et al. 2011). On the other hand, the feedback scheme from De Lucia et al. (2004) results in more extended star formation histories and higher efficiencies in transforming gas into stars, which therefore results in higher luminosities for massive galaxies: up to 0.8 mag brighter than observed for the brightest cluster galaxies (De Lucia & Blaizot 2007). The model we use also employs a slightly earlier reionization epoch and additional suppression of cooling in small halos ($T_{\rm vir} < 10^4$ K) motivated by improved modeling for the low mass galaxies. Below we shortly describe the basic processes in the model.

Reionization is modeled following Gnedin (2000) and Croton et al. (2006). It lasts from $z = 15$ to $z = 11.5$, and causes a decrease in baryonic content for all halos equal or below a redshift-dependent so-called filtering mass. The hot gas in halos can cool depending on the metallicity and temperature of the gas. This is however forbidden below the atomic hydrogen cooling limit $T_{\rm vir} = 10^4$ K under the assumption that in most cases any molecular hydrogen undergoes photodissociation by UV radiation from the (first) stars. Cold gas is assumed to be in an exponential thin disk with properties based on the formalism of Mo et al. (1998). This cold gas can form stars when above a critical surface density threshold $\Sigma_{\rm crit} = 0.59 V_{200}/r_{\rm SF,disk}$, assuming a star-forming disk radius $r_{\rm SF,disk} = 3R_d$ (where R_d denotes the disk scale radius), a flat rotation curve for the gas disk with $V_{\rm rot} = V_{200}$, and a fixed gas velocity dispersion of 6 km/s (Kennicutt 1989). The star formation rate is proportional to the amount of gas above the threshold. During major mergers star formation can happen in bursts when (a part of the total amount of) cold gas is transformed into stars. The model assumes a Chabrier (Chabrier 2003) initial mass function, and assumes instantaneous recycling from Type II supernovae ejecta. This implies that 43% of the mass in stars formed is (instantaneously) recycled back into the (cold) gas phase together with an equal fraction of metals formed in these Type II SNe events. In general metals follow the mass flow between the different baryonic components. Gas ejection induced by supernovae is dependent on the mass of the halo ($\propto 1/V_{200}^2$). The ejected gas by supernovae feedback is put in a separate component that can later be reincorporated in the hot gas component.

If a galaxy becomes a satellite the hot gas and ejected gas components are assumed to be stripped instantaneously and are added to the new host. Starkenburg et al. (2013) further introduce stellar stripping and tidal disruption prescriptions for satellite galaxies, but we do not apply those prescriptions in our runs because our focus is on the lowest mass field (isolated) galaxies.

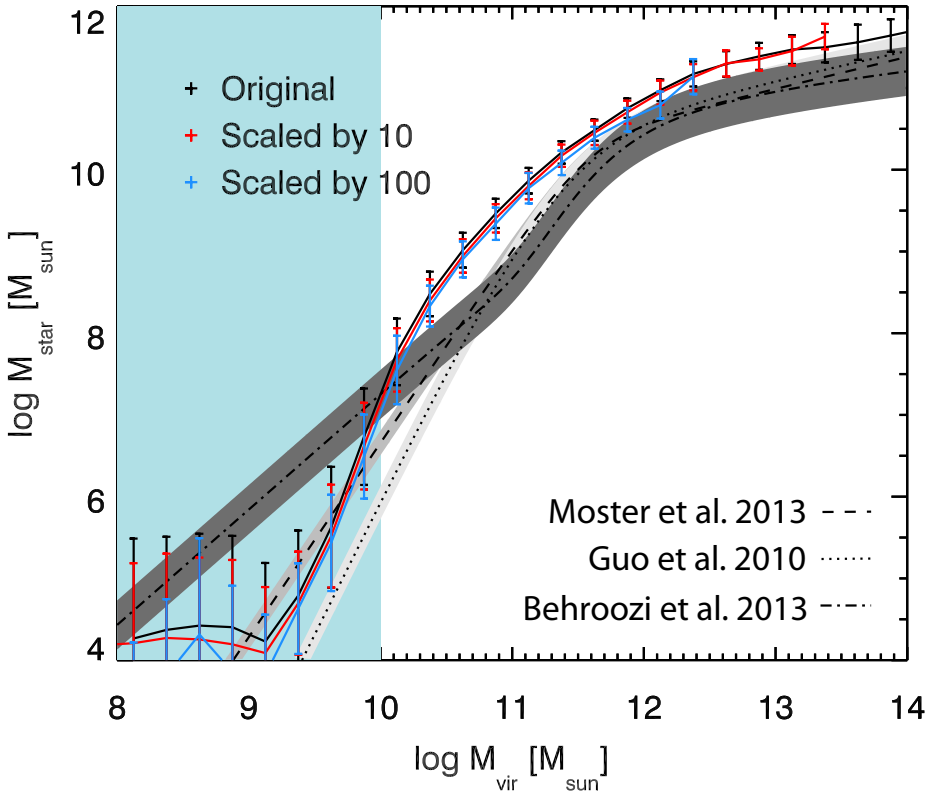

Figure 5.2 – The halo mass–stellar mass function, defined as the median of the stellar mass and halo mass ($M_{\rm vir}$) for the galaxies of central subhalos at $z = 0$ for the original Millennium-II simulation (black), mass-scaled by a factor 10 (red), and mass-scaled by a factor 100 (blue) with the location of the selected galaxies highlighted (light-blue shaded area). Overplotted are three halo mass–stellar mass relations: from Guo et al. (2010): dotted line with the light grey area denoting $\sigma = 0.2$ dex, from Moster et al. (2013): dashed line, with the grey shaded area denoting $\sigma = 0.15$ dex, and from Behroozi et al. (2013a): dot-dashed line with the dark grey shaded area denoting $\sigma = 0.3$ dex.

5.2.3 Some properties of the galaxies in the model

We apply the semi-analytic model described above to the Millennium-II simulation, and to this same simulation rescaled by a factor of 10 and a factor of 100, with the goal of exploring mergers on the scale of dwarf galaxies, especially with dark satellites. It is important to realize that because of this scaling-down, galaxies at a fixed mass could reside in quite different environments in each of the simulations "versions"; the massive clusters in the Millennium-II will now be large groups or small clusters, and a group like

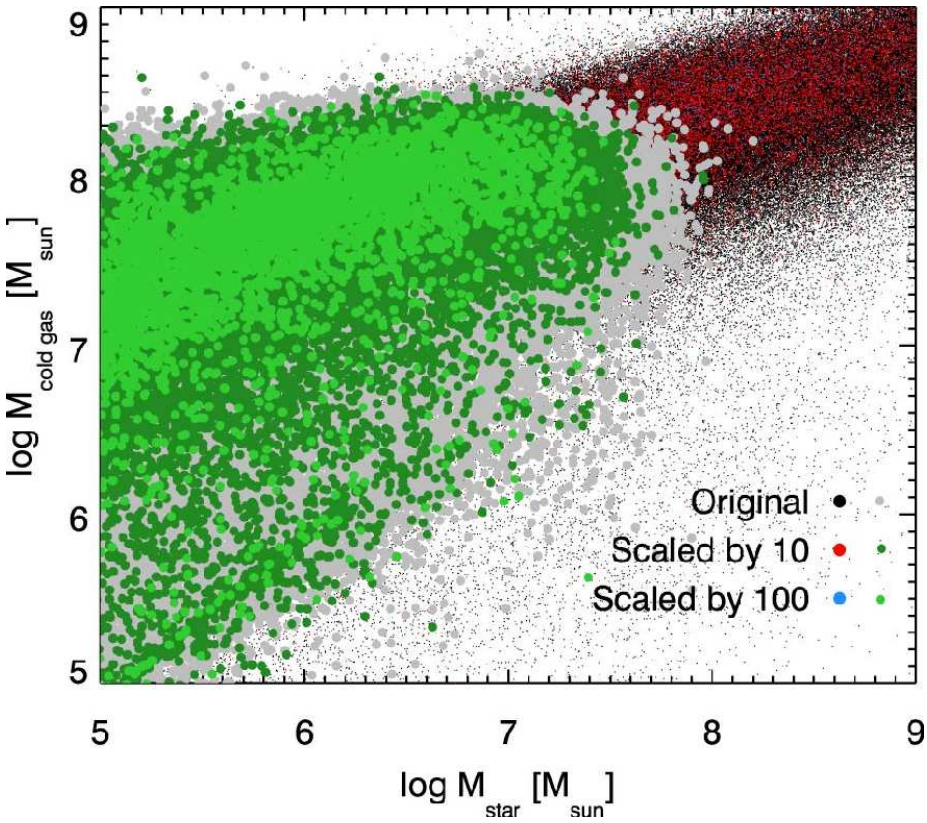

Figure 5.3 – The stellar mass and cold gas mass for isolated galaxies at $z = 0$ in the original Millennium-II (black), the version scaled by 10 (red), and the version scaled by 100 (blue), with our selection of galaxies ($10^8 M_\odot < M_{\rm vir} < 10^{10} M_\odot$, $M_\star > 0$ and the central halo in their tree) highlighted for all three versions (original: grey, scaled by 10: dark green, scaled by 100: light green).

the Local Group will be a small group of dwarf galaxies if scaled in mass by a factor of 100.

Since our focus is on the dwarf galaxy scale, we will not discuss the general properties of the galaxy population. As mentioned earlier, the model is known to have shortcomings for massive systems, where galaxies tend to be brighter than estimated observationally for a given halo mass.

This is also apparent from Figure 5.2 where we show the halo mass–stellar mass function for central galaxies at $z = 0$, for all simulations "versions". Note that all three versions agree well over the range where they overlap. Overplotted in Fig. 5.2 are three halo mass–stellar mass relations with their quoted uncertainties: derived by Behroozi et al. (2013a) (dot-dashed), Moster

et al. (2013) (dashed), and a theoretical prediction from Guo et al. (2010) (dotted). Note how our semi-analytic model appears to overpredict the stellar mass for fixed halo mass for a large range in halo masses, especially for $M_{\rm vir} \gtrsim 10^{10.5}\ M_\odot$ where the empirical relations are best calibrated. For lower masses these empirical relations are largely extrapolations, what explains their great variety. In this regime, the SA model we use depicts good agreement with the results of hydrodynamical simulations (see e.g. Fig. 14 of Starkenburg et al. 2013). It is also here where e.g. Yaryura et al. (2016) argue that the model galaxies are embedded in the right dark matter halos from a comparison to the HI velocity function. This is in fact the shaded region (light blue) where we select the dwarf galaxies that are the focus of our work, i.e. those with virial mass in the range of $10^8\ M_\odot \leq M_{\rm vir} \leq 10^{10}\ M_\odot$.

Figure 5.2 shows that there are a small number of halos with virial masses below $M_{\rm vir} \sim 10^9\ M_\odot$ that do have stars. These are all halos that are isolated. A subset, however, consists of central halos at $z = 0$ that were subhalos in their past. Those are not considered further in our analysis as they do not correspond to the central halos within their halo trees.

The relation between the cold gas mass and stellar mass of isolated galaxies with $10^5 M_\odot \leq M_\star \leq 10^9 M_\odot$ at $z = 0$ is shown in Fig. 5.3. Irrespective of the large scatter there is the expected general correlation, although the scatter is significant, of the order of 1–2 dex in cold gas mass and 1–3 dex in stellar mass especially at the low mass end. This is particularly apparent from the distribution of solid circles, which corresponds to the objects of interest, i.e. those selected by virial mass ($10^8\ M_\odot \leq M_{\rm vir} \leq 10^{10}\ M_\odot$; blue shaded area in Fig. 5.2). Note that these objects are typically also rather gas-rich, with more baryons in the form of cold gas than in stars.

5.3 Results

5.3.1 Dwarf and dark galaxies in the scaled simulations

As we are mainly interested in the low mass halos, and which of those contain a dwarf galaxy and which stay dark, we show in Fig. 5.4 the fraction of dark objects as a function of halo mass[1] in the regime of interest. The fractions of dark objects and the mass at which the transition from mostly dark to mostly bright objects occurs agrees very well amongst the three simulation runs. For central galaxies 50% of the objects are bright, and 50% remains dark[2], around $M_{\rm vir} \sim 10^{9.4}\ M_\odot$, while for satellites this happens at $M_{\rm vir} \sim 10^{9.0}\ M_\odot$.

For the purpose of this Chapter, we are mostly interested in the dwarf galaxies that are isolated, i.e. they are not a satellite of a bigger galaxy. Therefore, we select dwarf galaxies that are the main galaxies within their

[1] For centrals (type0) the mass is $M_{\rm vir}$, while for satellites (typeI) the mass measured is $M_{\rm halo}$.
[2] We count as dark also objects with $M_{\rm star} = 0$ but $M_{\rm gas} \neq 0$.

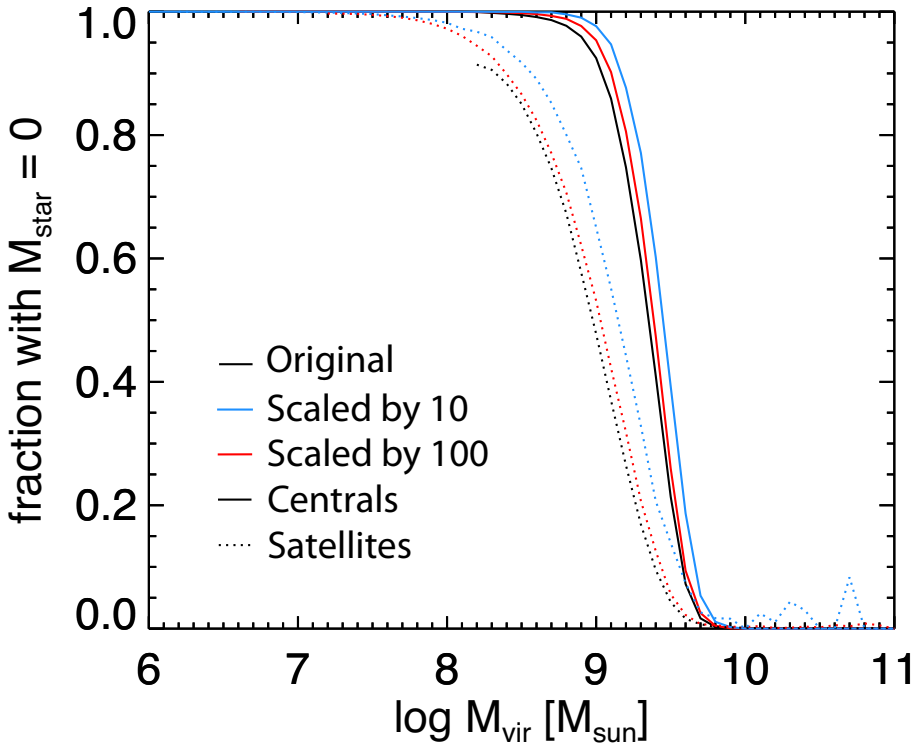

Figure 5.4 – The fraction of dark galaxies ($M_\star = 0$) as a function of $M_{\rm vir}$ for galaxies from the semi-analytic run on the original Millennium-II simulation (black), a version mass-scaled by a factor 10 (red), and a version mass-scaled by a factor 100 (blue).

merger tree and have a virial mass in the above-mentioned range and with a stellar mass $M_\star > 0$. For the merger trees of these systems we trace the subhalos falling into the main branch that were themselves isolated halos before infall, up to $z \sim 2$, and explore the statistical properties of this set.

In general every halo experiences a large number of mergers but the infalling subhalos are mostly of very low mass. We focus on secondaries that are larger than 5%, 20% or 40% of the main halo mass at infall. We define the mass ratio as the ratio of the number of particles gravitationally bound to the satellite and to the host halo in the snapshot before the secondary becomes a satellite. In Chapter 2 and Chapter 3 (Starkenburg & Helmi 2015; Starkenburg et al. 2016, respectively) we show that such objects can exert a significant perturbation on the main dwarf galaxy when the subhalos have pericenter passages close to the stellar disk. We will take a closer look at the expected pericenters for the systems in our sample in Sect. 5.3.3.

5.3.2 Merger rates

For our set of dwarf galaxies we compute the fraction that experience a merger between redshifts $z = 2$ and $z = 0$. We count events for which the last snapshot before infall is within this range (i.e. the accreted objects are not necessarily fully disrupted by the present day). We consider only hosts with > 100 particles, and satellites with a minimum of 20 particles.

The fraction of systems experiencing a merger with a single (i.e. not part of a group) infalling satellite will vary depending on whether we consider all hosts, or only those with stars at all times (and not just at $z = 0$). For example if we count all satellites that fall onto, and later merge with, the main branch of the tree (defined as that with the largest number of halo particles at each snapshot) in the simulation with the highest mass resolution (i.e. that scaled by 100), we find that 66% of the hosts within our selection criteria have experienced at least one merger with mass ratio $m/M_z \geq 0.05$ since $z = 2$. For a merger mass ratio of $m/M_z \geq 0.2$ this drops to 43% and for a mass ratio of $m/M_z \geq 0.4$, it is 27%. Almost all of the infalling satellites are dark. For this definition of a merger, of the 5099 selected hosts in this simulation only two have no merger at all above the resolution limit imposed. For the "lower resolution" versions the number of infalling satellites is smaller, and the number of halos without any mergers below a given threshold is naturally higher.

However, as we are interested in the merger fractions for dwarf galaxies, we also provide a different estimate. This estimate of the merger fraction is obtained by defining the main stellar branch of the tree as the branch that follows the most massive progenitors that contain stars. Furthermore we require that the infalling subhalos are star-less or dark. If we then compute the fraction of present-day dwarf galaxies that have experienced at least one merger with a dark satellite since $z = 2$ the estimate drops slightly, to 60% for $m/M_z \geq 0.05$, 27% for $m/M_z \geq 0.2$, and 14% for $m/M_z \geq 0.4$. This is partly because even though we follow the stellar main branch, some of the selected dwarf galaxies at $z = 0$ do not have stars at higher redshifts. Furthermore for a significant number of those that do, the stellar component is not in the most massive halos that are defined to be the main branch but in infalling halos. A complex, often stochastic, star formation history is expected at this low mass end where within a narrow range of virial masses, some halos will be able to form stars but others will not. Note that if a satellite containing stars falls onto a host halo that is still dark we consider this as a dark-light merger as well, and the main halo will contain this stellar mass when the infalling system is dissolved. However, overall the fraction of dark satellites is overwhelmingly dominant within the population of infalling satellites.

Figure 5.5 shows the distribution of present day virial mass for the selected dwarf galaxies that have experienced a merger above a given mass ratio, where the number of mergers is obtained through the second estimate (following the

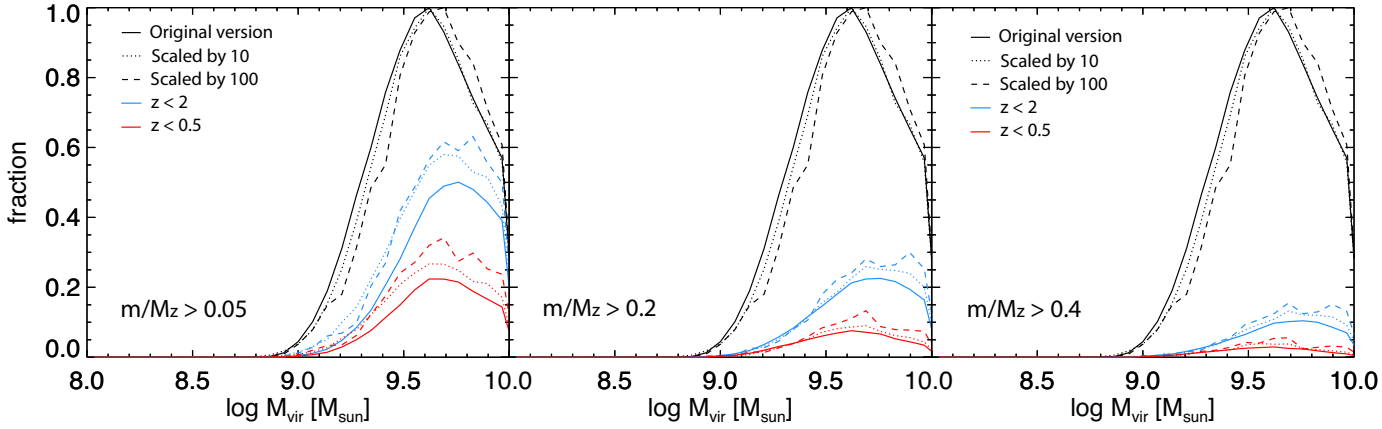

Figure 5.5 – The distribution of virial mass for the complete sample of dwarf galaxies (black) in the original simulation (solid), scaled by 10 (dotted), and scaled by 100 (dashed), and the ones with at least one merger with a dark secondary with merger mass ratio $m/M_z \geq 0.05$ (left panel), $m/M_z \geq 0.2$ (middle panel), and $m/M_z \geq 0.4$ (right panel) for $0 < z < 2$ (blue), and for $0 < z < 0.5$ (red). For the lowest merger mass ratio ($m/M_z \geq 0.05$) there is a significant difference due to resolution effects: 43% of the selected halos in the original version experience a merger for $z < 2$ and 20% for $z < 0.5$, while for the version scaled by 100 there fractions are 60% and 31%.

stellar main branch). In black we show the virial mass function of the selected dwarf galaxies, while the red curves correspond to the distribution for the systems that have experienced a merger for $z < 2$, and the blue curves to those for $z < 0.5$. The different linestyles depict the estimates obtained by using the different simulation "versions", and as the figure shows, they agree very well with each other. Most of the difference in the distributions, really only apparent when considering the lowest merger mass ratios, is due to resolution effects: either to the main halos dropping below the limit of 100 particles, and/or the satellites dropping below the subhalo resolution limit of 20 particles. For Fornax-like host galaxies (with $M_{\rm vir} \sim 10^{9.5}\ M_{\odot}$) approximately 50%, 20%, and 10% will have experienced a merger with mass ratio $m/M_z > 0.05$, $m/M_z > 0.2$, and $m/M_z > 0.4$, respectively since $z = 2$. For $z < 0.5$ these values are $\sim 30\%$ for $m/M_z > 0.05$, $\sim 10\%$ for $m/M_z > 0.2$, and $\sim 5\%$ for $m/M_z > 0.4$.

Figure 5.6 shows the expected fraction of dwarf galaxies having experienced a merger within a fixed lookback time. For these numbers we have combined the mergers found in all three versions of the simulation. Clearly mergers involving higher mass ratios are less common. In agreement with results for other N-body simulations the merger fraction increases slowly toward higher virial masses (see also Stewart et al. 2008), as shown by the left hand-side panels. For a galaxy of $M_{\rm vir} \sim 10^{9.5}\ M_{\odot}$ the fraction having experienced a merger within the last 2 Gyr is ~ 0.11, ~ 0.04, and ~ 0.02 for the different mass ratios considered.

The panels on the right of Figure 5.6 show the same expected fraction but now as function of the present day stellar mass of the dwarf (as predicted by the semi-analytic model, and which has thus far neglected the effect of the type of mergers we discuss now). We see that for low stellar masses the fraction appears to be relatively flat, while at high masses there appears to be a bump. This behavior may be understood in part because halos of a given virial mass can host galaxies with a large range of stellar masses (leading as it were to a redistribution of the merger fractions shown in the left panels). The fall-off at the high mass end is likely a reflection of the drop in the number of selected galaxies at the upper limit of the virial mass, $M_{\rm vir} \leq 10^{10}\ M_{\odot}$ also seen in Fig. 5.5 .

5.3.3 Properties of the most significant mergers

Mass ratios with respect to the stellar component

As a result of the low fraction of baryonic mass in low mass halos the stellar component of dwarf galaxies can be extremely small. In a merger event the mass ratio of the secondary halo to the stellar mass (or disk mass) of the primary halo can thus be very large. If the secondary has pericentric passages close in, a minor merger event will actually have the characteristics of a major

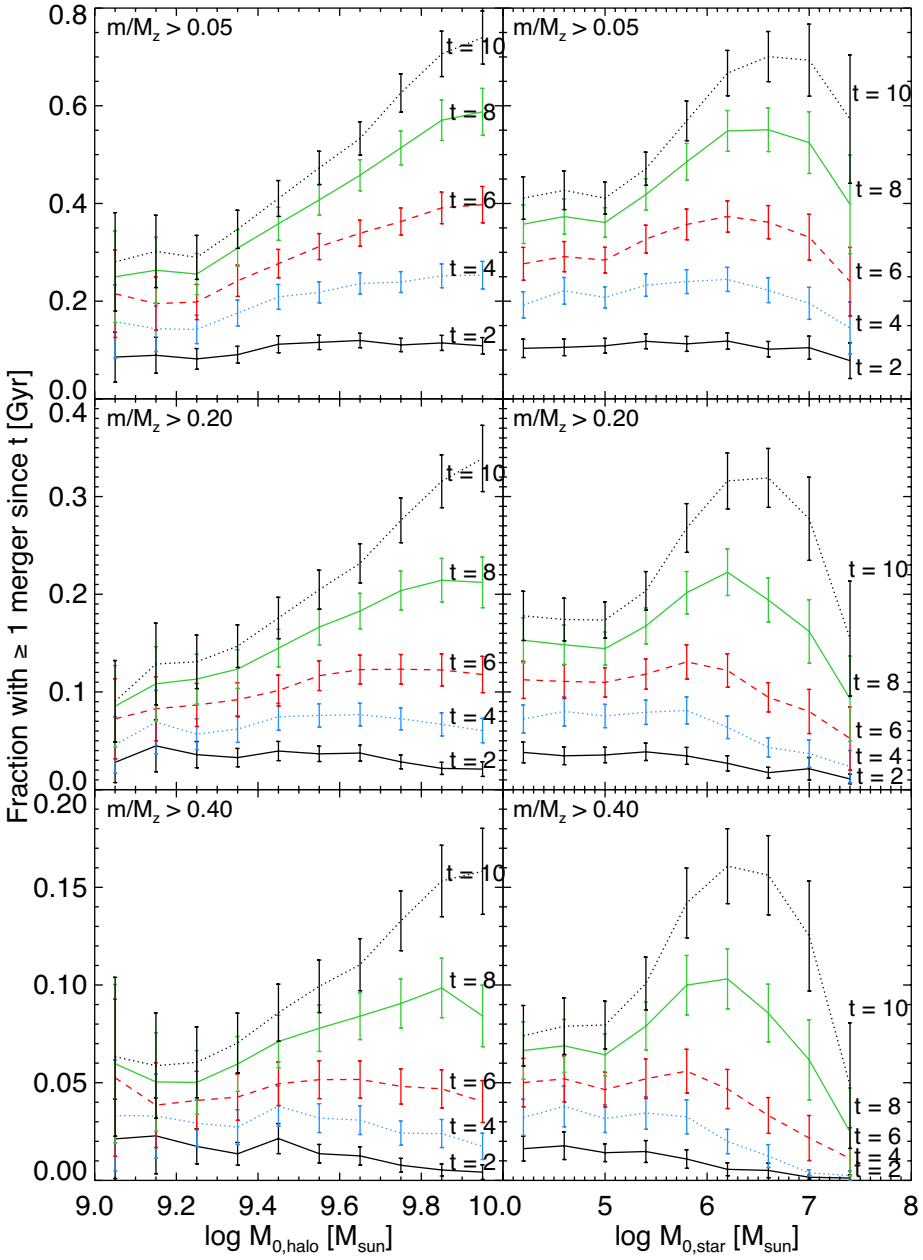

Figure 5.6 – The fraction of dwarf galaxies experiencing a merger within a lookback time of $t = 2$ Gyr, $t = 4$ Gyr, $t = 6$ Gyr, $t = 8$ Gyr, and $t = 10$ Gyr for all three versions of the simulation with virial mass (left panels) and with stellar mass (right panels), where the primary is bright and the secondary is dark with a merger mass ratio $m/M_z \geq 0.05$ (top panels), $m/M_z \geq 0.2$ (middle panels), or $m/M_z \geq 0.4$ (bottom panels). Error bars reflect poisson errors in the sample and number of dwarf galaxies having experienced a merger.

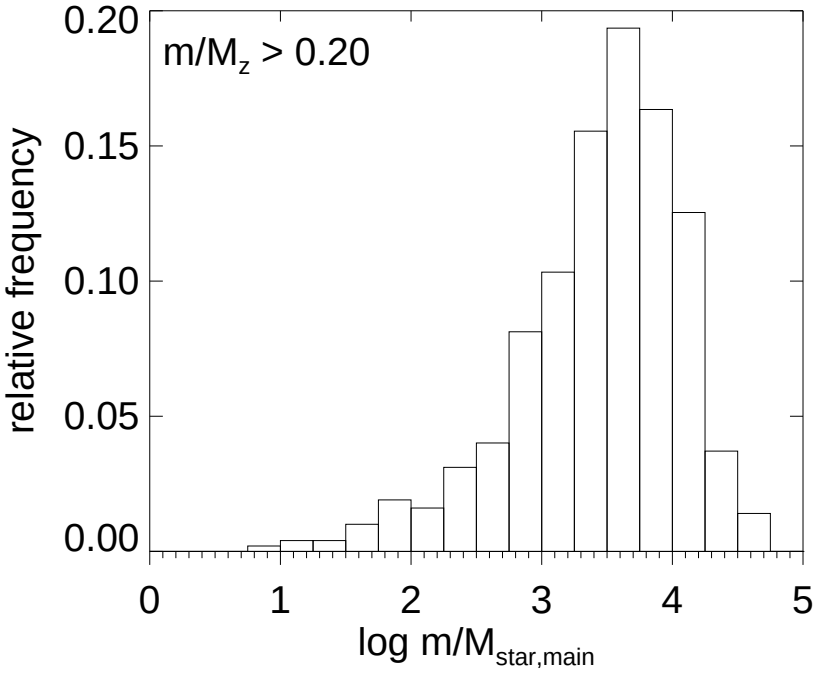

Figure 5.7 – The distribution of secondary halo mass to main stellar mass ratio, $m/M_{\rm stars,main}$, for all mergers where the main halo has stars and $m/M_z \geq 0.2$ and the stellar component has $M_\star \geq 10^5\ M_\odot$. The mass in the stellar component is low for many of the dwarf galaxies, especially at large lookback times, which results in the satellite being more than 1000 times as massive as the stellar component in many cases.

merger for the galaxy (see Chapter 2 and Chapter 3). Therefore it is interesting to explore the mass ratio of the secondary halo and the stellar mass of the primary halo in the dwarf-dark mergers. The distribution of mass ratios is plotted in Fig. 5.7. The log-scale of the horizontal axis shows the enormous range of mass ratios that we find, and reflects the vast range in stellar mass fractions that dwarf galaxies have, even though we restrict this plot to the galaxies with well-resolved stellar components where $M_\star > 10^5\ M_\odot$. Note that Fig. 5.7 shows the mass ratio at the moment just before infall of the secondary. For a deeply embedded pericentric passage the satellite will have lost about 90% of its pre-infall mass by the time of the first passage. Nevertheless, in almost all cases the satellites will still be much more massive than the stellar component at this point in time. Such an encounter will result in severe tidal effects in the host dwarf galaxy as we describe in Chapter 2 and Chapter 3.

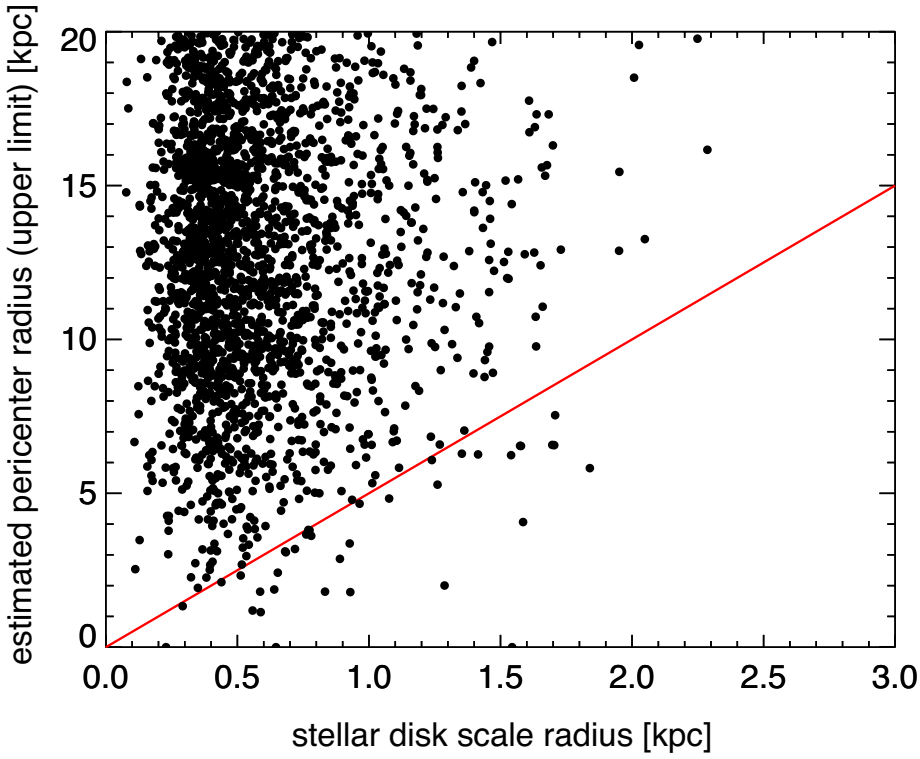

Figure 5.8 – The estimated first pericenter radii versus the disk scale radii of the host galaxies. The red line shows the relation $r_{\rm peri} = 5R_d$. About 1.5% of the 2285 merger cases shown has a pericenter radius $r_{\rm peri} < 5R_d$. The pericenters are upper limits as they are estimated using the closest first approach seen from the simulations and a test particle orbit in a spherical potential. All cases shown have merger mass ratios $m/M_z > 0.2$, therefore dynamical friction will likely result in smaller pericentric radii.

Since dwarfs are typically gas-rich, such an encounter will often imply the triggering of a starburst.

Estimate of the pericentric distances

To determine how close the satellite comes to the central stellar disk of the dwarf galaxy we obtain an estimate of the first pericenter radius combining two methods. If we follow the positions of the dwarf and satellite halos in the N-body simulation itself, this provides an upper limit to the first pericenter that depends on the output frequency, the orbit, and the timescale on which the satellite is destroyed. Using the position and velocity of this first minimum radial distance determined from the simulation we derive another estimate,

based on the energy and angular momentum at this point in time. The pericentric distance is obtained assuming conservation of energy and angular momenta, by requiring that the radial velocity of the satellite be zero at pericenter, and by assuming that the host halo follows a NFW profile. There are significant uncertainties associated to this procedure, but it allows us to obtain an estimate (of the upper limit) of a first pericentric radius.

Figure 5.8 shows the estimated first pericentric radii against the disk scale radius of the host dwarf galaxy at the time of first pericenter in the N-body simulation. We have plotted here only mergers with mass ratios $m/M_z > 0.2$ for dwarf galaxies with $M_{\rm vir} > 5 \times 10^9\, M_\odot$ since $z \sim 0.5$. Almost all pericenters are much larger than the disk radii, but as these estimates are upper limits, a significant fraction could have first pericentric passages close to the stellar disk if dynamical friction were properly taken into account. All points below the red line are mergers where the first pericentric passage is within $5R_d$, which we consider to be close to the disk. Even with the upper limits for the pericentric radii, this is already true for about 1.5% of the $m/M_z > 0.2$, $z < 0.5$, and $M_{\rm vir} > 5 \times 10^9\, M_\odot$ mergers.

5.3.4 Environment

Figure 5.9 shows the $z = 0$ environment of three dwarf galaxies in our sample, all from the scaled by 10 "version": in the outskirts of a larger group (top panels), and in two more isolated environments (middle and bottom panels). Hence, this figure reflects the variety in environments where the isolated dwarf galaxies can be found (in all versions of the simulation in fact).

Interestingly, for this figure we required the dwarf galaxies to have $M_{\rm vir} > 5 \times 10^9\, M_\odot$, and to have experienced a minor merger with a dark satellite since $z = 0.5$ where the pericentric distance upper limit is smaller than the virial radius of the host (sub)halo. In all cases, the dwarf galaxy is the central object within its most direct environment (i.e. it is not a satellite itself)[3]. In the case of the top panel, the dwarf itself has $M_{\rm vir} = 7.0 \times 10^9 M_\odot$, no close neighbors (within its halo tree) with stars, but it is on the edge of a more massive group where the central galaxy, at distance of 1220 kpc, has a virial mass of $M_{\rm vir} = 4.7 \times 10^{12} M_\odot$. The dwarf shown in the middle panel has $M_{\rm vir} = 9.0 \times 10^9\, M_\odot$ and only a few bright neighbors within 1 Mpc, the most massive of which has $M_{\rm vir} = 9.9 \times 10^{10}\, M_\odot$. Finally the bottom panel of Fig. 5.9 shows a dwarf galaxy of $M_{\rm vir} = 6.6 \times 10^9\, M_\odot$ in a filamentary structure with two small groups on either side. The most massive halo in the neighborhood has $M_{\rm vir} = 1.4 \times 10^{11}\, M_\odot$.

[3]Mergers between satellites do happen (Angulo et al. 2009; Deason et al. 2014), but the effects of these on the galaxies within the satellite halos is probably small because of the background potential of the main halo.

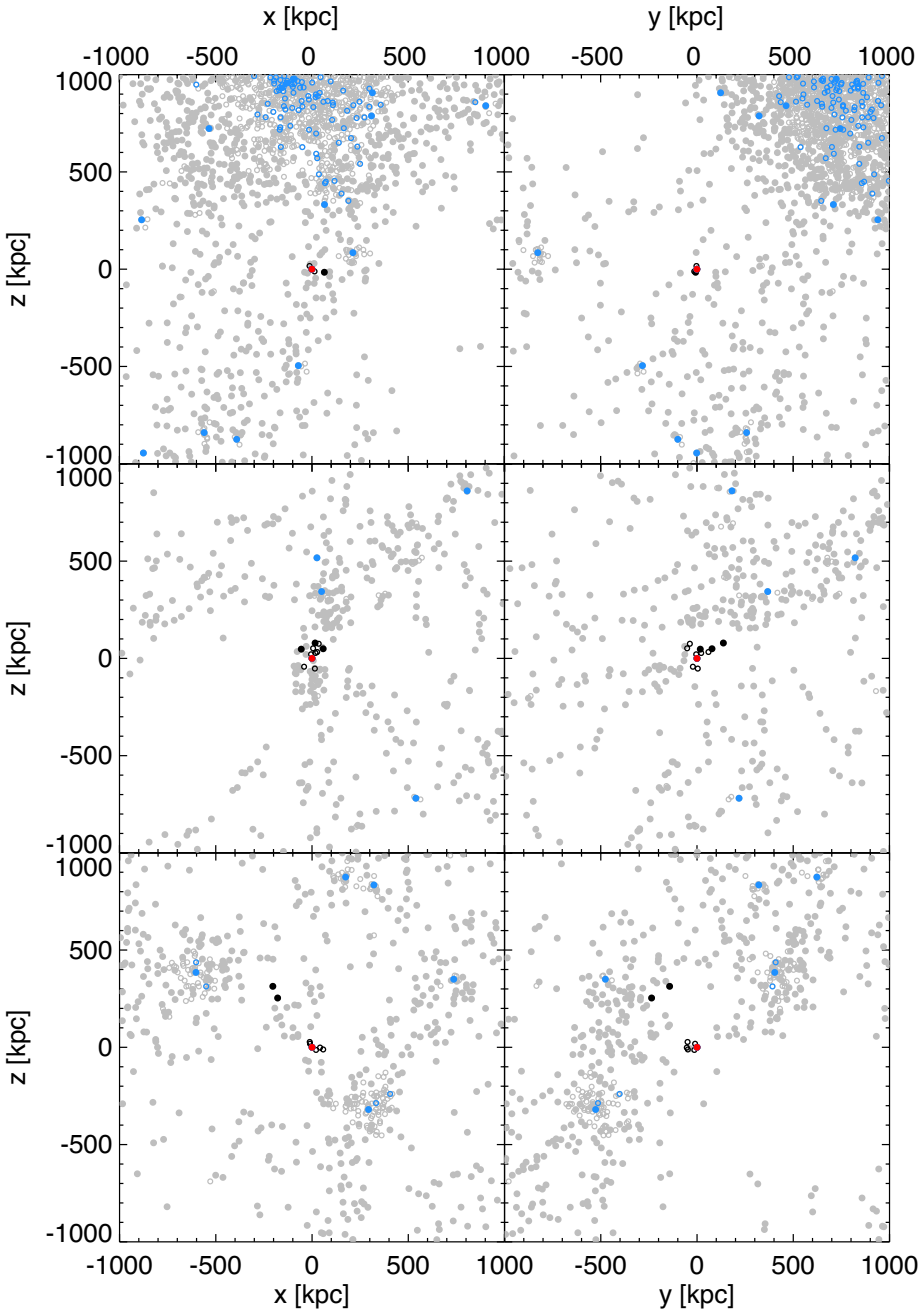

Figure 5.9 – Environment within a box of 2x2x2 Mpc around a subset of three of our selected dwarf galaxies (in red), in the simulation version scaled by a factor 10 in mass. All halos within the box are shown (grey: all; black: part of the tree of the central galaxy; filled circles: central halos; open circles: subhalos) with the ones that have stars highlighted (blue).

5.4 Discussion

In this Chapter we have quantified the likelihood of mergers between dwarf galaxies and dark satellites. To this end we have combined the Millennium-II cosmological N-body simulation, and two scaled down versions, with a semi-analytic galaxy formation model.

The semi-analytic model is necessary to determine whether a halo hosts a bright galaxy or has remained dark. We believe that the specifics of the model do not affect the derived estimates of the merger fractions very strongly because of the relatively weak dependence on virial mass of the host (see e.g. Fig. 5.6), particularly for mergers that have taken place in the last 6 - 8 Gyr. Furthermore the range in which the transition occurs from mostly dark halos to halos hosting luminous galaxies agrees well with the results of a variety of models from the literature (Gnedin 2000; Hoeft et al. 2006; Kaufmann et al. 2007; Okamoto et al. 2008; Gnedin et al. 2009; Li et al. 2010; Sawala et al. 2013).

Although it is not fully correct to rescale the Millennium-II as we have done (doing this properly would require scaling the time axis as well), it is reassuring that the estimates obtained are consistent with extrapolations from the literature. For example, we can compare the fraction of dwarf galaxies that experienced a merger within a certain range of halo mass ratios and within a certain redshift or lookback time to the work of Fakhouri et al. (2010). Although these authors compute merger rates on the basis of mergers of Friends-Of-Friends halos and not the infall of subhalos with respect to the central halo within a FOF-halo, their fitted formula predicts ≈ 0.26 and ≈ 0.50 mergers for a halo with $M_{\rm halo,FOF} \sim 10^9\ M_\odot$ integrated over mass ratios > 0.4 and > 0.2 and redshift $0 < z < 2$, which is close to the values of 27% and 43% we find. Stewart et al. (2008) do use similar definitions of halo masses and mergers (infalling subhalos) as we do, but they define merger mass ratios with respect to the present day mass of the halo. Therefore, although we find a similar dependence on present day virial mass (see their Fig. 6), we can not compare merger fractions quantitatively.

The semi-analytic model as it is implemented does not consider the possibility that mergers with dark objects could significantly impact galaxies, and while this may be the case for large systems, we have shown in Chapter 2, 3, and 4 that this is not true for dwarf galaxies. In most semi-analytic models available in the literature changes in galaxy properties due to mergers (i.e. bursts of star formation, bulge growth) are determined based on (the ratio of) the stellar and cold gas mass of the merging systems (Somerville & Davé 2015, and references therein), and for galaxies like the Milky Way, this ratio is similar to that obtained using their virial masses. On the other hand, for dark–dwarf mergers, the first ratio is zero, and even if the ratio of virial masses is only ~ 0.2, we have shown in Sect. 5.3.2, that the infalling dark halo is almost always much heavier than the stellar component of the dwarf, reaching ratios

as large as $m/M_{\rm star} \gtrsim 10^5$ (although this estimate is somewhat dependent on the specific implementation of baryonic physics on this mass scale). This implies that semi-analytic models should be adjusted to take such mergers into account and hence provide more robust predictions of the properties of dwarf galaxies.

5.5 Conclusions

In a ΛCDM universe dark matter halos are abundant, but toward lower masses a steeply increasing fraction will remain starless. Nevertheless, these small dark matter halos can leave imprints on galaxies, especially on the low mass dwarfs as shown earlier in this Thesis. In this Chapter we have used the large cosmological N-body simulation Millennium-II coupled to a semi-analytic galaxy formation model to determine the fraction of dwarf galaxies that have experienced significant mergers with dark satellites since redshift $z = 2$. To increase the range of resolved halo masses we have scaled down the N-body simulation by a factor of 10 and by a factor of 100 in mass. The rescaled versions of the simulation agree well within the mass range where they overlap, and this procedure thus allows us to resolve infalling satellites down to $M_{\rm halo} = 2 \times 10^6\ M_\odot$ in the "highest resolution version".

For our sample of dwarf galaxies with $10^8\ M_\odot \leq M_{\rm vir} \leq 10^{10}\ M_\odot$, stellar mass $M_\star > 0$, and which are the central galaxy within their halo merger tree, we find that $\sim 27\%$ experiences at least one merger with mass ratio $m/M_z > 0.2$, with a *dark* satellite since $z \sim 2$. Roughly $\sim 10\%$ has experienced at least one such merger for $z < 0.5$.

In Chapters 2 and 3 we have shown the extreme effects such infalling dark satellites can have on dwarf galaxies, causing strong bursts of star formation and severely disturbed morphologies and kinematics. There we found that one of the drivers behind the strength of the effects is the large ratio between the satellite's mass and the host's stellar mass, $m/M_\star$. For the dark-dwarf interactions identified in the cosmological simulation Millennium-II, these $m/M_\star$ ratios are often much larger than we had assumed in Chapters 2 and 3. For example, approximately half of the mergers with virial mass ratios $m/M_z > 0.2$ in our cosmological simulations have $m/M_\star \sim 10^3$–10^5. Although limited by the time resolution of the simulations, we have found that a minimum of 1.5% of the accreted satellites in events with $z < 0.5$, $M_{\rm vir} > 5 \times 10^9\ M_\odot$, and $m/M_z > 0.2$, come within a few disk scale lengths of the stellar disk in their first pericentric passage, thus enhancing their dramatic impact even more.

In conclusion, we have shown that an important fraction of the dwarf galaxy population will have experienced a significant merger with a dark satellite in the not so distant past. These events should therefore be considered if the aim is to understand the properties and evolution of dwarf galaxies.

Bibliography

Aarseth, S. J. 1963, MNRAS, 126, 223
Abraham, R. G., van den Bergh, S., & Nair, P. 2003, ApJ, 588, 218
Ackermann, M., Albert, A., Anderson, B., et al. 2014, Phys. Rev. D, 89, 042001
Adams, E. A. K., Faerman, Y., Janesh, W. F., et al. 2015, A&A, 573, L3
Ajello, M., Gasparrini, D., Sánchez-Conde, M., et al. 2015, ApJL, 800, L27
Allen, S. W., Schmidt, R. W., Fabian, A. C., & Ebeling, H. 2003, MNRAS, 342, 287
Allgood, B., Flores, R. A., Primack, J. R., et al. 2006, MNRAS, 367, 1781
Amorisco, N. C., Evans, N. W., & van de Ven, G. 2014, Nature, 507, 335
Angulo, R. E., Lacey, C. G., Baugh, C. M., & Frenk, C. S. 2009, MNRAS, 399, 983
Arp, H. 1965, ApJ, 142, 402
Arp, H. 1966, ApJS, 14, 1
Ashley, T., Elmegreen, B. G., Johnson, M., et al. 2014, AJ, 148, 130
Ashley, T., Simpson, C. E., & Elmegreen, B. G. 2013, AJ, 146, 42
Athanassoula, E. 2003, MNRAS, 341, 1179
Athanassoula, E., Fady, E., Lambert, J. C., & Bosma, A. 2000, MNRAS, 314, 475
Athanassoula, E., Machado, R. E. G., & Rodionov, S. A. 2013, MNRAS, 429, 1949
Athanassoula, E., Rodionov, S. A., Peschken, N., & Lambert, J. C. 2016, ApJ, 821, 90
Athanassoula, E. & Sellwood, J. A. 1986, MNRAS, 221, 213
Barnes, J. & Hut, P. 1986, Nature, 324, 446
Barnes, J. E. 1988, ApJ, 331, 699
Barnes, J. E. & Hernquist, L. 1992, ARA&A, 30, 705
Begum, A., Chengalur, J. N., Karachentsev, I. D., Sharina, M. E., & Kaisin, S. S. 2008, MNRAS, 386, 1667
Behroozi, P. S., Wechsler, R. H., & Conroy, C. 2013a, ApJ, 770, 57
Behroozi, P. S., Wechsler, R. H., & Wu, H.-Y. 2013b, ApJ, 762, 109
Bekki, K. & Chiba, M. 2006, ApJL, 637, L97
Bekki, K. & Freeman, K. C. 2002, ApJL, 574, L21
Bekki, K., Koribalski, B. S., & Kilborn, V. A. 2005, MNRAS, 363, L21

Benítez-Llambay, A., Navarro, J. F., Abadi, M. G., et al. 2013, ApJL, 763, L41
Benson, A. J., Lacey, C. G., Frenk, C. S., Cole, S., & Baugh, C. M. 2004, in Astronomical Society of the Pacific Conference Series, Vol. 327, Satellites and Tidal Streams, ed. F. Prada, D. Martinez Delgado, & T. J. Mahoney, 125
Bergvall, N. 2012, Star Forming Dwarf Galaxies, ed. P. Papaderos, S. Recchi, & G. Hensler, 175
Bergvall, N., Marquart, T., Way, M. J., et al. 2015, ArXiv e-prints 1501.06928
Berrier, J. C., Bullock, J. S., Barton, E. J., et al. 2006, ApJ, 652, 56
Binney, J. & Merrifield, M. 1998, Galactic Astronomy (Princeton, NJ: Princeton University Press)
Binney, J. & Tremaine, S. 1987, Galactic Dynamics (Princeton, NJ: Princeton University Press)
Blanton, M. R., Dalcanton, J., Eisenstein, D., et al. 2001, AJ, 121, 2358
Blanton, M. R. & Moustakas, J. 2009, ARA&A, 47, 159
Blumenthal, G. R., Faber, S. M., Primack, J. R., & Rees, M. J. 1984, Nature, 311, 517
Bose, S., Hellwing, W. A., Frenk, C. S., et al. 2016, MNRAS, 455, 318
Bosma, A. 1978, PhD thesis, PhD Thesis, Groningen Univ., (1978)
Bournaud, F. 2011, in EAS Publications Series, Vol. 51, EAS Publications Series, ed. C. Charbonnel & T. Montmerle, 107–131
Bournaud, F., Chapon, D., Teyssier, R., et al. 2011, ApJ, 730, 4
Boylan-Kolchin, M., Springel, V., White, S. D. M., Jenkins, A., & Lemson, G. 2009, MNRAS, 398, 1150
Breddels, M. A. & Helmi, A. 2013, A&A, 558, A35
Brooks, A. M. & Zolotov, A. 2014, ApJ, 786, 87
Brosch, N., Almoznino, E., & Heller, A. B. 2004, MNRAS, 349, 357
Cannon, J. M., Giovanelli, R., Haynes, M. P., et al. 2011, ApJL, 739, L22
Cannon, J. M., Johnson, M., McQuinn, K. B. W., et al. 2014, ApJL, 787, L1
Cannon, J. M., Martinkus, C. P., Leisman, L., et al. 2015, AJ, 149, 72
Cannon, J. M., O'Leary, E. M., Weisz, D. R., et al. 2012, ApJ, 747, 122
Chabrier, G. 2003, PASP, 115, 763
Chakrabarti, S. & Blitz, L. 2009, MNRAS, 399, L118
Chamberlin, T. C. 1901, ApJ, 14, 17
Cole, S., Helly, J., Frenk, C. S., & Parkinson, H. 2008, MNRAS, 383, 546
Coleman, M., Da Costa, G. S., Bland-Hawthorn, J., et al. 2004, AJ, 127, 832
Conselice, C. J. 2003, ApJS, 147, 1
Conselice, C. J. 2006, MNRAS, 373, 1389
Conselice, C. J. 2014, ARA&A, 52, 291
Conselice, C. J., Bershady, M. A., & Jangren, A. 2000, ApJ, 529, 886
Cox, T. J., Jonsson, P., Somerville, R. S., Primack, J. R., & Dekel, A. 2008, MNRAS, 384, 386
Crain, R. A., Eke, V. R., Frenk, C. S., et al. 2007, MNRAS, 377, 41
Croton, D. J., Springel, V., White, S. D. M., et al. 2006, MNRAS, 365, 11
Dalcanton, J. J., Spergel, D. N., Gunn, J. E., Schmidt, M., & Schneider, D. P. 1997, AJ, 114, 635
Dalcanton, J. J., Williams, B. F., Seth, A. C., et al. 2009, ApJS, 183, 67
Dale, D. A., Cohen, S. A., Johnson, L. C., et al. 2009, ApJ, 703, 517
Dalla Vecchia, C. & Schaye, J. 2008, MNRAS, 387, 1431

Dalton, G., Trager, S., Abrams, D. C., et al. 2014, in Proceedings of the SPIE, Vol. 9147, Ground-based and Airborne Instrumentation for Astronomy V, 91470L
Davies, J. I., Disney, M. J., Minchin, R. F., Auld, R., & Smith, R. 2006, MNRAS, 368, 1479
Davis, M., Efstathiou, G., Frenk, C. S., & White, S. D. M. 1985, ApJ, 292, 371
Daylan, T., Finkbeiner, D. P., Hooper, D., et al. 2016, Physics of the Dark Universe, 12, 1
de Blok, W. J. G. & Walter, F. 2000, ApJL, 537, L95
De Lucia, G. & Blaizot, J. 2007, MNRAS, 375, 2
De Lucia, G. & Helmi, A. 2008, MNRAS, 391, 14
De Lucia, G., Kauffmann, G., & White, S. D. M. 2004, MNRAS, 349, 1101
de Vaucouleurs, G. 1948, Annales d'Astrophysique, 11, 247
Deason, A., Wetzel, A., & Garrison-Kimmel, S. 2014, ApJ, 794, 115
Di Matteo, P., Bournaud, F., Martig, M., et al. 2008, A&A, 492, 31
Di Matteo, P., Combes, F., Melchior, A.-L., & Semelin, B. 2007, A&A, 468, 61
D'Onghia, E. 2015, ApJL, 808, L8
Dressler, A. 1980, ApJ, 236, 351
Duc, P.-A., Cuillandre, J.-C., Serra, P., et al. 2011, MNRAS, 417, 863
Ekta, B. & Chengalur, J. N. 2010, MNRAS, 403, 295
Ellison, S. L., Nair, P., Patton, D. R., et al. 2011, MNRAS, 416, 2182
Elmegreen, B. G., Zhang, H.-X., & Hunter, D. A. 2012, ApJ, 747, 105
Erkal, D. & Belokurov, V. 2015, MNRAS, 454, 3542
Fakhouri, O. & Ma, C.-P. 2008, MNRAS, 386, 577
Fakhouri, O., Ma, C.-P., & Boylan-Kolchin, M. 2010, MNRAS, 406, 2267
Filho, M. E., Sánchez Almeida, J., Muñoz-Tuñón, C., et al. 2015, ApJ, 802, 82
Filho, M. E., Winkel, B., Sánchez Almeida, J., et al. 2013, A&A, 558, A18
Font, A. S., Navarro, J. F., Stadel, J., & Quinn, T. 2001, ApJL, 563, L1
Freeman, K. & Bland-Hawthorn, J. 2002, ARA&A, 40, 487
Gallagher, III, J. S. & Hunter, D. A. 1984, ARA&A, 22, 37
Gao, L., Navarro, J. F., Frenk, C. S., et al. 2012, MNRAS, 425, 2169
Garnett, D. R. 1990, ApJ, 363, 142
Garrison-Kimmel, S., Boylan-Kolchin, M., Bullock, J. S., & Lee, K. 2014, MNRAS, 438, 2578
Genel, S., Genzel, R., Bouché, N., Naab, T., & Sternberg, A. 2009, ApJ, 701, 2002
Gerssen, J., Kuijken, K., & Merrifield, M. R. 1997, MNRAS, 288, 618
Gil de Paz, A., Madore, B. F., & Pevunova, O. 2003, ApJS, 147, 29
Gingold, R. A. & Monaghan, J. J. 1977, MNRAS, 181, 375
Giovanelli, R., Haynes, M. P., Kent, B. R., et al. 2005, AJ, 130, 2598
Gnedin, N. Y. 2000, ApJ, 542, 535
Gnedin, N. Y., Tassis, K., & Kravtsov, A. V. 2009, ApJ, 697, 55
Gottlöber, S., Hoffman, Y., & Yepes, G. 2010, ArXiv e-prints 1005.2687
Gottlöber, S., Klypin, A., & Kravtsov, A. V. 2001, ApJ, 546, 223
Governato, F., Brook, C., Mayer, L., et al. 2010, Nature, 463, 203
Governato, F., Zolotov, A., Pontzen, A., et al. 2012, MNRAS, 422, 1231
Grebel, E. K., Gallagher, III, J. S., & Harbeck, D. 2003, AJ, 125, 1926
Guo, Q., White, S., Boylan-Kolchin, M., et al. 2011, MNRAS, 413, 101
Guo, Q., White, S., Li, C., & Boylan-Kolchin, M. 2010, MNRAS, 404, 1111
Helmi, A., Sales, L. V., Starkenburg, E., et al. 2012, ApJL, 758, L5
Hernquist, L. 1989, Nature, 340, 687
Hernquist, L. 1990, ApJ, 356, 359

Hernquist, L. 1993, ApJS, 86, 389
Hernquist, L. & Katz, N. 1989, ApJS, 70, 419
Hockney, R. W. & Eastwood, J. W. 1988, Computer simulation using particles (Bristol: Hilger)
Hoeft, M., Yepes, G., Gottlöber, S., & Springel, V. 2006, MNRAS, 371, 401
Holmberg, E. 1941, ApJ, 94, 385
Holwerda, B. W., Muñoz-Mateos, J.-C., Comerón, S., et al. 2014, ApJ, 781, 12
Holwerda, B. W., Pirzkal, N., Cox, T. J., et al. 2011a, MNRAS, 416, 2426
Holwerda, B. W., Pirzkal, N., de Blok, W. J. G., & Blyth, S.-L. 2013, MNRAS, 435, 1020
Holwerda, B. W., Pirzkal, N., de Blok, W. J. G., et al. 2011b, MNRAS, 416, 2437
Holwerda, B. W., Pirzkal, N., de Blok, W. J. G., et al. 2011c, MNRAS, 416, 2401
Holwerda, B. W., Pirzkal, N., de Blok, W. J. G., et al. 2011d, MNRAS, 416, 2415
Holwerda, B. W., Pirzkal, N., de Blok, W. J. G., & van Driel, W. 2011e, MNRAS, 416, 2447
Holwerda, B. W., Pirzkal, N., & Heiner, J. S. 2012, MNRAS, 427, 3159
Hopkins, P. F., Cox, T. J., Younger, J. D., & Hernquist, L. 2009, ApJ, 691, 1168
Hopkins, P. F., Hernquist, L., Cox, T. J., Younger, J. D., & Besla, G. 2008, ApJ, 688, 757
House, E. L., Brook, C. B., Gibson, B. K., et al. 2011, MNRAS, 415, 2652
Hu, C.-Y., Naab, T., Walch, S., Glover, S. C. O., & Clark, P. C. 2016, MNRAS
Huang, S. & Carlberg, R. G. 1997, ApJ, 480, 503
Huang, S., Haynes, M. P., Giovanelli, R., et al. 2012, AJ, 143, 133
Hubble, E. P. 1926, ApJ, 64, 321
Hubble, E. P. 1936, Realm of the Nebulae (New Haven: Yale University Press)
Hunter, D. A. & Elmegreen, B. G. 2004, AJ, 128, 2170
Hunter, D. A. & Elmegreen, B. G. 2006, ApJS, 162, 49
Hunter, D. A., Elmegreen, B. G., Oh, S.-H., et al. 2011, AJ, 142, 121
Hunter, D. A., Ficut-Vicas, D., Ashley, T., et al. 2012, AJ, 144, 134
Ibata, R. A., Lewis, G. F., Irwin, M. J., & Quinn, T. 2002, MNRAS, 332, 915
James, B. L., Koposov, S., Stark, D. P., et al. 2015, MNRAS, 448, 2687
Janowiecki, S., Leisman, L., Józsa, G., et al. 2015, ApJ, 801, 96
Johnston, K. V., Spergel, D. N., & Haydn, C. 2002, ApJ, 570, 656
Kannan, R., Macciò, A. V., Pasquali, A., Moster, B. P., & Walter, F. 2012, ApJ, 746, 10
Karachentsev, I. D., Karachentseva, V. E., & Huchtmeier, W. K. 2006, A&A, 451, 817
Karachentsev, I. D., Karachentseva, V. E., Huchtmeier, W. K., & Makarov, D. I. 2004, AJ, 127, 2031
Karachentsev, I. D., Karachentseva, V. E., Huchtmeier, W. K., Makarov, D. I., & Kaisin, S. S. 2008, in IAU Symposium, Vol. 244, IAU Symposium, ed. J. I. Davies & M. J. Disney, 235–246
Karachentsev, I. D., Makarov, D. I., Karachentseva, V. E., & Melnyk, O. V. 2011, Astrophysical Bulletin, 66, 1
Karachentsev, I. D., Makarova, L. N., Makarov, D. I., Tully, R. B., & Rizzi, L. 2015, MNRAS, 447, L85
Kauffmann, G., Colberg, J. M., Diaferio, A., & White, S. D. M. 1999, MNRAS, 303, 188
Kaufmann, T., Wheeler, C., & Bullock, J. S. 2007, MNRAS, 382, 1187
Kautsch, S. J., Grebel, E. K., Barazza, F. D., & Gallagher, III, J. S. 2006, A&A, 445, 765
Kaviraj, S. 2014a, MNRAS, 440, 2944
Kaviraj, S. 2014b, MNRAS, 437, L41
Kazantzidis, S., Łokas, E. L., Mayer, L., Knebe, A., & Klimentowski, J. 2011, ApJL, 740, L24

Kazantzidis, S., Magorrian, J., & Moore, B. 2004, ApJ, 601, 37
Kennicutt, Jr., R. C. 1989, ApJ, 344, 685
Kennicutt, Jr., R. C. 1998, ApJ, 498, 541
Kennicutt, Jr., R. C., Lee, J. C., Funes, José G., S. J., Sakai, S., & Akiyama, S. 2008, ApJS, 178, 247
Kent, B. R., Giovanelli, R., Haynes, M. P., et al. 2007, ApJL, 665, L15
Kim, J. H., Peirani, S., Kim, S., et al. 2014, ApJ, 789, 90
Klimentowski, J., Łokas, E. L., Knebe, A., et al. 2010, MNRAS, 402, 1899
Klypin, A., Kravtsov, A. V., Valenzuela, O., & Prada, F. 1999, ApJ, 522, 82
Knapen, J. H. & Cisternas, M. 2015, ApJL, 807, L16
Knapen, J. H. & James, P. A. 2009, ApJ, 698, 1437
Komatsu, E., Smith, K. M., Dunkley, J., et al. 2011, ApJS, 192, 18
Kormendy, J. & Fisher, D. B. 2005, in Revista Mexicana de Astronomia y Astrofisica Conference Series, Vol. 23, Revista Mexicana de Astronomia y Astrofisica Conference Series, ed. S. Torres-Peimbert & G. MacAlpine, 101–108
Kormendy, J. & Freeman, K. C. 2016, ApJ, 817, 84
Krajnović, D., Alatalo, K., Blitz, L., et al. 2013, MNRAS, 432, 1768
Lagos, C. d. P., Lacey, C. G., & Baugh, C. M. 2013, MNRAS, 436, 1787
Lee, J. C., Gil de Paz, A., Kennicutt, Jr., R. C., et al. 2011, ApJS, 192, 6
Lee, J. C., Kennicutt, Jr., R. C., Funes, S. J. J. G., Sakai, S., & Akiyama, S. 2009, ApJ, 692, 1305
Lelli, F., Fraternali, F., & Verheijen, M. 2014a, A&A, 563, A27
Lelli, F., Verheijen, M., & Fraternali, F. 2014b, MNRAS, 445, 1694
Li, Y.-S., De Lucia, G., & Helmi, A. 2010, MNRAS, 401, 2036
Li, Y.-S., Helmi, A., De Lucia, G., & Stoehr, F. 2009, MNRAS, 397, L87
Lisker, T., Wittmann, C., Pak, M., et al. 2015, in American Astronomical Society Meeting Abstracts, Vol. 225, American Astronomical Society Meeting Abstracts, 437.05
Łokas, E. L., Ebrová, I., Pino, A. d., & Semczuk, M. 2014, MNRAS, 445, L6
López-Sánchez, Á. R. 2010, A&A, 521, A63
Lora, V., Just, A., Sánchez-Salcedo, F. J., & Grebel, E. K. 2012, ApJ, 757, 87
Lotz, J. M., Primack, J., & Madau, P. 2004, AJ, 128, 163
Lucy, L. B. 1977, AJ, 82, 1013
Macciò, A. V., Dutton, A. A., & van den Bosch, F. C. 2008, MNRAS, 391, 1940
Makarov, D., Makarova, L., Sharina, M., et al. 2012, MNRAS, 425, 709
Martin, C. L. 2005, ApJ, 621, 227
Martínez-Delgado, D., Romanowsky, A. J., Gabany, R. J., et al. 2012, ApJL, 748, L24
Mashchenko, S., Wadsley, J., & Couchman, H. M. P. 2008, Science, 319, 174
Massey, P., Olsen, K. A. G., Hodge, P. W., et al. 2007, AJ, 133, 2393
Mateo, M. L. 1998, ARA&A, 36, 435
Mayer, L., Governato, F., Colpi, M., et al. 2001a, ApJ, 559, 754
Mayer, L., Governato, F., Colpi, M., et al. 2001b, ApJL, 547, L123
Mayer, L., Mastropietro, C., Wadsley, J., Stadel, J., & Moore, B. 2006, MNRAS, 369, 1021
McConnachie, A. W. 2012, AJ, 144, 4
McQuinn, K. B. W., Cannon, J. M., Dolphin, A. E., et al. 2015, ApJ, 802, 66
McQuinn, K. B. W., Skillman, E. D., Cannon, J. M., et al. 2010, ApJ, 721, 297
Meurer, G. R., Staveley-Smith, L., & Killeen, N. E. B. 1998, MNRAS, 300, 705
Mihos, J. C. & Hernquist, L. 1994a, ApJL, 425, L13
Mihos, J. C. & Hernquist, L. 1994b, ApJL, 431, L9

Minchin, R., Davies, J., Disney, M., et al. 2005, ApJL, 622, L21
Mo, H., van den Bosch, F. C., & White, S. 2010, Galaxy Formation and Evolution (Cambridge University Press)
Mo, H. J., Mao, S., & White, S. D. M. 1998, MNRAS, 295, 319
Monaghan, J. J. 1992, ARA&A, 30, 543
Moore, B., Ghigna, S., Governato, F., et al. 1999, ApJL, 524, L19
Moster, B. P., Macciò, A. V., Somerville, R. S., Johansson, P. H., & Naab, T. 2010, MNRAS, 403, 1009
Moster, B. P., Naab, T., & White, S. D. M. 2013, MNRAS, 428, 3121
Muñoz-Cuartas, J. C., Macciò, A. V., Gottlöber, S., & Dutton, A. A. 2011, MNRAS, 411, 584
Naab, T., Jesseit, R., & Burkert, A. 2006, MNRAS, 372, 839
Navarro, J. F., Frenk, C. S., & White, S. D. M. 1996, ApJ, 462, 563
Neistein, E. & Dekel, A. 2008, MNRAS, 388, 1792
Nidever, D. L., Ashley, T., Slater, C. T., et al. 2013, ApJL, 779, L15
Nierenberg, A. M., Treu, T., Menci, N., et al. 2016, ArXiv e-prints 1603.01614
Nilson, P. 1973, Uppsala general catalogue of galaxies (Uppsala: Astronomiska Observatorium)
Okamoto, T., Frenk, C. S., Jenkins, A., & Theuns, T. 2010, MNRAS, 406, 208
Okamoto, T., Gao, L., & Theuns, T. 2008, MNRAS, 390, 920
Ott, J., Stilp, A. M., Warren, S. R., et al. 2012, AJ, 144, 123
Papaderos, P., Guseva, N. G., Izotov, Y. I., & Fricke, K. J. 2008, A&A, 491, 113
Paudel, S., Duc, P. A., & Ree, C. H. 2015, AJ, 149, 114
Pearson, S., Besla, G., Putman, M. E., et al. 2016, MNRAS, 459, 1827
Peebles, P. J. E. 1982, ApJL, 263, L1
Pfleiderer, J. 1963, Z. Astrophys., 58, 12
Pfleiderer, J. & Siedentopf, H. 1961, Z. Astrophys., 51, 201
Planck Collaboration, Ade, P. A. R., Aghanim, N., et al. 2014, A&A, 571, A16
Pontzen, A. & Governato, F. 2012, MNRAS, 421, 3464
Postman, M. & Geller, M. J. 1984, ApJ, 281, 95
Press, W. H. & Schechter, P. 1974, ApJ, 187, 425
Primack, J. R. 2005, New. Astron. Rev., 49, 25
Purcell, C. W., Kazantzidis, S., & Bullock, J. S. 2009, ApJL, 694, L98
Pustilnik, S. A. 2008, in IAU Symposium, Vol. 244, Dark Galaxies and Lost Baryons, ed. J. I. Davies & M. J. Disney, 341–345
Qu, Y., Di Matteo, P., Lehnert, M. D., & van Driel, W. 2011, A&A, 530, A10
Quinn, P. J. & Goodman, J. 1986, ApJ, 309, 472
Quinn, P. J., Hernquist, L., & Fullagar, D. P. 1993, ApJ, 403, 74
Rees, M. J. & Ostriker, J. P. 1977, MNRAS, 179, 541
Ricotti, M. & Gnedin, N. Y. 2005, ApJ, 629, 259
Robertson, B. E. & Kravtsov, A. V. 2008, ApJ, 680, 1083
Rocha, M., Peter, A. H. G., Bullock, J. S., et al. 2013, MNRAS, 430, 81
Roman, J. & Trujillo, I. 2016, ArXiv e-prints 1603.03494
Roychowdhury, S., Chengalur, J. N., Begum, A., & Karachentsev, I. D. 2010, MNRAS, 404, L60
Rubin, V. C. & Ford, Jr., W. K. 1970, ApJ, 159, 379
Rubin, V. C., Ford, W. K. J., & . Thonnard, N. 1980, ApJ, 238, 471
Sánchez, S. F., Kennicutt, R. C., Gil de Paz, A., et al. 2012, A&A, 538, A8

Sánchez Almeida, J., Elmegreen, B. G., Muñoz-Tuñón, C., & Elmegreen, D. M. 2014, A&ARv, 22, 71
Sánchez-Janssen, R., Méndez-Abreu, J., & Aguerri, J. A. L. 2010, MNRAS, 406, L65
Sandage, A. 1961, The Hubble atlas of galaxies (Washington: Carnegie Institution)
Sawala, T., Frenk, C. S., Crain, R. A., et al. 2013, MNRAS, 431, 1366
Sawala, T., Frenk, C. S., Fattahi, A., et al. 2016a, MNRAS, 457, 1931
Sawala, T., Frenk, C. S., Fattahi, A., et al. 2015, MNRAS, 448, 2941
Sawala, T., Frenk, C. S., Fattahi, A., et al. 2016b, MNRAS, 456, 85
Scannapieco, C., Wadepuhl, M., Parry, O. H., et al. 2012, MNRAS, 423, 1726
Schaye, J. 2004, ApJ, 609, 667
Schaye, J. & Dalla Vecchia, C. 2008, MNRAS, 383, 1210
Schaye, J., Dalla Vecchia, C., Booth, C. M., et al. 2010, MNRAS, 402, 1536
Schombert, J. M., McGaugh, S. S., & Eder, J. A. 2001, AJ, 121, 2420
Schwartz, C. M. & Martin, C. L. 2004, ApJ, 610, 201
Schweizer, F. 1990, Interactions in our time., ed. Wielen, R., 60–71
Sérsic, J. L. 1963, Boletin de la Asociacion Argentina de Astronomia La Plata Argentina, 6, 41
Simon, J. D., Geha, M., Minor, Q. E., et al. 2011, ApJ, 733, 46
Simpson, C. M., Bryan, G. L., Johnston, K. V., et al. 2013, MNRAS, 432, 1989
Slater, C. T. & Bell, E. F. 2013, ApJ, 773, 17
Sofue, Y. 1994, ApJ, 423, 207
Somerville, R. S. & Davé, R. 2015, ARA&A, 53, 51
Springel, V. 2005, MNRAS, 364, 1105
Springel, V. 2010a, MNRAS, 401, 791
Springel, V. 2010b, ARA&A, 48, 391
Springel, V., Di Matteo, T., & Hernquist, L. 2005, MNRAS, 361, 776
Springel, V. & Hernquist, L. 2005, ApJL, 622, L9
Springel, V., Wang, J., Vogelsberger, M., et al. 2008, MNRAS, 391, 1685
Springel, V. & White, S. D. M. 1999, MNRAS, 307, 162
Springel, V., White, S. D. M., Tormen, G., & Kauffmann, G. 2001a, MNRAS, 328, 726
Springel, V., Yoshida, N., & White, S. D. M. 2001b, New. Astron., 6, 79
Starkenburg, E., Helmi, A., De Lucia, G., et al. 2013, MNRAS, 429, 725
Starkenburg, T. K. & Helmi, A. 2015, A&A, 575, A59
Starkenburg, T. K., Helmi, A., & Sales, L. V. 2016, A&A, 587, A24
Stewart, K. R., Bullock, J. S., Wechsler, R. H., & Maller, A. H. 2009, ApJ, 702, 307
Stewart, K. R., Bullock, J. S., Wechsler, R. H., Maller, A. H., & Zentner, A. R. 2008, ApJ, 683, 597
Stierwalt, S., Besla, G., Patton, D., et al. 2015, ApJ, 805, 2
Tamman, G. 1994, in European Southern Observatory Conference and Workshop Proceedings, Vol. 49, Dwarf galaxies, ed. G. Meylan & P. Prugniel
Tashpulatov, N. 1969, Soviet Astronomy, 46, 1236
Tashpulatov, N. 1970, Soviet Astronomy, 47, 277
Taylor, C. L., Brinks, E., Grashuis, R. M., & Skillman, E. D. 1995, ApJS, 99, 427
Taylor, E. N. & Webster, R. L. 2005, ApJ, 634, 1067
Teyssier, R. 2015, ARA&A, 53, 325
Teyssier, R., Chapon, D., & Bournaud, F. 2010, ApJL, 720, L149
Teyssier, R., Pontzen, A., Dubois, Y., & Read, J. I. 2013, MNRAS, 429, 3068
The Dark Energy Survey Collaboration. 2005, ArXiv e-prints 0510346

Tolstoy, E., Hill, V., & Tosi, M. 2009, ARA&A, 47, 371
Toomre, A. 1964, ApJ, 139, 1217
Toomre, A. 1974, in IAU Symposium, Vol. 58, The Formation and Dynamics of Galaxies, ed. J. R. Shakeshaft, 347–363
Toomre, A. 1977, in Evolution of Galaxies and Stellar Populations, ed. B. M. Tinsley & R. B. G. Larson D. Campbell, 401
Toomre, A. & Toomre, J. 1972, ApJ, 178, 623
Toth, G. & Ostriker, J. P. 1992, ApJ, 389, 5
Trentham, N., Möller, O., & Ramirez-Ruiz, E. 2001, MNRAS, 322, 658
van den Bosch, F. C. & Jiang, F. 2014, ArXiv e-prints 1403.6835
van den Bosch, F. C., Tormen, G., & Giocoli, C. 2005, MNRAS, 359, 1029
van der Kruit, P. C. & Freeman, K. C. 2011, ARA&A, 49, 301
van Dokkum, P. G. 2005, AJ, 130, 2647
van Dokkum, P. G., Abraham, R., Merritt, A., et al. 2015, ApJL, 798, L45
van Zee, L. 2000, AJ, 119, 2757
van Zee, L. 2001, AJ, 121, 2003
van Zee, L., Salzer, J. J., & Skillman, E. D. 2001, AJ, 122, 121
Vegetti, S., Koopmans, L. V. E., Bolton, A., Treu, T., & Gavazzi, R. 2010, MNRAS, 408, 1969
Vegetti, S., Lagattuta, D. J., McKean, J. P., et al. 2012, Nature, 481, 341
Velazquez, H. & White, S. D. M. 1999, MNRAS, 304, 254
Vera-Ciro, C., D'Onghia, E., Navarro, J., & Abadi, M. 2014, ApJ, 794, 173
Verbeke, R., De Rijcke, S., Koleva, M., et al. 2014, MNRAS, 442, 1830
Verde, L., Heavens, A. F., Percival, W. J., et al. 2002, MNRAS, 335, 432
Villalobos, Á. & Helmi, A. 2008, MNRAS, 391, 1806
Vogelsberger, M., Zavala, J., & Loeb, A. 2012, MNRAS, 423, 3740
von Hoerner, S. 1960, Z. Astrophys., 50
Wagner-Kaiser, R., De Maio, T., Sarajedini, A., & Chakrabarti, S. 2014, MNRAS, 443, 3260
Walker, I. R., Mihos, J. C., & Hernquist, L. 1996, ApJ, 460, 121
Walter, F., Brinks, E., de Blok, W. J. G., et al. 2008, AJ, 136, 2563
Wang, L., Dutton, A. A., Stinson, G. S., et al. 2015, MNRAS, 454, 83
Warren, B. E., Jerjen, H., & Koribalski, B. S. 2007, AJ, 134, 1849
Warren, S. R., Skillman, E. D., Stilp, A. M., et al. 2012, ApJ, 757, 84
Weisz, D. R., Dolphin, A. E., Skillman, E. D., et al. 2014, ApJ, 789, 148
Weisz, D. R., Johnson, B. D., Johnson, L. C., et al. 2012, ApJ, 744, 44
Westfall, K. B., Bershady, M. A., Verheijen, M. A. W., et al. 2011, ApJ, 742, 18
Wetzel, A. R., Tinker, J. L., Conroy, C., & van den Bosch, F. C. 2013, MNRAS, 432, 336
White, S. D. M. & Rees, M. J. 1978, MNRAS, 183, 341
Whitmore, B. C., Gilmore, D. M., & Jones, C. 1993, ApJ, 407, 489
Willett, K. W., Schawinski, K., Simmons, B. D., et al. 2015, MNRAS, 449, 820
Wyse, R. F. G. 2001, in Astronomical Society of the Pacific Conference Series, Vol. 230, Galaxy Disks and Disk Galaxies, ed. J. G. Funes & E. M. Corsini, 71–80
Xu, G. 1995, ApJS, 98, 355
Yabushita, S. 1971, MNRAS, 153, 97
Yaryura, C. Y., Helmi, A., Abadi, M. G., & Starkenburg, E. 2016, MNRAS, 457, 2415
Yoachim, P. & Dalcanton, J. J. 2006, AJ, 131, 226
Yozin, C. & Bekki, K. 2012, ApJL, 756, L18

Zavala, J., Jing, Y. P., Faltenbacher, A., et al. 2009, ApJ, 700, 1779
Zemp, M., Gnedin, O. Y., Gnedin, N. Y., & Kravtsov, A. V. 2011, ApJS, 197, 30
Zhang, H.-X., Hunter, D. A., Elmegreen, B. G., Gao, Y., & Schruba, A. 2012, AJ, 143, 47
Zwicky, F. 1933, Helvetica Physica Acta, 6, 110
Zwicky, F. 1937, ApJ, 86, 217
Zwicky, F., Herzog, E., & Wild, P. 1968, Catalogue of galaxies and of clusters of galaxies (Pasadena: California Institute of Technology)
Zwicky, F., Herzog, E., Wild, P., Karpowicz, M., & Kowal, C. T. 1961, Catalogue of galaxies and of clusters of galaxies, Vol. I (Pasadena: California Institute of Technology)
Zwicky, F. & Zwicky, M. A. 1971, Catalogue of selected compact galaxies and of post-eruptive galaxies (Guemligen: Zwicky)

Nederlandse Samenvatting

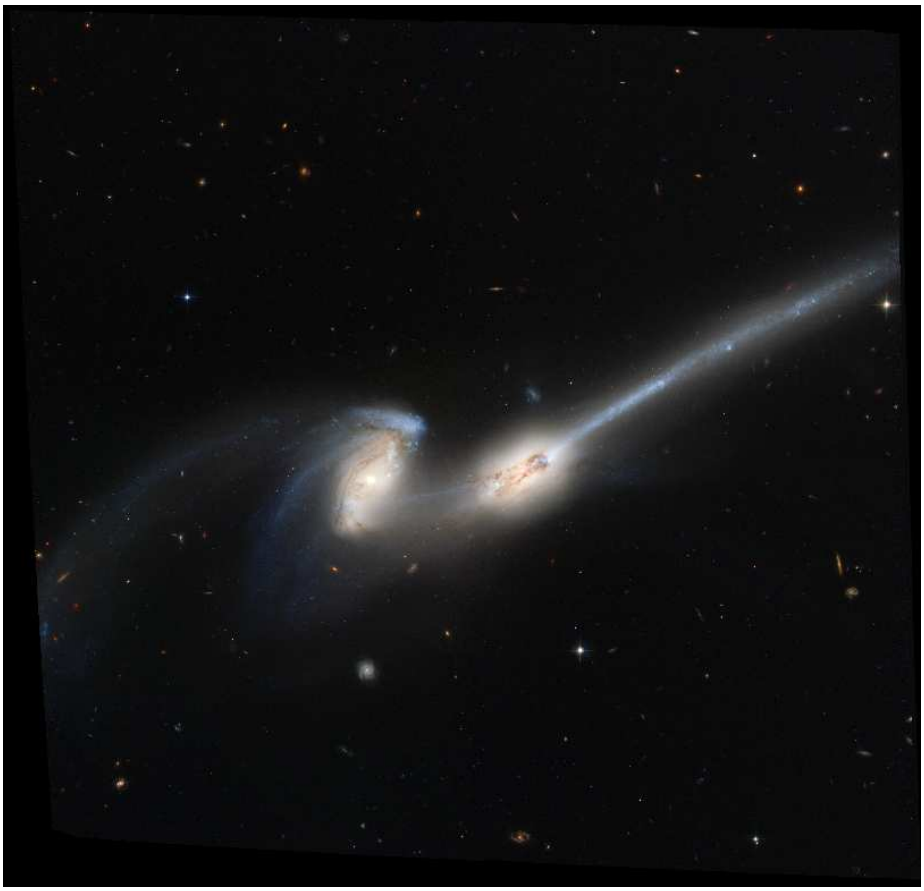

Figuur 1 – Twee botsende sterrenstelsels die de naam "de muizen" hebben gekregen. Tijdens de botsing zijn de sterrenstelsels zelf vervormd en zijn er lange staarten van sterren en gas uitgetrokken. Tijdens de botsing vind zeer sterke stervorming plaats. Deze sterrenstelsels zullen over de komende milljard jaar langzaam om elkaar heen draaien, weer botsen en uiteindelijk samensmelten om een groter sterrenstelsel te vormen (Foto genomen met de Advanced Camera for Surveys aan boord van de Hubble Space Telescope; credit: ACS Science & Engineering Team/HST/NASA).

Introductie

In het Heelal kunnen we buiten ons eigen sterrenstelsel, de Melkweg, veel andere sterrenstelsels waarnemen. Sommigen hiervan zijn vergelijkbaar in vorm en structuur met onze eigen Melkweg, terwijl andere sterrenstelsels een heel andere verschijning hebben. In eerste instantie zag men deze sterrenstelsels als geïsoleerde eilandjes in het Heelal. Tegenwoordig weten we echter dat sterrenstelsels zijn geworden tot wat ze zijn door interacties met andere sterrenstelsels. Rondom de Melkweg nemen we tientallen kleinere satelliet-stelsels waar, die ingevangen zijn door de Melkweg en onder invloed van diens zwaartekracht vervormd en langzaam uit elkaar getrokken worden. Sterrenstelsels als deze satelliet-stelsels zijn meer dan 100 maal kleiner dan de Melkweg en worden dwergsterrenstelsels genoemd. Daarnaast zijn er om ons heen duidelijke voorbeelden te vinden van sterrenstelsels die in verschillende stadia van een daadwerkelijke botsing en samensmelting zijn. Een voorbeeld van botsende sterrenstelsels is te zien in Fig. 1.

In de huidige standaard kosmologie zouden zulke botsingen voor sterrenstelsels in alle massaschalen voor moeten komen. Dit Proefschrift beschrijft onderzoek naar botsingen tussen dwergsterrenstelsels en hun eigen satelliet-stelsels, en de effecten hiervan. Onderzoek naar dit soort episodes in de evolutie van dwergsterrenstelsels kan ons veel leren over de vorming en evolutie van sterrenstelsels in het algemeen en dwergsterrenstelsels in het bijzonder. Bovendien kunnen de resultaten van het onderzoek licht werpen op de eigenschappen van een van de mysterieuze bouwstenen van het Heelal, de "donkere materie".

Om het onderzoek beschreven in dit Proefschrift in context te plaatsen, gaan we eerst de vorming van structuur in het Heelal en de vorming en evolutie van sterrenstelsels nader bekijken. Verschillen in de vormingsgeschiedenis van sterrenstelsels heeft geleid tot een variëteit aan verschillende soorten sterrenstelsels die door astronomen worden geclassificeerd. Deze classificaties worden behandeld in Sectie 5.5. Omdat dit Proefschrift botsingen tussen sterrenstelsels behandelt, beschrijven we mogelijke effecten van botsingen tussen sterrenstelsels in Sectie 5.5. Sectie 5.5 beschrijft vervolgens hoe astrofisici de evolutie van sterrenstelsels modelleren met behulp van computersimulaties om hier meer over te leren. Hiermee kunnen tot slot de resultaten van dit Proefschrift zoals beschreven in Sectie 5.5 in context geplaatst worden.

De vorming van structuur in het Heelal

In de sterrenkunde is op dit moment een kosmologie genaamd Λ Cold Dark Matter (ΛCDM) de standaard. Hierbij domineert "donkere energie" (de Λ) de energiedichtheid van het Heelal met $\sim 69\%$, en neemt de donkere materie vervolgens $\sim 26\%$ voor zijn rekening. Wetenschappers denken dat

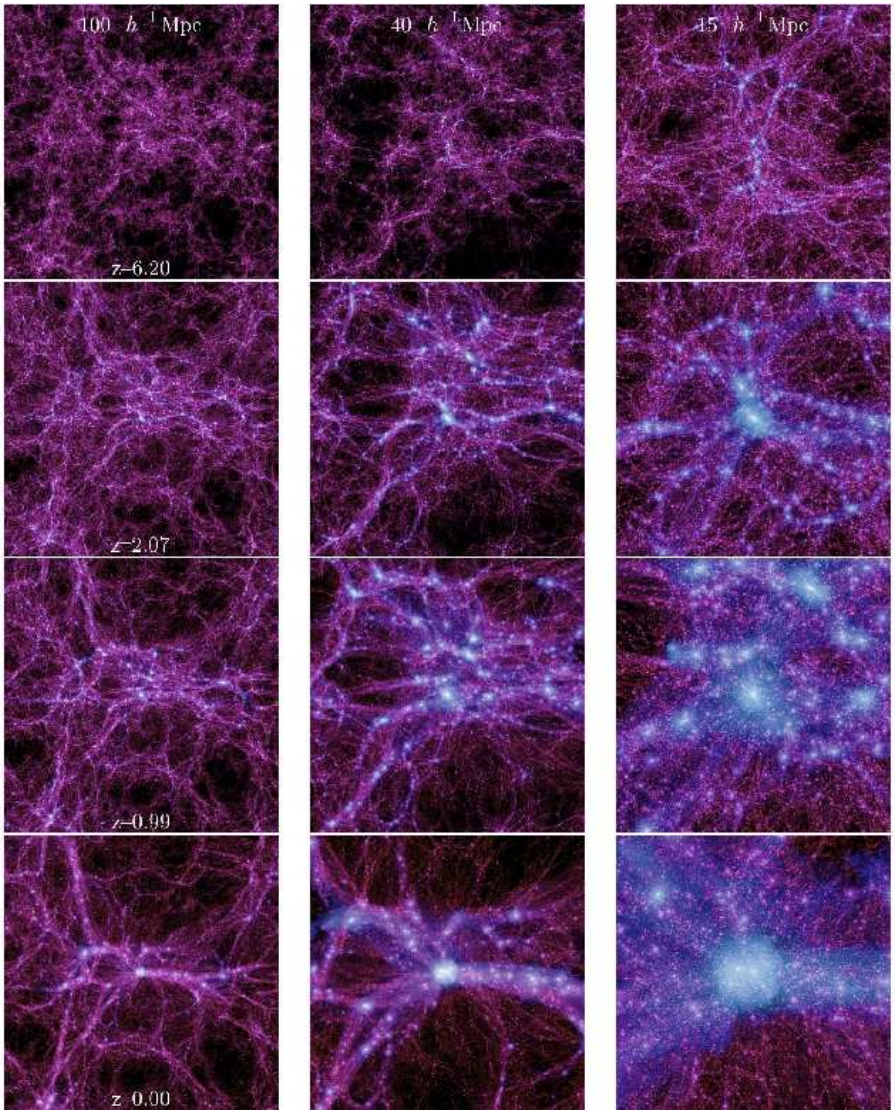

Figuur 2 – De evolutie over tijd van de structuur in een simulatie van een heelal dat uitsluitend uit donkere materie bestaat. Het figuur laat de structuur op 3 verschillende ruimtelijk schalen zien: het volledige gesimuleerde volume (100 Mpc/h), en twee verder ingezoomde regio's. Het centrale object is de zwaarste donkere materie halo in deze specifieke simulatie (de Millennium-II simulatie) en heeft in de tegenwoordige tijd ($z = 0$) een totale massa van ongeveer 800 maal de totale massa van de donkere materie halo van de Melkweg. De tijd wordt weergegeven door de grootte van het uitdijende Heelal in vergelijking tot de huidige grootte: van boven naar beneden is de grootte van het Heelal: $1/7$ ($z = 6$), $1/3$ ($z = 2$), $1/2$ ($z = 1$), en gelijk ($z = 0$) aan de huidige grootte van het Heelal. Figuur uit Boylan-Kolchin et al. (2009).

dit een elementair deeltje is dat zeer zwak interacteert met andere deeltjes en zichzelf. Er wordt op het moment naarstig gezocht naar direct bewijs van donkere materie en naar de eigenschappen ervan, zowel door astrofysici als door experimenteel natuurkundigen. Onderzoekers hopen dit mysterie in het komende decennium te kunnen opgehelderen. De laatste $\sim 5\%$ van de energiedichtheid in het Heelal is in de vorm van baryonen, de enige materie die we in principe kunnen waarnemen met het licht/elektromagnetisch spectrum. Van de aanwezige baryonen in het Heelal hebben we echter tot nu toe maar een kleine fractie direct waargenomen.

De structuur van materie in het Heelal is waarschijnlijk gevormd op een hiërarchische manier. Het vroege Heelal had een zeer hoge temperatuur en dichtheid, maar bevatte kleine regio's met een net hogere dichtheid dan hun omgeving. Deze minimale verschillen kunnen we terugvinden als temperatuurverschillen van ongeveer 1/100000 van de gemiddelde temperatuur in de Kosmische Microgolf Achtergrondstraling, een reliek van het vroege Heelal op basis van de temperatuur van straling met een golflengte van micrometers. De gebiedjes met een net hogere dichtheid zijn gegroeid door materiaal uit hun omgeving aan te trekken. Wanneer deze gebiedjes genoeg massa hadden om de algemene uitdijing van het Heelal tegen te gaan, zijn ze ineengestort om zelfstandige structuren te vormen, de zogenaamde donkere materie halo's. Hoewel onze moderne kosmologie aanneemt dat het Heelal op extreem grote schaal uniform en isotroop is (het "kosmologische principe" genaamd), laten de structuur van het kosmische web en van de afzonderlijke clusters en groepen van halo's zien dat op kleinere schaal de distributie van materie in het Heelal zeer complex is. Een voorbeeld hiervan is te zien in Fig. 2.

Sterrenstelsels in het Heelal

Sterrenstelsels vormen en zijn ingebed in de bovengenoemde donkere materie halo's. Tijdens dit vormingsproces, in het vroege Heelal, nog waar te nemen op extreem grote afstand van ons, zijn sterrenstelsels erg onregelmatig. Daarentegen kunnen in onze directe omgeving structureel verschillende vormen sterrenstelsels onderscheiden worden. Net als in de andere natuurwetenschappen proberen onderzoekers in de sterrenkunde vaak door waargenomen objecten te classificeren een beter begrip te krijgen van de onderliggende vormings- en evolutieprocessen. De meest bekende classificatiemethode voor sterrenstelsels is voor het eerst voorgesteld door Hubble in 1936 (de Hubble stemvork) en meer gedetailleerd beschreven door Sandage in 1961. Deze classificatie onderscheidt twee algemene klassen: de elliptische sterrenstelsels en de spiraalsterrenstelsels. Sterrenstelsels die niet binnen een van deze twee gedefinieerde klassen vallen, worden ingedeeld bij een afgescheiden, derde

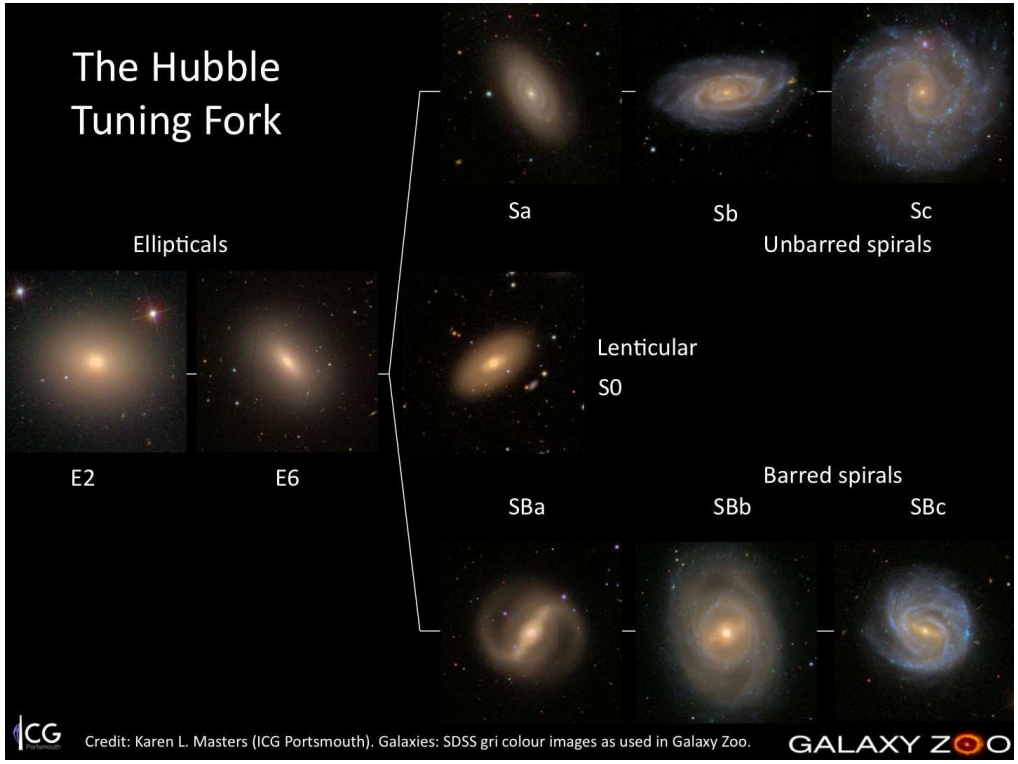

Figuur 3 – De classificatie van sterrenstelsels in elliptische stelsels (links, met verschillende graad van ellipticiteit), spiraalstelsels (rechts, met verschillende graad van dominantie van de spiraalstructuur en de centrale verdikking, en met of zonder balkstructuur) volgens de Hubble stemvork. Sterrenstelsels die niet in de deze groepen vallen worden onregelmatig genoemd. Credit: Karen Masters met afbeeldingen van het Galaxy Zoo project van waarnemingen van de Sloan Digital Sky Survey.

groep van "onregelmatige sterrenstelsels". Een voorbeeld van de classificatie van Hubble is te zien in Fig. 3.

Onze Melkweg zelf is een spiraalsterrenstelsel. De spiraalsterrenstelsels zijn de klasse aan de rechterkant van de Hubble stemvork in Fig. 3, en onderverdeeld in spiraalsterrenstelsels met en zonder dominante centrale balkstructuur (rechtsboven en -onder in Fig. 3). Deze sterrenstelsels zijn het meest voorkomend in de populatie sterrenstelsels van gemiddelde massa. Hun schijven van sterren en gas met grotere of kleinere spiraalstructuur is zeer opvallend, maar ze kunnen ook andere componenten hebben met variërende prominentie, zoals centrale bolvormige verdikkingen (bulges genoemd) en centrale balkstructuren. De schijf van gas kan gelijk aan of een paar maal groter dan de schijf van sterren zijn.

Elliptische sterrenstelsels (de klasse aan de linkerkant van de Hubble stemvork in Fig. 3) hebben, zoals de naam suggereert, een elliptische vorm. Ze hebben meestal veel minder gas dan spiraalsterrenstelsels. Onder de sterrenstelsels die vergelijkbare massa hebben als de Melkweg bestaat maar een kleine fractie uit elliptische sterrenstelsels. Onder grotere massa sterrenstelsels vormen elliptische sterrenstelsels een steeds grotere fractie van de populatie. In een cluster van sterrenstelsels zijn de meer centrale sterrenstelsels bijna altijd elliptische sterrenstelsels.

In zowel spiraalsterrenstelsels als elliptische sterrenstelsels kunnen substructuren of kleine onregelmatigeheden in de vorm en structuur voorkomen. Deze kunneen interne of externe oorzaak hebben. In de context van dit Proefschrift zijn we vooral geinteresseerd in externe oorzaken van onregelmatigeheden in sterrenstelsels, en dan met name externe oorzaken in de vorm van interacties met andere stelsels.

Dwergsterrenstelsels

Kijken we naar lagere massa sterrenstelsels dan komen we in het regime van de dwergsterrenstelsels. Er is geen eenduidige scheidslijn tussen dwergsterrenstelsels en grotere sterrenstelsels. Veel definities zijn gebaseerd op de geobserveerde helderheid en grootte van stelsels. Er wordt een grote variëteit aan soorten dwergsterrenstelsels onderscheiden waarvan de verschillende soorten vaak een historisch observationele oorsprong hebben. Zo kennen we: de sferoïdale dwergsterrenstelsels (dwarf spheroidals; dSph), de elliptische dwergsterrenstelsels (dwarf ellipticals; dEll), de onregelmatige dwergsterrenstelsels (dwarfs irregulars; dIrr), de ultra-zwakke dwergsterrenstelsels (ultra-faint dwarfs; UFDs), de blauwe, compacte dwergsterrenstelsels (blue compact dwarfs; BCDs), de extreem metaal-arme sterrenstelsels (extremely metal-poor galaxies; XMP), sterrenstelsels met gebieden met veel geïoniseerd waterstofgas (HII) door een grote dichtheid aan jonge sterren (HII-sterrenstelsels), en ultra-compacte dwergsterrenstelsels (ultra-compact dwarfs; UFDs).

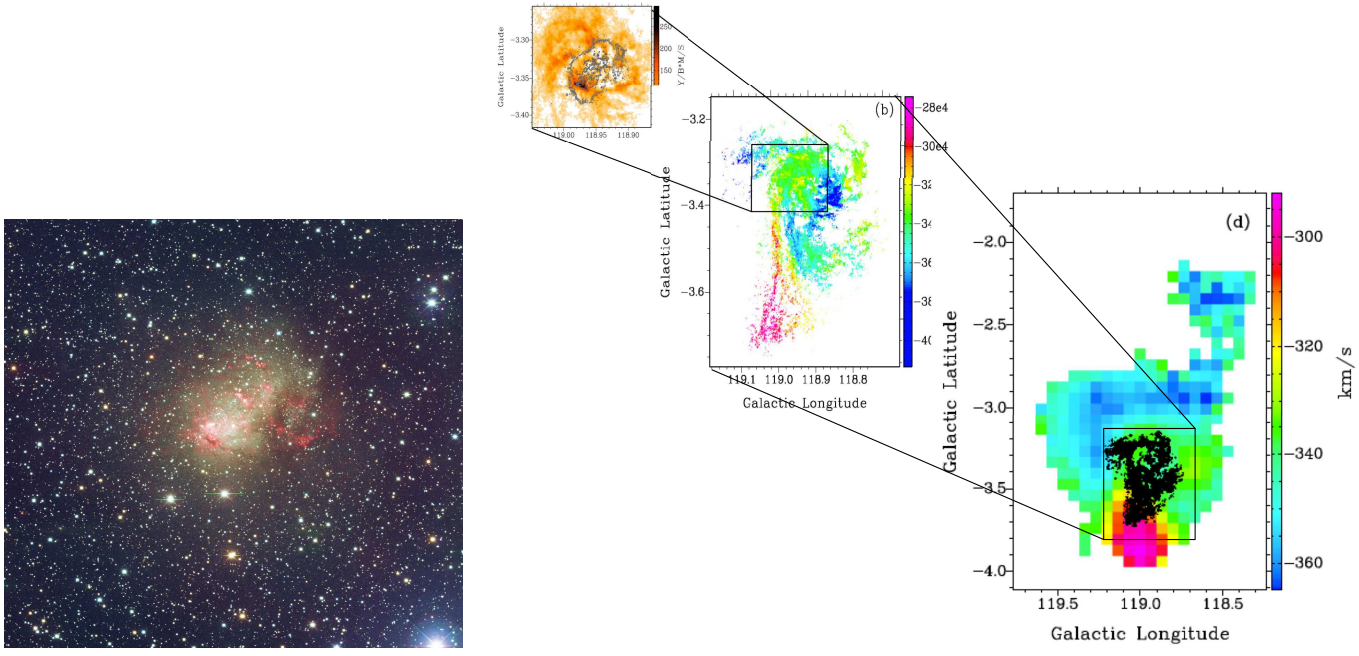

Figuur 4 – De onregelmatige structuur in gas en sterren van het dwergsterrenstelsel IC10. Uiterst links de ster-component door the Lowell Observatory Local Group Survey (zie Massey et al. 2007), en aan de rechterkant de optisch waarnemingen van de ster-component als indicatie (in het grijs in de figuur tweede van links) bovenop waarnemingen van het neutrale waterstofgas (HI). Het neutrale waterstofgas is waargenomen met twee verschillende resoluties. Bij hogere resolutie kan alleen de verdeling van het gas met hogere dichtheid waargenomen worden, maar wel tot in een zeker detail (middelste twee figuren). Bij lagere resolutie kan de verdeling van het gas tot lagere dichtheden geobserveerd worden, maar is de waargenomen structuur niet zo gedetailleerd (uiterst rechts, met de vorm van de hogere dichtheid waterstof van de figuur tweede van rechts er bovenop in zwart). In de twee meest rechtse figuren geven de kleurschalen de snelheden van het gas weer. De waarnemingen zijn gedaan met de Very Large Array (links en in het midden) en de Greenbank Telescope (rechts) (Figuur uit Ashley et al. (2014)).

Dicht bij grotere sterrenstelsels en in clusters zijn veelal de gas-loze sferoïdale, elliptische en ultra-zwakke dwergsterrenstelsels te vinden. Hierbuiten komen vooral de gas-rijke en onregelmatige overige soorten dwergstelsels veel voor. Over het algemeen zijn dwergsterrenstelsels veel onregelmatiger dan grotere sterrenstelsels. Daarnaast zien we de lagere mass schijfstelsels vaak dikker zijn dan Melkweg-achtige schijfstelsels. Dit is terug te vinden in de kinematische eigenschappen, waarbij sprake is van rotatiesnelheden voor sterren, die niet, of niet veel, groter zijn dan hun ongeordende of willekeurige snelheden.

Dwergsterrenstelsels worden, als kleine sterrenstelsels, sneller beïnvloed door interne en externe processen. Echter, omdat vele processen vergelijkbare resultaten kunnen geven, is het ook lastiger om te identificeren welk proces er precies verantwoordelijk is voor de waargenomen eigenschappen. Een voorbeeld van een verstoord dwergsterrenstelsel is te zien in Fig. 4. Dit dwergsterrenstelsel, IC10 genaamd, is zeer onregelmatig in de structuur en kinematica, zowel wat betreft de sterren als het gas. In dit geval is de oorzaak van de verstoring waarschijnlijk extern. Wat de exacte oorsprong van de externe oorzaak is, is echter erg lastig vast te stellen.

Het onderzoek naar de evolutie van dwergsterrenstelsels kent nog veel open vragen. Binnen het kader van een ΛCDM kosmologie is de structuur van de donkere materie halo's nagenoeg volledig schaal-vrij: de structuur van de halo van de Melkweg en de structuur van de halo van een dwergsterrenstelsel zijn bijna hetzelfde. Voor dwergsterrenstelsels zijn er zeer veel effecten die de stervormingsprocessen in die halo's kunnen beïnvloeden. Externe effecten zijn de kosmische achtergrondstraling in het vroege Heelal, de invloed van een nabij groter sterrenstelsel, of interacties met andere kleine sterrenstelsels of intergalactische gaswolken. Interne processen zijn onder andere effecten van het stervormingsproces op het omringende gas en onstabiliteiten in de ster- of gas-schijf. Daarnaast zien we in verschillende typen dwergsterrenstelsels overlappende maar ook afwijkende eigenschappen. Dit werpt de vraag op wat hun karakteristieke vormingsgeschiedenis is. Bovendien lijken nieuwe waarnemingen te laten zien dat ons beeld van dwergsterrenstelsels nog verre van compleet is. Er blijken typen dwergsterrenstelsels te bestaan, die zo lastig te detecteren zijn dat we ze nu alleen kunnen vinden door naar hun specifieke signatuur op zoek te gaan. Het is waarschijnlijk dat er soorten dwergsterrenstelsels zijn die op dit moment nog buiten onze waarnemingsmogelijkheden liggen.

Een belangrijke vraag in de sterrenkunde is hoe klein een sterrenstelsel kan zijn. Is er een minimale massa voor een sterrenstelsels? Zijn er donkere materie halo's zonder sterren? Deze twee vragen zijn eigenlijk hetzelfde: we gaan er van uit dat elk zelfstandig sterrenstelsel zich in een donkere materie halo bevindt, maar het omgekeerde hoeft niet waar te zijn. Dit is erg relevant met het oog op het vergelijken van modellen met donkere materie met waarnemingen van sterrenstelsels. Om een voorbeeld hiervan te geven: de

modellen voorspellen een zeer groot aantal kleine halo's in de omgeving van de Melkweg maar we zien maar enkele tientallen dwergsterrenstelsels in dat gebied. Een mogelijke en populaire oplossing voor deze tegenstrijdigheid is dat kleinere donkere materie halo's door toedoen van een aantal verschillende processen (bijna) geen sterren hebben kunnen vormen en daarom niet of nauwelijks zichtbaar zijn voor ons. Deze sterrenstelsels worden "ster-loze" of "donkere" sterrenstelsels genoemd. In het onderzoek gepresenteerd in dit Proefschrift gaan we uit van de voorspelling dat donkere stelsels bestaan, en identificeren we de gevolgen van die voorspelling op dwergsterrenstelsels.

Botsende sterrenstelsels

Zoals eerder vermeld, denken we dat botsingen en samensmeltingen, of mergers, van sterrenstelsels een belangrijke rol speelt in de vorming en evolutie van sterrenstelsels. Hoewel er al langer ideeën zijn over botsingen tussen sterrenstelsels, het belang ervan in de evolutie van sterrenstelsels en de effecten ervan op het voorkomen en de structuur van sterrenstelsels, is dit proces pas meer structureel onderzocht in de laatste decennia van de vorige eeuw. Pas rond die tijd werd het mogelijk om sterrenstelsels en botsende sterrenstelsels te simuleren met computermodellen. Een bijzondere uitzondering hierop is het werk van Holmberg uit 1941, waarin hij een botsing tussen twee spiraalsterrenstelsels modelleerde met behulp van 37 gloeilampen per sterrenstelsel die hij handmatig verplaatste.

Botsingen en daaropvolgende samensmeltingen van sterrenstelsels kunnen grote en permanente gevolgen hebben voor de massa, vorm, structuur, kinematica en stervormingsgeschiedenis het uiteindelijke stelsel. Veel voorkomende effecten zijn onregelmatigeheden of veranderingen in de ster- en gasverdeling (bijvoorbeeld lange armen of staarten zoals in Fig. 1), een (sterke) verdikking van een ster-schijf in een spiraalstelsel en een tijdelijke (extreem) sterkere mate van stervorming. En groot deel van het gas van de botsende stelsels wordt naar het nieuwe gemeenschappelijke centrum gedreven waar het in zeer rap tempo nieuwe sterren vormt. Een botsing van twee ongeveer even grote spiraalsterrenstelsels kan resulteren in een groot elliptisch sterrenstelsel. Als echter een deel van het gas dat aanwezig was in de botsende stelsels niet direct in het centrum sterren vormt, is het ook mogelijk dat er een nieuwe dunne gas-schijf ontstaat, die weer het leven schenkt aan een nieuwe jonge ster-schijf. De grote diversiteit aan eigenschappen van de oorspronkelijke twee sterrenstelsels en de parameters van de botsing, zorgen voor een verscheidenheid aan mogelijke uitkomsten.

Voor interacties tussen twee sterrenstelsels met verschillende massa, minor mergers (in tegenstelling tot botsingen tussen twee stelsels van ongeveer dezelfde massa: major mergers), is er vooral onderzoek gedaan naar interacties van stelsels met een massa vergelijkbaar met de Melkweg met een satelliet-

stelsel. Deze zogenaamde minor mergers veroorzaken voor een Melkweg-grootte stelsel vooral kleine onregelmatigheden of substructuren bovenop de schijfstructuur van het spiraalsterrenstelsel. Omdat de effecten van minor mergers over het algemeen kleiner zijn, zijn ze lastiger te detecteren op basis van gegevens van waarnemingen.

Het modelleren van sterrenstelsels

De vorming en evolutie van de structuur in het Heelal, het kosmische web, en de halo's en sterrenstelsels is te modelleren met behulp van grote computersimulaties. Voor simulaties die uitsluitend de structuurvorming in de donkere materie volgen, hoeft alleen de zwaartekracht berekend te worden. Dit betekent dat zeer grote en gedetailleerde simulaties gedaan worden om de grote schaal structuur en de eigenschappen van donkere materie halo's te beschrijven.

Het modelleren van sterrenstelsels is echter een stuk gecompliceerder. Processen die verband houden met gasfysica, stervorming, sterevolutie en supernova's, zwarte gaten en actieve galactische kernen, en hoog-energetische astrofysica moeten idealiter allemaal meegenomen worden. Echter, de meeste van deze processen worden nog niet tot in detail goed begrepen, laat staan dat ze tot in detail goed te modelleren zijn. Daarom worden er vaak empirische of theoretische relaties gebruikt om de fysische processen onder een bepaalde resolutie, of schaal, te beschrijven.

Voor het modelleren van sterrenstelsels zijn er verschillende simulatiemethoden. Bij één wordt de dynamica van donkere materie, gas en sterren expliciet gevolgd tot een bepaalde resolutie. Een voorbeeld van de vorming van een grote donkere materie halo in de context van het kosmische web met deze methode is te zien in Fig. 2. Deze hydrodynamische modelleertechniek wordt gebruikt in Hoofdstuk 2 en Hoofdstuk 3 van dit Proefschrift. Een andere optie is om de informatie over donkere materie halos van grote N-body simulaties te gebruiken en te berekenen wat voor soort sterrenstelsels daarin zouden behoren te zitten. De evolutie van sterrenstelsels wordt in dat geval uitsluitend beschreven door series van empirisch of fysisch beargumenteerde relaties en formules. Deze sterrenstelsels hebben daardoor geen ruimtelijke informatie voor de posities van gas en sterren, alleen de totale massa aan gas en sterren. Een simulatie volgens deze methode wordt in Hoofdstuk 5 gebruikt. Daarmee wordt onder andere berekend wat voor sterrenstelsels de halo's van Fig. 2 bevatten.

Met behulp van deze modelleertechnieken kan de evolutie van sterrenstelsels in verschillende context tot in groot detail onderzocht worden, zowel in een kosmologische context, vanaf de vorming van de eerste sterren tot nu, als in geïsoleerde situaties waar de effecten van variaties in begincondities op het eindresultaat onderzocht kan worden.

Dit Proefschrift

Dit Proefschrift presenteert onderzoek naar de effecten van invallende satelliet-stelsels op dwergsterrenstelsels. Aangezien de satelliet-stelsels nog kleiner zijn dan de dwergsterrenstelsels zelf is er een grote kans dat het ster-loze of donkere sterrenstelsels zijn. De gravitationele effecten van de merger zullen echter nog steeds aanwezig zijn. Bovendien hebben dwergsterrenstelsels een kleinere massa aan baryonische materie (sterren en gas) in verhouding tot hun massa aan donkere materie in vergelijking met grotere sterrenstelsels. Daarom kan een merger voor een dwergsterrenstelsel een veel groter effect hebben dan voor een Melkweg-achtig sterrenstelsel. In een botsing van een dwergsterrenstelsel en diens donkere satelliet-stelsel zullen de gravitationele effecten van de botsing erg groot kunnen zijn terwijl er maar één sterrenstelsel direct waargenomen kan worden.

Hoofdstuk 2 beschrijft simulaties van botsingen tussen dwergsterrenstelsels met verschillende massa's aan ster-schijven en hun donkere satelliet-stelsels. Hier laten we zien dat de kleinere massa aan sterren en gas in dwergsterrenstelsels leidt tot meer extreme effecten naar aanleiding van de botsing, die in alle gevallen sterke vervorming veroorzaakt. De gesimuleerde botsing is een minor merger, waar de massa van het satelliet-stelsel 5 maal zo klein is als de totale massa (inclusief halo) van het dwergsterrenstelsel. Desalniettemin kan de botsing de vorm, structuur en kinematica van de ster-schijf van het dwergsterrenstelsels totaal veranderen. Het resulterende sterrenstelsels kan zelfs een meer sferoïdale vorm hebben dan schijfvormig. Dit laat zien dat interacties zoals beschreven in dit Proefschrift nieuwe vormingsmechanismen kunnen zijn voor sferoïdale dwergsterrenstelsels.

In Hoofdstuk 3 breiden we deze simulaties uit door het toevoegen van gas aan het dwergsterrenstelsel. Hier laten we zien dat een minor merger voor een dwergsterrenstelsel met een donker sterrenstelsel kan leiden tot een zeer sterke toename in de mate van stervorming, zowel in korte scherpe pieken van stervormingsactiviteit als in een langdurige toename. Daarnaast is, als gevolg van de botsing, ook in de gasverdeling sterke vervorming te zien. Bovendien worden de effecten op de ster-schijf niet verminderd door de aanwezigheid van gas, zoals wordt gevonden in simulaties van Melkweg-achtige sterrenstelsels. We karakteriseren en beschrijven de invloed van variaties in beginwaarden van verschillende eigenschappen van het dwergsterrenstelsel, het donkere sterrenstelsel en de botsing zelf, op de effecten tijdens en na de botsing. We vergelijken een aantal globale eigenschappen van onze model-sterrenstelsels met waargenomen dwergsterrenstelsels en zien een goede overeenkomst.

Om uiteindelijk de voorspellingen van de hierboven beschreven simulaties te testen aan waarnemingen proberen we in Hoofdstuk 4 op een kwantitatieve manier de observationele eigenschappen van de gesimuleerde botsende

dwergsterrenstelsels te beschrijven. Hiervoor hebben we methoden gebruikt die zijn toegepast op een grote verscheidenheid aan waargenomen sterrenstelsels. Deze methoden kwantificeren indicatoren van de vorm en kinematica van waargenomen stelsels, bijvoorbeeld de asymmetrie en de concentratie van de lichtverdeling. We laten hier zien dat de dwergsterrenstelsels door botsingen een grote verscheidenheid aan waarden kunnen bereiken. We meten de waarden van alle indicatoren op vaste tijdstippen in alle simulaties. Afhankelijk van het moment en de sterkte van de botsing kunnen de waarden van de indicatoren dus erg verschillen. Uit het onderzoek blijkt echter dat dwergsterrenstelsels die geen botsing ervaren bijna altijd specifieke waarden voor de meeste indicatoren hebben. Een combinatie van deze indicatoren kunnen dus gebruikt worden om uit waarnemingen dwergsterrenstelsels te zoeken die in een botsing met een donker satelliet-stelsel zijn.

Een belangrijke vraag in deze context is hoe vaak botsingen tussen dwergsterrenstelsels en donkere sterrenstelsels te verwachten zijn. In Hoofdstuk 5 combineren we een kosmologische simulatie met uitsluitend donkere materie, met een model van de vorming en evolutie van sterrenstelsels op basis van de gegevens van de donkere materie halo's. We gebruiken dit model om in de vormingsgeschiedenis van een groot aantal dwergsterrenstelsels botsingen met hun donkere satelliet-stelsels te traceren en te bestuderen. Uit dit onderzoek blijkt dat ongeveer 10% van de dwergsterrenstelsels een merger zoals bestudeerd in dit Proefschrift heeft beleefd sinds het Heelal $2/3$ van zijn huidige grootte had (iets meer dan 4 miljard geleden).

Alles bij elkaar laat dit Proefschrift zien dat botsingen tussen dwergsterrenstelsels en donkere sterrenstelsels grote effecten kunnen hebben. Vanuit een statistisch oogpunt zijn zulke interacties niet verwaarloosbaar in de vormingsgeschiedenis van de populatie van dwergsterrenstelsels. Botsingen van dwergsterrenstelsels met donkere satelliet-stelsels kunnen een belangrijke rol spelen in de vorming van sterk stervormende dwergstelsels of sferoïdale stelsels, en in de totale variëteit aan dwergsterrenstelsels die we om ons heen zien. Bovendien kunnen deze bevindingen gebruikt worden om indicaties van ster-loze of donkere sterrenstelsels te vinden door de effecten van hun botsingen met dwergsterrenstelsels. Daarmee levert dit Proefschrift tevens een nieuwe en oorspronkelijke bijdrage aan de zoektocht naar de eigenschappen van donkere materie.

Acknowledgements

This Thesis is the culmination of some wonderful years. A large number of people have contributed to the great times and the fun I have had during those years. Also, I love to learn, and during the last years I have learned many interesting things, astronomy-related and otherwise. I hope to continue both in the coming years, but first I would like to thank everyone who made the fun and the learning possible.

Amina, I think you are a wonderful supervisor, and I feel privileged to have been your student. Under your guidance I have learned to do good research, for example by using my curiosity to understand the details of the project but not to get lost in this. I loved the way my projects gradually developed out of earlier results and discussions. Thank you very much for your trust and confidence in me. I am also very grateful for your support and personal interest, especially during more challenging times. I have very much enjoyed being part of your research group. Your encouragement to discuss our own and others' work, from the tiniest detail to the broader context and new ideas, is wonderful and a great way to learn and do science. And of course thank you for encouraging and initiating many great dinners and cocktail evenings with the group.

Laura, my unofficial co-promotor, thank you for your wonderful enthusiasm, ideas, questions, and support. Talking and discussing with you always makes me happy, and provides a boost for my motivation with a ton of new ideas. I had a wonderful time visiting you in Boston, science-wise and otherwise! I hope we can work together on many more projects in the future.

I also would like to thank Claudio Dalla Vecchia and Joop Schaye for allowing me to use the OWLS version of Gadget, and Claudio for his guidance

in setting up and analyzing the first test simulations during a visit to MPE, and for helping out with any questions I had. Else, thank you for letting me use your version of the semi-analytic code and helping me out with setting up the SAM in combination with the Millennium-II files. Carlos Vera-Ciro and Maarten Breddels have helped me with lots of smaller and larger computation and visualization questions, for which I am very grateful.

I am also very grateful to my reading committee. Eline, Joop, and Julio, thank you for taking the time to read my Thesis, and thank you for your comments. I am very honored that you are all planning to attend my defense, and I look forward to some interesting discussions.

The Kapteyn Institute is a great study and work environment and I have very much enjoyed my time there. Many people at the institute contribute to the very open and positive atmosphere. I have had great discussions with almost everyone about a huge variety of subjects, and I would like to thank everyone for the great time I had at Kapteyn.

I would like to thank Amina's group: Laura, Facundo, Else, Yang-Shyang, Carlos, Maarten, Teresa, Giacomo, Hans, Kyle, Robyn, Hao, Shoko, Jovan, Jorrit, Manolis, Davide, Helmer, Lorenzo, Pim, Martín, Yamila, Steven, Johanna, and Casper for many great discussions, meetings, and parties. A special thanks also goes to the Galactic Dynamics (or bible) study group (part of Amina's group), and the Kapteyn Bayesians study group for many interesting sessions and shared thoughts about both subjects.

Many thanks to the people who provide the basis on which the Kapteyn Institute is build, Wim, Martin, Eite, Valentin, Maarten, Hennie, Jackie, Gineke, Christa, Martine, and Lucia, for all their help, patience, cheerfulness, and interest.

Thomas, Esra, Sofia, Asa, Anaïs, Zheng, and Tuba, it was very good to share an office with you, thank you for all the nice talks but also for the good work climate. Leon, even though you were my officemate before the PhD, you also belong in this group, thank you.

I would furthermore especially like to thank Hans, Eva, Leon, Shoko, Giacomo and Ewa, Stephan, Gergö and Anke, Patrick, Jouke, Ellen, Scott, Robyn, Beth, Maarten, Jovan, Manolis, Teresa, Sofia and Thomas, Yunhee, and Asa for all the friendship, asked or unasked advice, and the great shared moments involving coffee times, lunches, dinners, music, sports, or just a good talk.

Ook veel vrienden van buiten de sterrenkunde hebben bijgedragen tot veel steun en plezier in de afgelopen jaren: Veera, Olger en Laura, Cees, Quirine en Benno, Ellen, Lieke en Marcel, en Nienke en Tom, heel erg bedankt voor jullie vriendschap en alle fijne activiteiten en momenten.

Als laatste wil ik graag mijn familie bedanken, voor alle interesse, steun, plezier, en liefde. Jaap, Annet, Else, Jasper, Joost, Corien, Paul, Trees, Susan, Iris, Bas, en Jan Willem, dank jullie wel. Else en Jasper, jullie zijn niet voor

niets mijn paranimfen, ik ben heel blij jullie als broer en als zus (en collega) te hebben. Jaap en Annet, dank jullie wel voor jullie onvoorwaardelijke liefde en steun, maar ook uitdaging. Het is geweldig te voelen dat jullie trots op ons zijn, en ik ben trots op jullie.

Liefste Roel, dank je wel voor onze geweldige tijd in Groningen samen en ik kijk uit naar een supermooie tijd samen in New York en waar we verder nog terecht komen. Samen met jou is alles is mooier.

Thank you all!
Tjitske